DISS. ETH NO. 22847

DYNAMIC SIGNAL PROCESSING IN GENE REGULATION

A thesis submitted to attain the degree of

DOCTOR OF SCIENCES of ETH ZURICH

(Dr. sc. ETH Zurich)

presented by

RYAN KELLOGG

M.S. Biomedical Engineering, Carnegie Mellon University

born on 17.09.1984

citizen of

United States

accepted on the recommendation of

Prof. Dr. Savas Tay

Prof. Dr. Kobi Benenson

Prof. Dr. Renato Paro

Prof. Dr. Timm Schroeder

2015

TABLE OF CONTENTS

ZUSAMMENFASSUNG

Zellen sind multiplen Umweltsignalen ausgesetzt, welche sich zeitlich oft ändern und nur von wenigen Kernsignalnetzwerken detektiert werden, die diese Umweltsignale in eine spezifische Genexpressionsantwort transformieren. NF-kappaB ist ein Genkontrollnetzwerk, welches in der Koordination von Prozessen wie zellulärem Stress und Entzündungen involviert ist. Das Signalnetzwerk hat zwei wichtige dynamische Eigenschaften: 1) digitale Aktivierung, was bedeutet, dass der Signalprozess homogen abläuft, wenn das Eingangssignal einen Schwellenwert überschreitet. Wird dieser Grenzwert nicht erreicht, findet kein Signalfluss statt. 2) Eine verzögerte negative Rückkopplung führt zu einer oszillierenden NF-kappaB Lokalisierung im Zellkern. Diese Dissertation untersucht die Rolle dieser zwei dynamischen Eigenschaften des NF-kappaB Netzwerkes in biologischen Prozessen.

Das erste Ziel dieser Arbeit war die Entwicklung und Implementierung eines mikrofluidischen Arbeitsprozesses, welcher das Messen und Analysieren von dynamischen Einzelzellexperiment mit hohem Durchsatz routinemässig ermöglicht. Dies war notwendig, da Durchsatz, Präzision und die Möglichkeit die zelluläre Mikroumwelt während der Datenakquisition mittels Videomikroskopie zu manipulieren, für aktuelle Methoden limitiert sind. Unser mikrofluidischer Ansatz erlaubt es uns eine Sukzession von Arbeitsschritten zu kombinieren. Wir können ein videomikroskopisches Experiment mit dynamischen Eingangssignalen und Genexpressionsmessungen verbinden und diese routinemässig analysieren.

Als zweites haben wir die Funktion der digitalen NF-kappaB Aktivierung untersucht. Abhängig von ihrer räumlichen und biologischen Umgebung sind Zellen Stimuli von unterschiedlicher Stärke und Dauer ausgesetzt. Zellen in der Nähe einer Infektionsstelle sind zum Beispiel kurzen Entzündungssignalen hoher Intensität ausgesetzt, während weiterentfernte Zellen ein langes aber schwaches Signal empfangen. Durch eine Kombination von experimentellen und rechengestützten Ansätzen haben wir entdeckt, dass bestimmte Eigenschaften des Eingangssignals wie Fläche und Profil die Parameter der digitalen Aktivierung bestimmen (Aktivierungswahrscheinlichkeit und Populationsheterogenität).

Als letzteres haben wir die Rolle von Oszillationen in der Genekontrolle untersucht. Dies haben wir durch die mikrofluidische Verabreichung periodischer Stimuli unterschiedlicher Frequenz erreicht, welche die NF-kappaB Oszillationen entweder abschwächen oder verstärken. Durch den Vergleich der Genexpression dieser Konditionen konnten wir feststellen, dass ein verstärktes Oszillationssignal eine effiziente Transkription ermöglicht, welches auf die nichtlineare Natur der NF-kappaB-DNA Bindung zurückzuführen ist. Stochastische Modellierung weist darauf hin, dass Signalrauschen (Noise) vorteilhaft für die Realisierung von Entrainment (synchronisierte und verstärkte Oszillationen) unter fluktuierenden Eingangssignalen ist.

Zusammengefasst lernen wir von dieser Arbeit, dass die dynamischen Eigenschaften von Signalnetzwerken nicht willkürlich sind, sondern eine verhaltensspezifische Funktion haben. Während die digitale Aktivierung eine orthogonale Kontrolle über die Anzahl aktivierter Zellen und deren Heterogenität ermöglicht, erlaubt eine oszillierende Kontrolle der Transkription die Wahrnehmung der Frequenz von Umweltfluktuationen. Die genaue Bedeutung dieser Erkenntnisse für spezifische biologische Bedingungen werden in zukünftigen Experimenten noch gezeigt werden müssen. Nichtsdestotrotz konnten wir grundlegende Prinzipien der dynamischen Informationsprozession in der Genregulation und Gewebefunktionen zeigen.

ABSTRACT

Cells face a multitude of environmental cues that change with time and rely on just a few core signaling networks to sense and convert this information to gene expression responses. NF-κB is a gene regulatory network involved in a host of biological processes around cellular stress and inflammation. The pathway has two important dynamic features: 1) Digital activation, meaning that is a threshold level of input is required to trigger all-or-none pathway activation, and 2) Delayed negative feedback leading to oscillations in NF-κB nuclear localization. This thesis uncovers roles of these two dynamic features of the NF-κB network.

First, we establish a microfluidic pipeline for high-throughput analysis of single-cell dynamic signaling. Current methods for studying signaling dynamics at the single-cell level are limited in throughput, precision, and ability to manipulate the cellular microenvironment during live imaging. By investing in a microfluidic approach we solve these issues and enable streamlined collection and analysis of imaging and gene expression data under temporally modulated input.

Second, we explore the function of the switch-like or digital NF-κB response. Cells receive different intensities and durations of input depending on their spatial and biological context. For example, cells close to an infection site may receive a short duration, high intensity inflammatory signal while cells distant to the site experience a sustained but low intensity signal. Combining computation and experimental screening of intensity and duration inputs, we discover that specific features of the input profile (area and shape) determine distinct parameters of the NF-κB switch response (activation probability and population heterogeneity).

Third, we investigate the function of oscillation in gene regulation. To do this we either perturb or enhance NF-κB oscillations by delivering periodic input at different frequencies to the pathway using microfluidics. By comparing gene expression when the NF-κB oscillation is either disrupted or enhanced we discover that an oscillatory mode of gene regulation enables efficient transcription due to the nonlinear nature of NF-κB—DNA binding. Stochastic modeling indicated that noise is beneficial for enabling the NF-κB to entrain (synchronize and enhance oscillation) under fluctuating input.

The message emerging from this work is that dynamic properties of signaling networks are not arbitrary but rather perform specific functions. While digital activation enables orthogonal control over fraction of activating cells and population heterogeneity, oscillatory control of transcription enables sensing frequency of environmental fluctuation to control gene expression. Although implications of these findings in specific biological scenarios will bear out in future work, these initial insights shed light on how the dynamic machine of the cell computes fluctuation in surroundings to coordinate gene regulation and tissue functions.

1. INTRODUCTION

1.1 Cellular information processing

Cells are the basic unit of life and must process signals in their environment and convert these to gene expression responses that implement biological functions. The information processing capacity of cells is huge: environmental signals span a vast space of metabolite, lipid, carbohydrate, and protein molecules that present by diffusion or physical interactions between cells. The combination and intensity of environmental signals fluctuates in time and the basic questions of how cells perform parallel and temporal processing of complex signaling inputs are largely unanswered.

Traditionally information processing in cells is described as follows: a signal activates a specific receptor, initiating a cascade of protein-protein interactions that culminates in the binding of transcription factors to DNA in the nucleus, leading to expression of certain genes. This gene expression leads to the production of proteins that mediate the cellular response to the signal, such as causing differentiation into a more specialized cell type in the case of a morphogen signal or generating an immune response in the case of an infection signal.

However, problems are immediate apparent with the traditional model: There are simply not enough signaling pathways and transcription factors to process all the possible signal types that cells encounter. Cells appeared to rely on just a few core gene regulators, and the traditional model is not sufficient to explain how cells process signals that change in time.

Two features of cellular systems are increasingly appreciated that hint at how cells may solve these problems: 1) the single cells comprising tissues and organisms are inherently dynamic, and while different signals may activate the same signaling pathway, the dynamics of transcription factor activation differ in timescale and temporal pattern; and 2) this gene regulator activation is affected by biochemical noise, leading different cells in a population to show heterogeneity in dynamics.

The current model of cell information processing focuses squarely on the dynamic, stochastic nature of signal transduction, with the core concept that cells “encode” a particular input signal into a specific pattern of dynamic activation, and cells subsequently “decode” these dynamics to regulate expression of a particular set of genes (Werner et al., 2005).

1.2 Encoding: oscillation and stochastic pulsing in signaling systems

Oscillation plays a fundamental role in biological systems across the tree of life, in especially two aspects: for example, circadian rhythms that link organism physiology to time of day, and cells cycle and divide at regular intervals. It is now recognized that oscillation is also ubiquitous in cell signaling. Cell signaling oscillations generally happen at a faster timescale than circadian and cell cycle oscillations and were thus termed ultradian oscillations. Hormones such as cortisol, insulin, and leptin oscillate in the regulation of stress and appetite (Sinha et al., 1996; Walker et al., 2010). Ultradian oscillations were observed to occur in signaling pathways including Stat, Smad, and Hes1 (Kobayashi et al., 2009). Fascinatingly, these

oscillations often occur at harmonic frequencies of the circadian cycle with periods such as 12, 6, and 3 hours. It is therefore tempting to speculate that oscillation is linked across timescales in biological systems.

It has emerged in recent years that dynamic mechanisms of gene regulation play a central role in enabling cells to process complex spatiotemporal signals. As one example, the motif of oscillation and stochastic pulsing of transcription factors appears to be a common mode of genetic control that is conserved across species (Levine et al., 2013a). Specific functions of oscillation, pulsing, and dynamic regulation of gene expression include:

Encoding input intensity using frequency modulation. Multiple signaling systems – including ERK, calcium, NFAT4 and Crz1 in yeast – exhibit frequency modulation, wherein the level of an input controls the frequency of stochastic pulses or oscillations of a transcription factor (TF) into and out of the nucleus (Albeck et al., 2013; Cai et al., 2008; Dolmetsch et al., 1997; Yissachar et al., 2013) . The effect is similar to an analog to digital converter: the analog input signal is converted to discretized pulses of TF activation at a particular frequency. The phenomenon is also seen in neurons, where communication strength between neurons is encoded in the rapidity of action potential firing . However, in this case the frequency modulated signal is used to transmit information between cells rather than transmit a signal to the nucleus and regulate gene expression.

Encoding input type by stimulus-specific dynamic profiles. Different stimulus types that activate the same signaling network may achieve specific gene expression and phenotypic outcomes though distinct temporal dynamics of transcription factor activation. This phenomenon has been demonstrated convincingly in the p53 tumor suppressor system (Liu et al., 2014; Purvis and Lahav, 2013; Wee et al., 2012a). Depending on the mode of DNA damage, whether induced by UV or gamma radiation, p53 exhibits differential dynamics and conversion between either oscillating or steady activation (Purvis et al., 2012). Similarly in the Notch system, a transition from oscillation in Hes1 TF activity to either sustained high or low expression mediates a transition from stem cell self-renewal to differentiation (Imayoshi et al., 2013).

1.3 Decoding: dynamic regulation of gene expression

After a signal is encoded in a dynamic pattern of transcription factor activation, it is then decoded in the nucleus to regulate the induction or suppression of specific genes. Dynamic gene regulation (i.e. oscillation or stochastic pulsing of transcription factors) potentially serves several functional roles for the cells.

Functions of frequency modulation: Conversion of an analog input signal into discrete transcription factor pulses at a frequency depending on the level of input could play several functions for the cell. Different frequencies of oscillation can direct distinct gene expression programs depending on promoter and mRNA stability characteristics (Ashall et al., 2009; Wee et al., 2012b). In calcium signaling, input level changes the frequency of calcium oscillations and this alters the specificity and efficiency of gene expression (Ca, 1998). In ERK signaling, EGF dose determines the frequency of ERK pulses into the

nucleus leading to coordination of proliferation phenotype (Albeck et al., 2013). In the yeast Crz1 network, frequency of stochastic pulsing also depends on input level, and the authors showed that this mechanism of gene regulation allows the system to achieve proportional expression control across multiple genes even when promoters have different activation characteristics (Cai et al., 2008).

Functions of stimulus-specific dynamics. Cells rely on relatively few core signaling pathways to transmit information about a huge diversity of signals, and in general it is not clear how input-output specificity is achieved in gene regulation. In the NF-κB and p53 systems, dynamics of transcription factor activation depend on the type of input (Purvis et al., 2012; Werner et al., 2005). In these systems it was shown that different activation dynamics are sufficient to produce specific responses to a stimulus. Therefore, a single pathway can increase the number of possible outputs though different dynamics of pathway activation.

In general, how different transcription factor dynamics achieve specific gene regulatory actions is not yet fully understood. Modeling studies show that due to the cooperative nature of transcription factor binding to DNA, an oscillatory compared to nonoscillatory regulatory mode can produce either higher or lower gene expression output (Wee et al., 2012b). NF-κB and p53 both regulate hundreds of target genes, and further, oscillatory transcription factor activity can generate distinct patterns of gene activation across multiple transgenes (Wee et al., 2012b).

Overall, while initial findings support that these features enable stimulus specific coordination of distinct programs of gene control across target genes, the mechanisms and functions of oscillation and stochastic pulsing in transcription are still emerging. In this work we focus on the hypothesis that dynamic features of gene regulatory networks also function to transmit information about temporal information in the input signal. For this we focus on the NF-κB system, which is central to inflammatory responses and implicated in many diseases.

1.4 NF-κB: a core signal processing circuit in immunity and disease

NF-κB was discovered serendipitously by Ranjan Sen and David Baltimore in 1986 when looking for transcription factors that regulate B cell antibody maturation (Baltimore, 2009; Sen and Baltimore, 1986). NF-κB was named as it was because it was a nuclear factor that was bound to the κ light chain antibody enhancer in B cells. They found that NF-κB could be induced without requiring transcription, leading to the finding that NF-κB is held in a ready state in the cytoplasm but bound to an inhibitor protein. This inhibitor protein was named IκB (Baeuerle and Baltimore, 1988).

After an NF-κB ligand such as TNF binds its receptor, IκB is phosphorylated and tagged for proteosomal degradation by IKK (IκB Kinase). IKK has since turned out to be a major signaling “hub”, and it is activated by a wide range of ligands including cytokines (such as Tumor Necrosis Factor or TNF), pathogen molecules (such as lipopolysaccharide or LPS), antibodies, and other stimuli associated with cell stress including reactive oxygen species, DNA damage, and mechanical sheer (Figure 1). Although NF-κB turned out to be important in B cell antibody maturation, it is expressed in nearly all cell types and acts as broadly as a critical mediator of the innate immune response (Gerondakis et al., 2014; Hayden and

Ghosh, 2008). Further, NF-κB is involved in lymphocyte activation, neurobiology, and centrally implicated in diseases such as cancer and autoimmunity (Baker et al., 2011; Hayden and Ghosh, 2008; Meffert and Baltimore, 2005; Oh and Ghosh, 2013).

Following IKK activation, IκB degradation exposes a nuclear localization sequence on NF-κB leading to its translocation to the nucleus where NF-κB orchestrates the regulation of hundreds of genes. NF-κB dependent genes are typically grouped depending on timescale of regulation with "early" genes upregulated in 15-60 minutes, "middle" genes activated within 2-4 hours, and "late" reaching maximal activation in 8-12 hours (Hao and Baltimore, 2013; Tay et al., 2010).

Following the initial discovery, the complete network of proteins that interact with and regulate the activity of NF-κB has been systematically worked out (Hoffmann et al., 2002). The network of interacting proteins that determine NF-κB activation is analogous to an electronic circuit (Figure 1). We now discuss two dynamic elements of the NF-κB network that similarly appear in electronic circuits: 1) a switch, and 2) an oscillator.

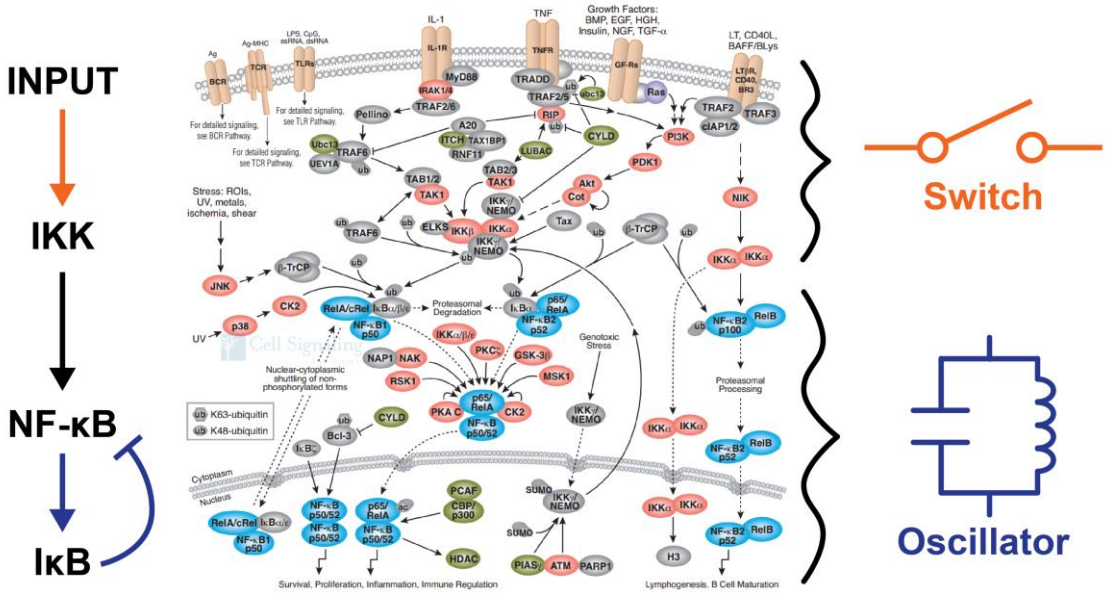

Figure 1. Modules of the NF-κB circuit. NF-κB can be divided in two parts: an "upstream" part encompassing signaling from the input and receptor level to activation to IKK, and a "downstream" part that includes the NF-κB/IκB feedback module. The upstream part functions as a switch, such that a threshold must be exceeded for pathway activation to occur. The downstream part includes activation of NF-κB and gene regulation and functions as an oscillator, due to delayed negative feedback of IκB on NF-κB.

1.4.1 NF-κB circuit elements: switch-like (digital) activation

After receptor binding of an NF-κB inducing molecule such as LPS or TNF, adaptor proteins are recruited to the cell membrane. These adaptor proteins assemble into a higher-order molecular complex that subsequently mediates IKK activation (Lin et al., 2010; Wu, 2013). The formation of higher-order molecular complexes is inherently cooperative, meaning that assembly initiation facilitates further growth of the complex (Wu, 2013). This coopertivity leads to nonlinear, switch-like kinetics of IKK activation and effectively a threshold in the amount of receptor signal needed to trigger IKK (Shinohara et al., 2014).

As a consequence, the NF-κB pathways activates in a digital, switch-like fashion such that cells either fully activate NF-κB or not at all (Tay et al., 2010). Importantly, the threshold for pathway activation varies between cells due to different levels of receptor expression. As a consequence, increasing dose of stimulation to the pathway leads to an increasing fraction of cells in the population that respond, without significantly impacting the amplitude of the response (Tay et al., 2010).

The mode of "digital" pathway activation (as opposed to "analog" activation where increasing input dose leads to a proportional increase in response amplitude) is also observed in signaling pathways such as ERK/MAPK (von Kriegsheim et al., 2009a; Malleshaiah et al., 2010; Petty et al., 1998). Interestingly, whether pathway activation is digital or analog can depend on cell type, suggesting that switch-like activation is a tunable parameters to impact how cell populations respond to stimuli (Aoki et al., 2011).

1.4.2 NF-κB circuit elements: oscillation and noise

Among the genes most rapidly induced by NF-κB is in fact IκB, forming a negative feedback loop (Hoffmann et al., 2002). So although the intial IκB pool was degraded to allow activation of NF-κB, the supply is quickly refilled. This newly synthesized IκB rebinds NF-κB in the nucleus leading to export from the nucleus back to the cytoplasm. If active IKK is still present in the cytoplasm, IκB bound to NF-κB is again degraded and the cycle repeats, leading to oscillations in NF-κB between the cytoplasm and nucleus.

Although IκB negative feedback was realized soon after discovery of NF-κB, for many years oscillations in the pathway were not identified due to use of bulk cell assays in measuring transcriptional activity (Hoffmann et al., 2002). Importantly, dynamics and oscillations are highly variable or heterogeneous between cells in the population, and therefore the appearance of oscillation is generally lost in population assays when the cell responses are averaged. It was only in 2004 when live fluorescence imaging first revealed the extent of NF-κB oscillation in single cells (Nelson 2004).

1.5 Biological noise

Heterogeneity in NF-κB dynamics arises from biological noise. Noise is fundamental to the natural stochastic nature of biochemical molecular interactions (Hornung and Barkai, 2008). When reactions involve low number of molecules, molecular collision resulting in a reaction may occur variably and infrequently, and this variability in collision timing propagates in subsequent reactions. For example, in

processes such as transcription, NF-κB molecules interaction with only two gene loci on DNA, and transcription tends to occur in bursts of mRNA production. Because the timing of these bursts is infrequent this leads to variability in level of IκB protein which causes variability in oscillation dynamics of NF-κB. The noise arising from biochemical interactions is referred to as *intrinsic noise* (Elowitz et al., 2002; Levine et al., 2013b). Over a long timescale spanning multiple cell divisions, intrinsic noise propagates to effects on differences in the level of key signaling species between cells such as differences in receptor number, leading to cell-cell variability in aspects such as signaling pathway sensitivity and also properties such as oscillation frequency (Elowitz et al., 2002; Hornung and Barkai, 2008). This long-standing difference in protein species or organelles between cells is referred to as *extrinsic noise* (Elowitz et al., 2002).

Noise intuitively seems that it would be detrimental in biological systems due to causing uncertainty in how cells will behave in response to a signal. However, evolution occurs in the context of noise, and a number of positive functions for noise have been identified in diverse processes including cell differentiation and neurobiology (Eldar and Elowitz, 2010; McDonnell and Ward, 2011).

1.6 Hypothesis: how cells process temporal information

Although most in vitro studies of cell signaling are conducted under non-changing input conditions, in real biological contexts cells see highly dynamic and fluctuating levels of environmental signals, due to signals from neighbor cells or from circulation. It is well established that concentration level of a signal influences cell behavior and fate with examples in development, inflammatory response, etc. However it is not clear how cells make use of information contained in the dynamics of fluctuations of concentration of an input, which could provide information for example about spatial context (Warmflash et al., 2012). The hypothesis underlying this work is that dynamic network motifs such as oscillation and digital activation facilitate processing of temporal (i.e. frequency, duration) information in signaling inputs.

1.7 Tools for dynamic cell signaling analysis at single-cell resolution

Addressing fundamental questions in how cells process information requires A) measuring responses real-time in living cells, B) at the resolution of single cells, and with C) precise spatiotemporal control of the cellular signaling environment.

1.7.1 Live cell fluorescence imaging

Live cell imaging of fluorescent reporter constructs was a revolutionary advance that enabled observation of signaling dynamics in single cells, revealing for the first time the extent of noise and heterogeneity in dynamics between cells in their response and also phenomena such as oscillations and digital activation (Spiller et al., 2010).

At the time of the discovery of NF-κB the state of the art of the art was to use electrophoretic mobility shift assays (EMSA) to measure transcription factor translocation into the nucleus (Hoffmann and Baltimore, 2006). Because this was a population average measurement, it was not possible to see

oscillations in NF-κB dynamics. The use of live cell fluorescence microscopy was required to see dynamics of single cells and observe complex pathway dynamics.

Live fluorescent imaging works by genetically fusing a fluorescent protein to cellular protein of interest on the 5 or 3' end of the protein. The protein fusion then emits fluorescence revealing the localization and concentration of the protein in the cell. For the case of NF-κB, expression of NF-κB is essentially unchanging in time, activity of the protein depends rather on amount of NF-κB localized in the nucleus. By observing the movement of NF-κB in and out of the nucleus, researchers discovered oscillatory dynamics in the pathway that is highly heterogeneous between cells (Nelson 2004). Oscillation and dynamic heterogeneity is now observed in many signaling pathways (Purvis and Lahav, 2013).

One issue with engineering fluorescent protein tagging constructs is how they are delivered and expressed in cells. Transient transfection allows different expression levels of the construct in different cells to see how expression level impacts signaling. Stable genomic integration of a construct helps to reduce variability in construct expression between cells. Interestingly, this variability can still develop through differences in epigenetic modifications that develop between cells (Spiller et al., 2010).

Until recently it has been difficult to avoid expression the tagged version of the protein at levels exceeding the natural expression level of the protein, leading to possible artifacts (Nelson et al., 2004). This was addressed only through using recombinant mouse technology and design of a fluorescent fusion knock-in mouse line (Zambrano et al., 2014). However, development of such mice is expensive and time consuming. The discovery of CRISPR has now made it much easier to introduce florescent proteins knocked-in to the endogeneous gene locus, enabling control of fluorescent protein fusion expression under the endogenous transcriptional control for the protein and avoiding artifacts related to use of synthetic promoters and overexpression (Mali et al., 2013).

1.7.2 Microfluidic cell culture

Asking how cells process signals that change in time requires the ability to deliver time-evolving inputs. Moreover, since the space of inputs that change in time is large, it is necessary to develop high-throughput ways to test this. Since stimulated cells can subsequently release proteins and soluble signals that communicate with neighbor cells, it is necessary to avoid convective mixing that could disturb the diffusion field between cells. All of these issues are addressed through the use of microfluidics, which engineers fluidic structures on the size scale of single cells and allows high-throughput testing of arbitrary input conditions with temporal input patterns (Tay et al., 2010; Whitesides, 2006)

Microfluidic functionality is achieved using two microfluidic layers, a flow and control layer. The flow layer contains fluids and cells in the experiment. The control layer creates microfluidic valves in the flow layer by pushing on the flow and pinching off flow at precise locations on the chip. With this design insight it has been possible to engineer chips with features similar to those of an integrated electronic circuit, with increasing complexity and develop specialized functions such as pumping, gradients, etc (Scha et al., 2002).

Microfluidic chips are fabricated using standard photolithography techniques to pattern positive and negative photoresists on silicon wafers. These photoresist patterns are then used to mold chip layers from polydimethylsiloxane (PDMS). Layers are bonded and holes punched so that on-chip channels are accessible by external tubing, and the chip bonded to a glass slide for imaging on the microscope (Iliescu et al., 2012). Chips are externally actuated using electronic solenoid valves connected to pressure sources that actuate specific valves on the chip through electronic control via a Matlab or Labview interface. Microfluidics has advanced cell culture from simple cell monolayers to complex cell organization mimicking tissues and organs (Bhatia and Ingber, 2014)

1.7.3 High-throughput gene expression analysis

Beyond improved capabilities around cell culture control and stimulation, microfluidics provides revolutionary advances in sensitivity and throughput of biochemical assays including measurement of nucleic acids. Real-time PCR amplifies and simultaneously detects and quantifies a gene product. Microfluidics enables reducing the reaction volume for these assays by orders of magnitude and thereby improving sensitivity in mRNA detection (Hong et al., 2004). This increased sensitivity enables detection of mRNA molecules from single mammalian and bacterial cells (Marcus et al., 2006; Sanchez-Freire et al., 2012). Moreover, microfluidic approaches can perform combinatorial tests of a panel of gene primers against a series of biological samples in reaction arrays – for example, in a 48×48 or 96×96, enabling 2304 and 9216 PCR reactions respectively without increased pipette steps – for vastly increased throughput (Knutson et al., 2013).

One limitation of real-time PCR is that it is estimates the abundance of a nucleic acid based on the rate of amplification and is therefore a relative measurement subject to amplification bias. An ideal measurement method would quantify absolute number of mRNA species. This is achieved using microfluidics to divide an uncertain number of mRNA molecules into a large number of reaction chambers such that each chamber contains either zero or one molecule. An amplification reaction in each chamber then is then positive or negative for the presence of the target molecule allowing counting and absolute quantification of molecule number. This method has become known as “digital PCR” and has been successfully implemented in both valve and droplet based microfluidic systems (Beer et al., 2008; Leman et al., 2014; Warren et al., 2006).

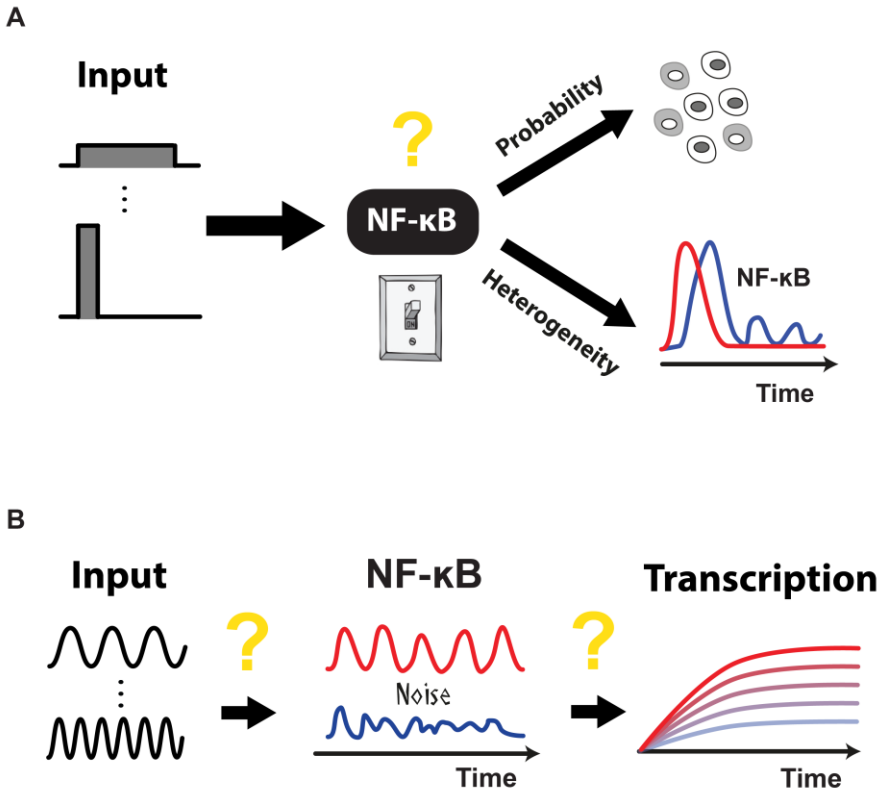

Figure 2. Identifying functions of the NF-κB switch and oscillator. A) By screening different combinations of input dose and duration – leading to comparison of weak-sustained and intense-brief input profiles – we explore how the NF-κB switch regulates both the probability and heterogeneity of responses in the population. B) Using periodic input to NF-κB enables examining how the system processes frequency content in the input. Though analysis of mRNA output we measure importance of oscillation in the transcription regulatory function of NF-κB.

1.8 Aims of the thesis

This thesis investigates how dynamic features of the NF-κB pathway function to process temporal information in signaling inputs. First, we establish a microfluidic pipeline to address limitations in current technology for studying single-cell dynamic signaling under temporally modulated input. Next, we apply this pipeline to understand functions for digital activation and oscillation in the NF-κB response.

1.8.1 Establish a robust microfluidics pipeline for single-cell analysis

The first goal is to establish a microfluidic pipeline in the lab for single-cell analysis that enables live imaging and gene expression measurements under concurrent modulation of the cellular microenvironment. Critical issues to address are how to achieve robust long-term culture of a variety of

cell types, how to extract cells or lysate from the chip for downstream high-throughput gene expression analysis, and how to achieve automated and fast analysis of imaging and gene expression data.

1.8.2 Dissect dynamics and function of the NF-κB switch

Although the NF-κB response is well understood to be switch-like or digital, it is not understood how dose and duration of the input are integrated to determine switch activation. Moreover, the larger question of why switch-like response is beneficial is also not addressed. In this part we aim to address these questions through experiment and modeling to screen the dose-duration input space to characterize NF-κB switch dynamics and better understand how the switch functions to determine the collective NF-κB responses in a cell population.

1.8.3 Determine role of noise and oscillation in gene regulation

Although signaling is typically studied in unchanging conditions, in vivo biological signals are in general not static but rather dynamic and fluctuating. NF-κB oscillation controls transcription, but it is not clear how or why. We use a microfluidic approach to stimulate NF-κB using periodic input, which either disturbs or enhances the NF-κB oscillation depending on the input frequency. By studying gene expression under these two cases we dissect how oscillation in NF-κB nuclear localization controls transcription. Noise is a critical aspect of oscillation and it is not understood to what extent noise impacts oscillation and NF-κB transcriptional output. Using modeling together with experimental data we address how synergy between oscillation and noise mediates the NF-κB response under periodic input.

1.9 References

Adachi, S., and Iwata, M. (2002). Duration of calcineurin and Erk signals regulates CD4/CD8 lineage commitment of thymocytes. Cell. Immunol. *215*, 45–53.

Ahmed, S., Grant, K.G., Edwards, L.E., Rahman, A., Cirit, M., Goshe, M.B., and Haugh, J.M. (2014). Data-driven modeling reconciles kinetics of ERK phosphorylation, localization, and activity states. Mol. Syst. Biol. *10*, 718.

Albeck, J.G., Mills, G.B., and Brugge, J.S. (2013). Frequency-Modulated Pulses of ERK Activity Transmit Quantitative Proliferation Signals. Mol. Cell *49*, 249–261.

Altan-Bonnet, G., and Germain, R.N. (2005). Modeling T cell antigen discrimination based on feedback control of digital ERK responses. PLoS Biol. *3*, 1925–1938.

Aoki, K., Yamada, M., Kunida, K., Yasuda, S., and Matsuda, M. (2011). Processive phosphorylation of ERK MAP kinase in mammalian cells. Proc. Natl. Acad. Sci. U. S. A. *108*, 12675–12680.

Arumugam, M., Raes, J., Pelletier, E., Le Paslier, D., Yamada, T., Mende, D.R., Fernandes, G.R., Tap, J., Bruls, T., Batto, J.-M., et al. (2011). Enterotypes of the human gut microbiome. Nature *473*, 174–180.

Ashall, L., Horton, C. a, Nelson, D.E., Paszek, P., Harper, C. V, Sillitoe, K., Ryan, S., Spiller, D.G., Unitt, J.F., Broomhead, D.S., et al. (2009). Pulsatile stimulation determines timing and specificity of NF-kappaB-dependent transcription. Science *324*, 242–246.

Baeuerle, P. a, and Baltimore, D. (1988). Activation of DNA-binding activity in an apparently cytoplasmic precursor of the NF-kappa B transcription factor. Cell *53*, 211–217.

Bagowski, C.P., and Ferrell, J.E. (2001). Bistability in the JNK cascade. Curr. Biol. *11*, 1176–1182.

Baker, R.G., Hayden, M.S., and Ghosh, S. (2011). NF-κB, inflammation, and metabolic disease. Cell Metab. *13*, 11–22.

Baltimore, D. (2009). Discovering NF- k B. 1–4.

Beer, N.R., Wheeler, E.K., Lee-Houghton, L., Watkins, N., Nasarabadi, S., Hebert, N., Leung, P., Arnold, D.W., Bailey, C.G., and Colston, B.W. (2008). On-chip single-copy real-time reverse-transcription PCR in isolated picoliter droplets. Anal. Chem. *80*, 1854–1858.
Behar, M., and Hoffmann, A. (2013). Tunable signal processing through a kinase control cycle: The IKK signaling node. Biophys. J. *105*, 231–241.
Behar, M., Barken, D., Werner, S.L., and Hoffmann, A. (2013). Theory The Dynamics of Signaling as a Pharmacological Target. Cell *155*, 448–461.
Bhatia, S.N., and Ingber, D.E. (2014). Microfluidic organs-on-chips. Nat. Biotechnol. *32*, 760–772.
Ca, A. (1998). Calcium oscillations increase the efficiency and specificity of gene expression. *392*, 933–936.
Cai, L., Dalal, C.K., and Elowitz, M.B. (2008). Frequency-modulated nuclear localization bursts coordinate gene regulation. Nature *455*, 485–490.
Dolmetsch, R.E., Lewis, R.S., Goodnow, C.C., and Healy, J.I. (1997). Differential activation of transcription factors induced by Ca2+ response amplitude and duration. Nature *386*, 855–858.
Eldar, A., and Elowitz, M.B. (2010). Functional roles for noise in genetic circuits. Nature *467*, 167–173.
Elowitz, M.B., Levine, A.J., Siggia, E.D., and Swain, P.S. (2002). Stochastic gene expression in a single cell. Sci. Signal. *297*, 1183.
Fu, Y., Lim, S., Urano, D., Tunc-ozdemir, M., Phan, N.G., and Elston, T.C. (2014). Theory Reciprocal Encoding of Signal Intensity and Duration in a Glucose-Sensing Circuit. Cell *156*, 1084–1095.
Furusawa, Y., Obata, Y., Fukuda, S., Endo, T. a, Nakato, G., Takahashi, D., Nakanishi, Y., Uetake, C., Kato, K., Kato, T., et al. (2013). Commensal microbe-derived butyrate induces the differentiation of colonic regulatory T cells. Nature *504*, 446–450.
Gerondakis, S., Fulford, T.S., Messina, N.L., and Grumont, R.J. (2014). NF-κB control of T cell development. Nat. Immunol. *15*, 15–25.
Gómez-Sjöberg, R., Leyrat, A. a., Pirone, D.M., Chen, C.S., and Quake, S.R. (2007). Versatile, fully automated, microfluidic cell culture system. Anal. Chem. *79*, 8557–8563.
Gottschalk, R. a., Hathorn, M.M., Beuneu, H., Corse, E., Dustin, M.L., Altan-Bonnet, G., and Allison, J.P. (2012). Distinct influences of peptide-MHC quality and quantity on in vivo T-cell responses. Proc. Natl. Acad. Sci. *109*, 881–886.
Han, Q., Bagheri, N., Bradshaw, E.M., Hafler, D. a., Lauffenburger, D. a., and Love, J.C. (2012). From the Cover: Polyfunctional responses by human T cells result from sequential release of cytokines. Proc. Natl. Acad. Sci. *109*, 1607–1612.
Hao, S., and Baltimore, D. (2013). RNA splicing regulates the temporal order of TNF-induced gene expression. Proc. Natl. Acad. Sci. U. S. A. *110*, 11934–11939.
Hayden, M.S., and Ghosh, S. (2008). Shared Principles in NF-kB Signaling. Cell *132*, 344–362.
Hoffmann, A., and Baltimore, D. (2006). Circuitry of nuclear factor kappaB signaling. Immunol. Rev. *210*, 171–186.
Hoffmann, A., Levchenko, A., Scott, M.L., and Baltimore, D. (2002). The IkappaB-NF-kappaB signaling module: temporal control and selective gene activation. Science *298*, 1241–1245.
Hong, J.W., Studer, V., Hang, G., Anderson, W.F., and Quake, S.R. (2004). A nanoliter-scale nucleic acid processor with parallel architecture. Nat. Biotechnol. *22*, 435–439.
Hornung, G., and Barkai, N. (2008). Noise propagation and signaling sensitivity in biological networks: a role for positive feedback. PLoS Comput. Biol. *4*, e8.
Hughey, J.J., Gutschow, M. V, Bajar, B.T., and Covert, M.W. (2014). Single-cell variation leads to population invariance in NF- κB signaling dynamics.
Huh, D., Kim, H.J., Fraser, J.P., Shea, D.E., Khan, M., Bahinski, A., Hamilton, G. a, and Ingber, D.E. (2013). Microfabrication of human organs-on-chips. Nat. Protoc. *8*, 2135–2157.
Iezzi, G., Karjalainen, K., and Lanzavecchia, A. (1998). The Duration of Antigenic Stimulation Determines the Fate of Naive and Effector T Cells. Immunity *8*, 89–95.
Iliescu, C., Taylor, H., Avram, M., Miao, J., and Franssila, S. (2012). A practical guide for the fabrication of microfluidic devices using glass and silicon. Biomicrofluidics *6*, 16505–1650516.

Imayoshi, I., Isomura, A., Harima, Y., Kawaguchi, K., Kori, H., Miyachi, H., Fujiwara, T., Ishidate, F., and Kageyama, R. (2013). Oscillatory control of factors determining multipotency and fate in mouse neural progenitors. Science *342*, 1203–1208.
Junkin, M., and Tay, S. (2014). Microfluidic single-cell analysis for systems immunology. Lab Chip *14*, 1246–1260.
Kazmierczak, B., and Lipniacki, T. (2010). Spatial gradients in kinase cascade regulation. IET Syst. Biol. *4*, 348–355.
Kellogg, R.A., and Tay, S. (2015). Noise Facilitates Transcriptional Control under Dynamic Inputs. Cell *160*, 381–392.
Kellogg, R.A., Gómez-Sjöberg, R., Leyrat, A.A., and Tay, S. (2014). High-throughput microfluidic single-cell analysis pipeline for studies of signaling dynamics. Nat. Protoc. *9*, 1713–1726.
Kingeter, L.M., Paul, S., Maynard, S.K., Cartwright, N.G., and Schaefer, B.C. (2010). Cutting edge: TCR ligation triggers digital activation of NF-kappaB. J. Immunol. *185*, 4520–4524.
Knutson, C.G., Mangerich, A., Zeng, Y., Raczynski, A.R., Liberman, R.G., Kang, P., Ye, W., Prestwich, E.G., Lu, K., Wishnok, J.S., et al. (2013). Chemical and cytokine features of innate immunity characterize serum and tissue profiles in inflammatory bowel disease. Proc. Natl. Acad. Sci. U. S. A. *110*, E2332–E2341.
Kobayashi, T., Mizuno, H., Imayoshi, I., Furusawa, C., Shirahige, K., and Kageyama, R. (2009). The cyclic gene Hes1 contributes to diverse differentiation responses of embryonic stem cells. 1870–1875.
Von Kriegsheim, A., Baiocchi, D., Birtwistle, M., Sumpton, D., Bienvenut, W., Morrice, N., Yamada, K., Lamond, A., Kalna, G., Orton, R., et al. (2009a). Cell fate decisions are specified by the dynamic ERK interactome. Nat. Cell Biol. *11*, 1458–1464.
Von Kriegsheim, A., Baiocchi, D., Birtwistle, M., Sumpton, D., Bienvenut, W., Morrice, N., Yamada, K., Lamond, A., Kalna, G., Orton, R., et al. (2009b). Cell fate decisions are specified by the dynamic ERK interactome. Nat. Cell Biol. *11*, 1458–1464.
Lee, T.K., Denny, E.M., Sanghvi, J.C., Gaston, J.E., Maynard, N.D., Hughey, J.J., and Covert, M.W. (2009). A noisy paracrine signal determines the cellular NF-kappaB response to lipopolysaccharide. Sci. Signal. *2*, ra65.
Leman, M., Abouakil, F., Griffiths, A.D., and Tabeling, P. (2014). Droplet-based microfluidics at the femtolitre scale. Lab Chip.
Levine, J.H., Lin, Y., and Elowitz, M.B. (2013a). Functional roles of pulsing in genetic circuits. Science *342*, 1193–1200.
Levine, J.H., Lin, Y., and Elowitz, M.B. (2013b). Functional roles of pulsing in genetic circuits. Science *342*, 1193–1200.
Lin, S.-C., Lo, Y.-C., and Wu, H. (2010). Helical assembly in the MyD88-IRAK4-IRAK2 complex in TLR/IL-1R signalling. Nature *465*, 885–890.
Lipniacki, T., Puszynski, K., Paszek, P., Brasier, A.R., and Kimmel, M. (2007). Single TNFalpha trimers mediating NF-kappaB activation: stochastic robustness of NF-kappaB signaling. BMC Bioinformatics *8*, 376.
Liu, B., Bhatt, D., Oltvai, Z.N., Greenberger, J.S., and Bahar, I. (2014). Significance of p53 dynamics in regulating apoptosis in response to ionizing radiation, and polypharmacological strategies. Sci. Rep. *4*, 6245.
Liu, T., Yamaguchi, Y., Shirasaki, Y., Shikada, K., Yamagishi, M., Hoshino, K., Kaisho, T., Takemoto, K., Suzuki, T., Kuranaga, E., et al. (2013). Single-Cell Imaging of Caspase-1 Dynamics Reveals an All-or-None Inflammasome Signaling Response. Cell Rep. *8*, 974–982.
Mali, P., Yang, L., Esvelt, K.M., Aach, J., Guell, M., DiCarlo, J.E., Norville, J.E., and Church, G.M. (2013). RNA-guided human genome engineering via Cas9. Science *339*, 823–826.
Malleshaiah, M.K., Shahrezaei, V., Swain, P.S., and Michnick, S.W. (2010). The scaffold protein Ste5 directly controls a switch-like mating decision in yeast. Nature *465*, 101–105.
Marcus, J.S., Anderson, W.F., and Quake, S.R. (2006). Microfluidic single-cell mRNA isolation and analysis. Anal. Chem. *78*, 3084–3089.

McDonnell, M.D., and Ward, L.M. (2011). The benefits of noise in neural systems: bridging theory and experiment. Nat. Rev. Neurosci. *12*, 415–426.
Meffert, M.K., and Baltimore, D. (2005). Physiological functions for brain NF-kappaB. Trends Neurosci. *28*, 37–43.
Miskov-Zivanov, N., Turner, M.S., Kane, L.P., Morel, P. a, and Faeder, J.R. (2013). The duration of T cell stimulation is a critical determinant of cell fate and plasticity. Sci. Signal. *6*, ra97.
Negro, A., Dodge-Kafka, K., and Kapiloff, M.S. (2008). Signalosomes as therapeutic targets. Prog. Pediatr. Cardiol. *25*, 51–56.
Nelson, D.E., Ihekwaba, A.E.C., Elliott, M., Johnson, J.R., Gibney, C.A., Foreman, B.E., Nelson, G., See, V., Horton, C.A., Spiller, D.G., et al. (2004). Oscillations in NF-kappaB signaling control the dynamics of gene expression. Science *306*, 704–708.
Oh, H., and Ghosh, S. (2013). NF- j B: roles and regulation in different CD4 + T-cell subsets. 41–51.
Pantazis, P., and Supatto, W. (2014). Advances in whole-embryo imaging: a quantitative transition is underway. Nat. Rev. Mol. Cell Biol. *15*, 327–339.
Paszek, P., Ryan, S., Ashall, L., Sillitoe, K., Harper, C. V, Spiller, D.G., Rand, D. a, and White, M.R.H. (2010). Population robustness arising from cellular heterogeneity. Proc. Natl. Acad. Sci. U. S. A. *107*, 11644–11649.
Pękalski, J., Zuk, P.J., Kochańczyk, M., Junkin, M., Kellogg, R., Tay, S., and Lipniacki, T. (2013). Spontaneous NF-κB activation by autocrine TNFα signaling: A computational analysis. PLoS One *8*.
Petty, M.C., Introduc-, L.F.A., Aca-, F.L.S., Clays, K., Armstrong, N.J., Jr, J.E.F., and Machleder, E.M. (1998). The Biochemical Basis of an All-or-None Cell Fate Switch in Xenopus Oocytes. *280*, 895–899.
Purvis, J.E., and Lahav, G. (2013). Encoding and decoding cellular information through signaling dynamics. Cell *152*, 945–956.
Purvis, J.E., Karhohs, K.W., Mock, C., Batchelor, E., Loewer, A., and Lahav, G. (2012). P53 Dynamics Control Cell Fate. Science *336*, 1440–1444.
Sanchez-Freire, V., Ebert, A.D., Kalisky, T., Quake, S.R., and Wu, J.C. (2012). Microfluidic single-cell real-time PCR for comparative analysis of gene expression patterns. Nat. Protoc. *7*, 829–838.
Santos, S.D.M., Verveer, P.J., and Bastiaens, P.I.H. (2007). Growth factor-induced MAPK network topology shapes Erk response determining PC-12 cell fate. Nat. Cell Biol. *9*, 324–330.
Scha, R., Okuno, T., Hassdorf, R., Shigeto, K., Ono, T., Bode, M., Pietzsch, O., Wiesendanger, R., Getzlaff, M., Wiesendanger, R., et al. (2002). Microfluidic Large-Scale Integration. *4437*.
Selimkhanov, J., Taylor, B., Yao, J., Pilko, A., Albeck, J., Hoffmann, A., Tsimring, L., and Wollman, R. (2014). Systems biology. Accurate information transmission through dynamic biochemical signaling networks. Science *346*, 1370–1373.
Sen, R., and Baltimore, D. (1986). Multiple nuclear factors interact with the immunoglobulin enhancer sequences. Cell *46*, 705–716.
Shah, N. a, and Sarkar, C. a (2011). Robust network topologies for generating switch-like cellular responses. PLoS Comput. Biol. *7*, e1002085.
Shinohara, H., Behar, M., Inoue, K., Hiroshima, M., Yasuda, T., Nagashima, T., Kimura, S., Sanjo, H., Maeda, S., Yumoto, N., et al. (2014). Positive feedback within a kinase signaling complex functions as a switch mechanism for NF-κB activation. Science *344*, 760–764.
Sinha, M.K., Sturis, J., Ohannesian, J., Magosin, S., Caro, F., Stephens, T., Heiman, M.L., and Polonsky, K.S. (1996). Ultradian Oscillations of Leptin Secretion in Humans between midnight and early morning hours and lowest around noon to mid-afternoon . In the. Biochem. Biophys. Res. Commun. *738*, 733–738.
Spiller, D.G., Wood, C.D., Rand, D. a, and White, M.R.H. (2010). Measurement of single-cell dynamics. Nature *465*, 736–745.
Tay, S., Hughey, J.J., Lee, T.K., Lipniacki, T., Quake, S.R., and Covert, M.W. (2010). Single-cell NF-kappaB dynamics reveal digital activation and analogue information processing. Nature *466*, 267–271.
Walker, J.J., Terry, J.R., and Lightman, S.L. (2010). Origin of ultradian pulsatility in the hypothalamic-pituitary-adrenal axis. Proc. Biol. Sci. *277*, 1627–1633.

Warmflash, A., Zhang, Q., Sorre, B., Vonica, A., Siggia, E.D., and Brivanlou, A.H. (2012). Dynamics of TGF-β signaling reveal adaptive and pulsatile behaviors reflected in the nuclear localization of transcription factor Smad4. Proc. Natl. Acad. Sci. U. S. A. *109*, E1947–E1956.
Warren, L., Bryder, D., Weissman, I.L., and Quake, S.R. (2006). Transcription factor profiling in individual hematopoietic progenitors by digital RT-PCR. Proc. Natl. Acad. Sci. U. S. A. *103*, 17807–17812.
Wee, K.B., Yio, W.K., Surana, U., and Chiam, K.H. (2012a). Transcription factor oscillations induce differential gene expressions. Biophys. J. *102*, 2413–2423.
Wee, K.B., Yio, W.K., Surana, U., and Chiam, K.H. (2012b). Transcription factor oscillations induce differential gene expressions. Biophys. J. *102*, 2413–2423.
Werner, S.L., Barken, D., and Hoffmann, A. (2005). Stimulus specificity of gene expression programs determined by temporal control of IKK activity. Science *309*, 1857–1861.
Whitesides, G.M. (2006). The origins and the future of microfluidics. Nature *442*, 368–373.
Wu, H. (2013). Essay Higher-Order Assemblies in a New Paradigm of Signal Transduction. 287–292.
Yang, H., Wang, H., Shivalila, C.S., Cheng, A.W., Shi, L., and Jaenisch, R. (2013). Resource One-Step Generation of Mice Carrying Reporter and Conditional Alleles by CRISPR / Cas-Mediated Genome Engineering. Cell *154*, 1370–1379.
Yin, Q., Lin, S.-C., Lamothe, B., Lu, M., Lo, Y.-C., Hura, G., Zheng, L., Rich, R.L., Campos, A.D., Myszka, D.G., et al. (2009). E2 interaction and dimerization in the crystal structure of TRAF6. Nat. Struct. Mol. Biol. *16*, 658–666.
Yissachar, N., Fischler, T.S., Cohen, A.A., Reich-zeliger, S., Russ, D., Shifrut, E., and Porat, Z. (2013). Short Article Dynamic Response Diversity of NFAT Isoforms in Individual Living Cells. Mol. Cell *49*, 322–330.
Zambrano, S., Bianchi, M.E., and Agresti, A. (2014). High-throughput analysis of NF-κB dynamics in single cells reveals basal nuclear localization of NF-κB and spontaneous activation of oscillations. PLoS One *9*, e90104.
Zanoni, I., Ostuni, R., Marek, L.R., Barresi, S., Barbalat, R., Barton, G.M., Granucci, F., and Kagan, J.C. (2011). CD14 Controls the LPS-Induced Endocytosis of Toll-like Receptor 4. Cell *147*, 868–880.

2. HIGH-THROUGHPUT MICROFLUIDIC SINGLE-CELL ANALYSIS PIPELINE FOR STUDIES OF SIGNALING DYNAMICS

This chapter published in *Nature Protocols*: Kellogg, R. A., Gómez-Sjöberg, R., Leyrat, A., and Tay, S. (2014). High-throughput microfluidic single-cell analysis pipeline for studies of signaling dynamics. Nat. Protoc. *9*, 1713–1726. doi:10.1038/nprot.2014.120

Ryan A. Kellogg[1], Rafael Gómez-Sjöberg[2], Anne A. Leyrat[3], Savaş Tay[1*]

[1]Dept. Biosystems Science and Engineering, ETH Zürich, Switzerland 4058.
[2]Dept. of Bioengineering, Stanford University, Stanford, CA 94305. Currently at Quanticel Pharmaceuticals, San Francisco, CA 94158
[3]Dept. of Bioengineering, Stanford University, Stanford, CA 94305. Currently at Fluidigm Corporation, South San Francisco, CA 94080

[*]Correspondence to: savas.tay@bsse.ethz.ch

R.A.K. developed methods for robust long-duration cell culture and gene expression measurements under dynamic on-chip stimulation, and wrote the protocol and manuscript.

Abstract

Time-dependent analysis of dynamic processes in single live cells is a revolutionary technique for the quantitative studies of signaling networks. Here, we describe an experimental pipeline and associated protocol that incorporate microfluidic cell culture, precise stimulation of cells with signaling molecules or drugs, live cell microscopy, computerized cell tracking, on-chip staining of key proteins, and subsequent retrieval of cells for high-throughput gene expression analysis using microfluidic qPCR. Compared to traditional culture dish approaches, this pipeline improves experimental precision and throughput by orders of magnitude and introduces much desired new capabilities in cell and fluid handling, representing a major step forward in dynamic single-cell analysis. Combination of microfluidic membrane valves, automation, and a streamlined protocol now enables a single researcher to generate 1 million data points on single-cell protein localization within a week, under 48 predesigned experimental conditions selected from different signaling molecules or drugs, their doses, timings and combinations, and on various cell types and densities.

INTRODUCTION

Increasing spatial and temporal resolution of the imaging of dynamic cellular processes[1], such as protein translocation,[2, 3] interaction[4], post-translational modification[4], diffusion[5] and local concentration[6], and the transcription of single mRNA molecules[7-9] and organelle function[10, 11], has opened the door to many new biological questions.[12] Single-cell longitudinal imaging is the gold standard in cell and systems biology, due to the ability of this technique to capture dynamics and variability of individual cells. Live cell imaging and single-cell analysis of dynamic signal processing have greatly enhanced our

understanding of basic immune responses[13], development[14], biological noise[15], and drug responses[16]. However, experiments to measure single-cell dynamics using manual pipetting and conventional (dish or flask-based) cell culture methods have limited throughput, reproducibility, and confer researchers only a partial ability to manipulate the cellular environment precisely in real-time. Furthermore, the large media volumes around the cells contribute to background fluorescence, inhomogeneity in concentration due to convective mixing, and weakened cell-to-cell paracrine signaling due to dilution of secreted molecules.

Microfluidics overcomes difficulties in traditional live imaging by miniaturizing fluid control to size scales matching those of single cells[17]. Microfluidic cell culture enables precise and automated specimen manipulation during live cell experiments in nanoliter volume chambers that allow physiological diffusive signaling between cells. Multiple patterns of complex temporal stimuli can be delivered in parallel to culture microchambers in a single experiment, resulting in dramatic increases in throughput, particularly when combined with automated image analysis routines. Transient, increasing or decreasing stimuli, as well as rapid pulse trains of chemicals, can be seamlessly delivered to cells when membrane-valve-based microfluidic systems are used. Moreover, precise spatial manipulation is possible through pairing with technologies such as optogenetics[18, 19] or optical tweezers[20]. Finally, use of microfluidics facilitates closed-loop control with continuous experimental manipulation based on real-time imaging feedback[21]. When combined with a robust image analysis pipeline, a single researcher can generate and analyze rich multiparameter datasets on the timescale of weeks rather than years.

Previously, we developed an automated microfluidic cell culture system[22] and used it to study immune signaling dynamics[2], cell migration[23] and stem cell differentiation[22], all the while accounting for natural variability between individual cells. Precision fluidic control and high-throughput achieved by this system enabled us to discover digital, all-or-none activation of the NF-κB immune pathway following inflammatory signaling inputs[2], and made possible the development of a widely applicable computational model of this pathway[2] and of coordinated cell migration in a population context.[23] Here, we describe an accessible end-to-end pipeline for microfluidics-based single-cell analysis, spanning production of microfluidics chips, hardware and software setup for controlling and automating chip operation, parallelized single-cell dynamic imaging experiments, automated image and data analysis, and cell retrieval from the chip for gene expression analysis using the Fluidigm® BioMark™ microfluidics-based qPCR system[17,18] (FIG 1).

APPLICATIONS OF THE PROTOCOL

Although this protocol focuses on cell signaling applications, the method described herein is useful for many applications involving dynamic monitoring of cells under variable stimulation type and timing, and is equally well suited to labeling studies in fixed cells across many experimental conditions or time points. In the field of stem cell biology, questions concerning how cell fate depends on the combination, concentration, and duration of soluble input signals are widely interesting and are among those that the present approach was designed to answer .[22] Stem cells have been maintained in the chip described herein for 2 weeks without signs of differentiation or loss of renewal potential[22] Due to the ability to program arbitrary stimulation procedures, complex and otherwise labor-intensive protocols for protein or RNA labeling can be programmed and performed unattended, for up to 96 experimental conditions. Moreover,

compared to widefield imaging in a 96-well plate, imaging in a microfluidic system with ~35-µm chamber height leads to vastly improved image signal-to-noise due to reduction in medium volume and background fluorescence.

COMPARISON WITH OTHER APPROACHES

A number of microfluidic technologies have been described for cell culture applications, including automated antibody labeling for measuring signal transduction across multiple time points in fixed cells[24-26], study of single-cell dynamics under microfluidic gradients[27], microfluidic perfusion of cell culture arrays[28], single-cell trap arrays[29, 30], and single- or few-cell isolation in microwells[31]. Overall, these methods lack the throughput capacity of the present protocol in terms of number of parallel experimental conditions that can be set up. The method described herein involves use of a chamber whose geometry allows natural diffusive signaling and physical contact between cells. Depending on the biological question being addressed, it may be suitable to choose an alternative chip design that, for example, traps and isolates single cells. The present protocol, including chip fabrication and computer control, surface treatment, cell loading and maintaining long-term viability, along with retrieval from chip for downstream analysis, is applicable to mammalian cell culture in other multilayer polydimethylsiloxane (PDMS) chip designs.

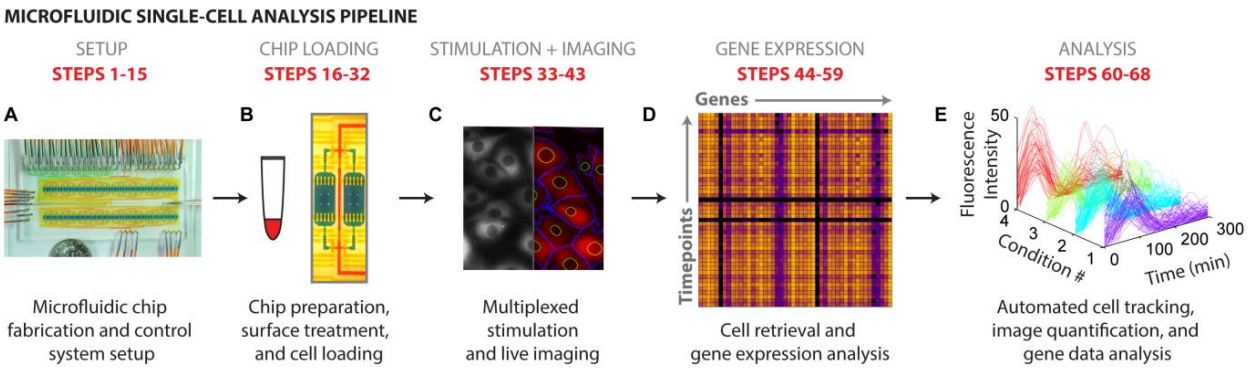

FIG 1. Single-cell live imaging and gene expression analysis pipeline. A) PDMS-based microfluidic chips are produced from silicon molds. The chip described (called the Cell Culture Chip[22]) contains 96 independent ~1 mm x 1 mm x 35 µm (35 nl) chambers. Computer-controlled hardware for actuating on-chip elastomeric valves is set up. B) Chips are mounted to the stage of a live imaging microscope and chambers surfaces are treated with cell adhesion molecules (typically fibronectin) to facilitate cell attachment. Cells prepared in suspension are loaded into each chamber and allowed to grow to desired confluency. Typically, 30% of chamber volume is exchanged with fresh medium at 2-h intervals to prompt rapid cell growth. C) Programmable chip control enables to deliver unique stimulation patterns for each chamber in parallel with live cell imaging. Imaging cells with fluorescent reporters facilitates readout of dynamic cell signaling events, such as translocation from the cytoplasm to the nucleus. D) After in-chip stimulation, cells are trypsinized, and they readily detach from chamber surface (typically in <1 min), and flowed through microbore tubing off-chip to a 96 well plate to be subjected to immediate lysis and one-step reverse transcription and specific-target amplification for gene expression analysis. Use of the Fluidigm microfluidic qPCR system enables to perform up to (96x96=) 9216 simultaneous qPCR

measurements. E) For live microscopy, image analysis automatically tracks cells and quantifies responses to produce single-cell trajectories of signaling dynamics. For images generated during microfluidic qPCR, fluorescence for each reaction over time is quantified to determine relative abundance of each gene template sequence. Images in (A) and (B) adapted with permission from REF [22]. Copyright 2013 American Chemical Society.

EXPERIMENTAL DESIGN

Microfluidic chip design. Multilayer soft lithography[32] enables the fabrication of microfluidic devices with integrated membrane valves that allow highly complex, parallelized fluid manipulation that have led to paradigm shifts in single-cell genomic[33, 34] and transcriptomic[35, 36] analysis. Chip fabrication begins with the design and preparation of molding masters on silicon wafers. The chip is typically designed using CAD software, and this design is printed to produce photomasks, which are, in turn, used to produce molds using standard UV photolithography in a cleanroom facility.[37, 38] In multilayer microfluidics, a positive photoresist is typically used to generate channels with rounded cross-section, and a negative photoresist is used to generate channels with rectangular cross-section.[39] For mold-making protocol steps see Gómez-Sjöberg *et al.*[22] The transparent, biocompatible, and gas-permeable PDMS is cured on the molds to create microscale features in the molds. By carefully aligning and bonding multiple PDMS layers on top of each other, it is possible to generate on-chip valves, and these valves can create a dense fluidic functionality that is analogous to the electronic functionality on a computer chip.[32]

The microfluidic cell culture chip[22] provides a broadly applicable platform that overcomes limitations of traditional live cell experiments around automation, precision, and throughput. The chip contains 96 individually controllable chambers of approximately 1x1 mm^2 surface area and 35 μm height, for a 35 nl volume. Each chamber can support the culture of between 1 and ~1000 mammalian cells depending on the cell size. Vials containing cell media and other reagents are connected to the chip through thin tubing. Up to 16 input reagent vials can be connected to the chip at a time. Flows from one or multiple inputs (which are combined by an on-chip mixer) are directed to selected chambers. An on-chip peristaltic pump enables highly precise delivery of predetermined volumes of reagents into chambers. The chip is constructed from two PDMS layers: the 'flow' layer, which contains cells and reagents, is positioned above a 'control' layer that creates microfluidic valves.[40] Overall, the chip functions as a miniaturized 96-well plate, where manipulation of nanoliter volumes for each chamber is independently controlled and fully automated.

Controlling and imaging the chip. Manufacture of on-chip valves that control chip functions requires hardware to deliver pressure to specified valves and software to implement different sequences of valve opening and closing. An air pressure source is connected to computer-controlled solenoid arrays that direct pressure to specified valves on the chip. Scripting in Matlab® or LabVIEW™ enables automation of chip functions, including chamber surface treatment, cell loading, cell feeding and stimulation, cell staining, cell retrieval from the chip, and chip cleaning. Input reagents, such as cell media, are pressurized with 5% CO_2 in air gas mixture to equilibrate the vial contents with the appropriate gas composition. The chip is mounted securely on the stage of an inverted automated fluorescence

microscope with environmental control to maintain temperature (37 °C), gas composition (5% CO_2 in air), and humidity (>95%) around the chip. Manufacturer-provided or open-source microscope control software such as μManager (www.micro-manager.org) is used to carry out timelapse imaging of cells in chambers on the chip. The chip can be used with either widefield or confocal microscopes. Although confocal compared to widefield systems may provide improved image quality, widefield systems have advantages in imaging speed and lower phototoxicity, which becomes important when studying signaling dynamics and fine time resolution needs to be maintained while acquiring images across many chip locations.

Maintaining cell viability in microfluidic chips. PDMS provides excellent permeability to oxygen and CO_2, which facilitates cell culture in closed PDMS devices.[41] As with any live imaging experiment, cell health is negatively affected by phototoxicity, and, therefore, illumination time and intensity should be minimized. Toxicity from uncrosslinked PDMS can be eliminated by fully curing PDMS chips, autoclaving them or using chemical extraction methods.[42] The small volume of microfluidic chambers means that cells rapidly consume nutrients and require feeding at frequent intervals. Cell feeding in the cell culture chip can be performed using the on-chip pump to gently exchange a portion of the chamber solution with fresh medium. A default 2-hour feeding interval with 30% medium replacement is suitable for cultures of 3T3 fibroblasts, RAW264.7 macrophages, and probably other cell types. As a consequence of the small chamber volume, the concentration of ligands introduced into the chambers decays exponentially as the ligands degrade and as cells process and internalize them. This concentration variation may be used to generate periodic input signals to cells. To achieve constant ligand concentration, the medium containing the ligand can be continually perfused using pressure-driven flow or the on-chip peristaltic pump. Please note that a no-ligand feeding condition should be included in stimulation experiments as a control to determine the possible influence of the feeding method on cell response.

Cell tracking and data analysis. Due to the volume of image data generated by the present protocol, automated processing and quantification is essential. Incorporating fluorescent reporters that label cellular compartments, such as the nucleus, can greatly aid computerized cell tracking and data extraction. Such labels may be genetically encoded in the cells' DNA or small molecule fluorophores may be added to cells before imaging. A number of software tools are available for image quantification. The Matlab Image Processing Toolbox provides a full set of functions for customized implementation of essentially any image analysis task. We use Matlab routines for analysis of dynamic NF-κB nuclear translocation and oscillation in cells.[2] Open source packages such as CellProfiler provide a broad range of image analysis functions that can be customized without programming. For large or complex image processing sets, it may be necessary to parallelize the tasks and carry out the analysis on a high-performance computer cluster. After cell tracking and image quantification, individual cell trajectories are assessed (typically in Matlab or Excel) to draw conclusions about single-cell and population responses to each input condition.

LIMITATIONS

Microfluidic cell culture experiments are inherently more complex and require longer setup times than experiments conducted with traditional methods, though the labor and time investment is recovered many fold by gains in throughput, automation, reproducibility, and image quality. However, the biggest payoff is in experiments that deliver very high information density (large number of data points per chamber or per cell, collected over the course of the culture). Simple experiments with a single end-point readout might not be suited to the microfluidic platform. The chip design described here is such that the chip has limited ability to generate chemical gradients, and it also requires for media to flow over cells to deliver new stimuli, a process that disturbs the paracrine signaling field in the chamber. Other chip designs enable gradient formation and diffusive feeding, which preserves the paracrine field[27, 43]. The chip design described in the present protocol is not optimized for generating smoothly varying (i.e. sinusoidal) inputs to cells. Gene expression analysis is currently limited to analysis of all cells within a chamber rather than single cells, though isolation and analysis of a cell of interest may be achieved in the current chip design using optical trapping methods.[44]

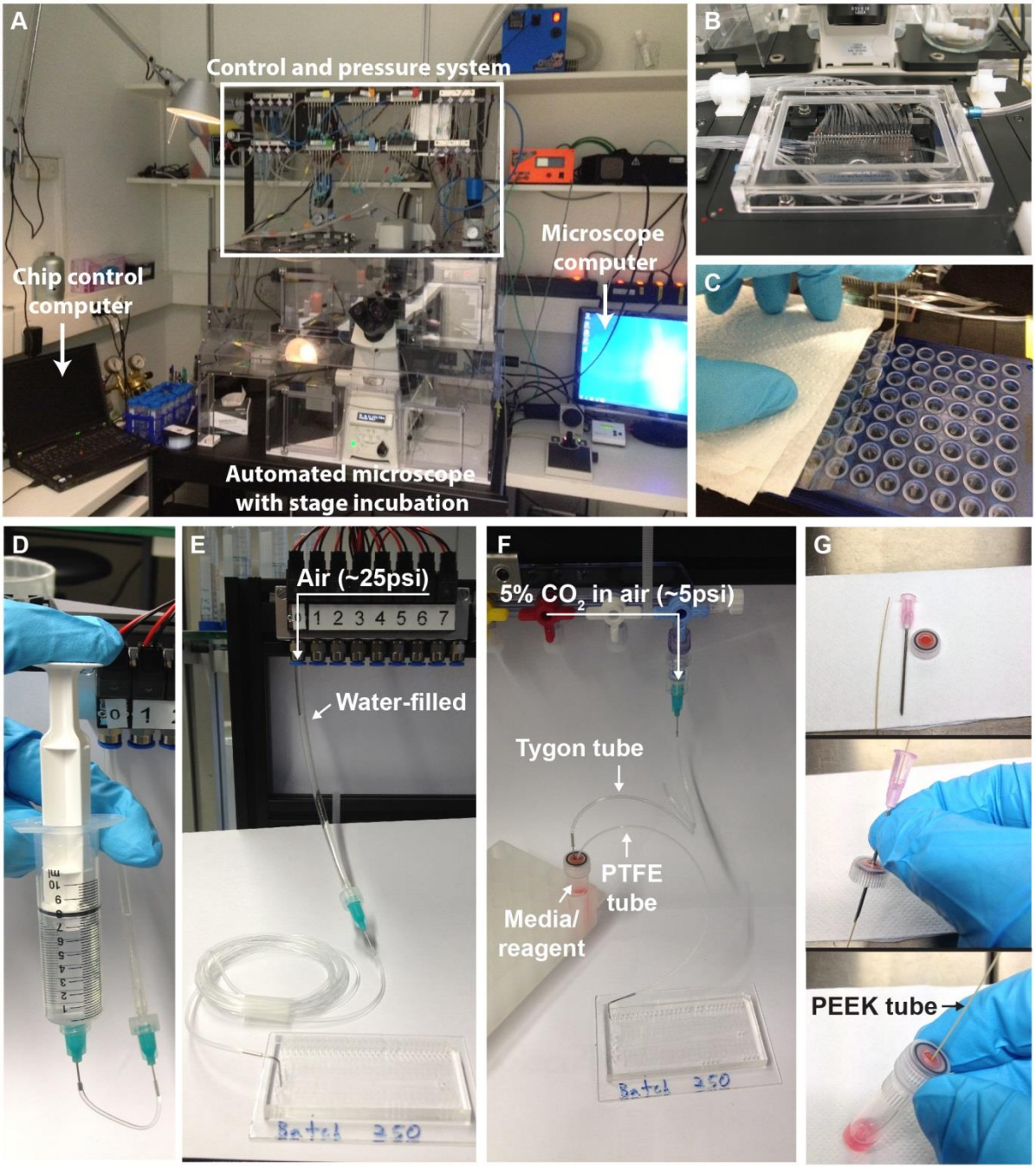

FIG 2. Photos of microfluidic cell culture system setup. (A) System overview. Solenoid valves that pressurize on-chip valves are controlled by a USB controller box operated by a laptop computer. An air pressure source is connected to solenoid valves (required pressure ~20–30 psi). The valve control system and computer are portable for use on different microscopes. A separate computer controls a fully motorized inverted fluorescence microscope (pictured: Nikon Ti-Eclipse). The microscope contains an incubation system to control temperature, humidity, and CO_2. (B) The chip is secured tightly to the microscope stage using a stage plate with a viewing area sufficiently large to see chambers and surrounding fluidic circuitry on chip. Slots in stage cover allow tubing connections to the chip, and tubing is secured using plastic stage clips. (C) Cell retrieval from chip. A ~10-cm length section of PEEK tubing is connected to either the upper or lower waste outlet on

the chip. Trypsin is delivered to chambers and cells are washed out serially through the tubing. Between each chamber, a PBS wash step prevents cross-contamination between chambers. The cells are deposited into a 96-well plate containing 5 µl of lysis buffer for qPCR processing. Each well should be sealed to prevent evaporation during cell retrieval. D) A syringe can be used to fill control lines with water. E) Control lines connect the chip to a computer-controlled pneumatic valve manifold supplied with air at typically 20–30 psi. Tygon tubing of sufficient length to reach the chip on the microscope then connects to the corresponding valve on the chip. F) To connect pressurized reagent inputs to the chip, Tygon tube connects a port on a manual manifold to a vial containing the desired reagent or medium. The connection from the vial to the chip is made using PTFE tubing. (G) Process for making vials to be pressurized for flowing reagents or cells into chip. While for media and reagents PTFE tube is used, for loading cells PEEK tube is used. A 20-gauge needle is inserted through a rubber membrane screw cap and 0.02" PEEK tubing is inserted through the needle. The needle is then removed.

MATERIALS

REAGENTS

- Polydimethylsiloxane (PDMS) and curing agent (Momentive RTV-615A and RTV-615B)
- Trimethylchlorosilane (TMCS) (Sigma 92360) !CAUTION TMCS is highly toxic and should be handled only in a fume hood, with proper personal protective equipment.
- Pluronic F-127 (Sigma P6867)
- Fibronectin from human plasma (Millipore® 341635-1MG)
- Cells and media. Cells should be adherent or semi-adherent on fibronectin or other ECM protein. Cells used here are NIH3T3 mouse fibroblasts and RAW264.7 mouse macrophages genetically modified to express NF-κB (p65) fluorescent fusion proteins.[2, 45]
- Signaling molecules for cell stimulation. Our lab has used TNF (Life Technologies PMC3014) and LPS (Sigma L4525).
- Hydrogen peroxide (H_2O_2) 30% (vol/vol) (Sigma 95313-1L) !CAUTION H_2O_2 is corrosive; wear proper personal protective equipment.
- CellsDirect one-step qRT-PCR kit containing Resupension Buffer, Lysis Enhancer, and SuperScript III/Platinum Taq mix (Life Technologies 11753-100)
- Assay loading reagent (Fluidigm 85000736)
- Sample loading reagent (Fluidigm 85000735)
- TaqMan® gene expression assays (Applied Biosystems® 4331182)
- TaqMan universal PCR master mix (Applied Biosystems 4304437)
- TE buffer (Ambion® AM9849)
- TaqMan primers (Applied Biosystems)
- Double-distilled water (ddH_2O)
- Delbucco's Phosphate Buffered Saline (PBS, Life Technologies 14190250)
- Delbucco's Modified Eagle Medium (DMEM, Life Technologies 32430-027)
- Fetal Bovine Serum (FBS, Sigma F2442-500ML)

- 0.05% Trypsin-EDTA (1X) (Trypsin, Life Technologies 25300-054)

Reagent setup

- 6% H_2O_2 solution (0.5 L): add 100ml 30% H_2O_2 into 400 ml ddH_2O. Store at 4 °C. Stable for 1 month.
- Medium for 3T3 fibroblasts and RAW264.7 macrophages (DMEM + 10% FBS): add 50 ml FBS to 450 ml DMEM. Store at 4 °C. Stable for 1 month.
- 100 µg/ml fibronection solution (1ml): add 100µl fibronectin (1mg/ml) into 900 µl PBS. Use immediately.
- 0.2% pluronic solution: Add 0.1g pluronic powder into 50 ml PBS. Store at at 4 °C. Stable for 6 months.
- Lysis Buffer solution (300 µl): Thaw Resuspension Buffer on ice. Combine 250 µl Resuspension Buffer and 25 µl Lysis Enhancer. Store on ice until ready to use.

EQUIPMENT

- Automated fluorescence inverted microscope with environmental control chamber. We have implemented this protocol on Leica DMI6000B and Nikon Ti-E microscopes.
- Pneumatic solenoid valves and controller boxes. Parts and assembly instructions are available at http://www.microfluidics.ethz.ch/chip_culture_protocol
- Silicon master molds. The silicon cell culture chip molds were obtained from the Stanford Microfluidics Foundry, http://www.stanford.edu/group/foundry/
- BioMark™ HD system with IFC Controller MX (Fluidigm)
- 48.48 Dynamic Array™ IFC (Fluidigm)
- Sonicator (SonoSwiss, SW 6H)
- Plasma machine (Diener, FEMTO Version A)
- Spin coater (SPS-Europe, SPIN150-NPP)
- Vacuum pump (Varian, SH-110) and desiccator (Thermo Scientific Nalgene, EW-06520-05)
- Punching press and 20-gauge round hole punch (Syneo, Accu-Punch MP)
- Laboratory oven (Thermo, Heratherm OSM60)
- Laminar flow hood (Thermo, Herasafe KS)
- Orbital mixer and 100ml disposable cups (Thinky Corp, ARE-310 and 250-100DSP)
- Pre-cleaned glass slides 75 x 50 mm (Fisher, #W56948)
- Stainless steel microbore tubes 0.025” OD x 0.013” ID x 0.75” long (New England Small Tube)
- Luer manifolds 5-port (Cole Palmer, #EW-30600-43)
- Disposable stainless steel dispensing needles (23 gauge, 0.5" long, type 304, ID 0.017", OD 0.025”, McMaster-Carr)
- Pressure regulator 0-30psi (Airtrol R-800-30-W/K)

- PEEK™ tubing (510 µm OD x 65 µm ID, IDEX 1543)
- PTFE tubing (0.022" ID x 0.042" OD, Cole Parmer EW-06417-21)
- Tygon® microbore tubing (0.02" x OD 0.06", VWR S-54-HL)
- Microtubes 2ml (Sarstedt 72.694.006)
- Membrane Screw Caps (Sarstedt AG 65.3716)
- 10 ml syringe (BD Medical 14-826-13)
- 0.2-µm syringe filter (Thermo Fisher Nalgene 191-2020)
- Scotch tape
- 5% CO_2 pressure source
- Compressed air source
- 'Valve control computer' with Windows (Microsoft) and MATLAB (Mathworks, version 2006 or later) installation. A laptop computer allows the valve control system to be portable between different microscopes.
- 'Analysis computer' with Windows (Microsoft) and the following software: CellProfiler open source package (www.cellprofiler.org) for image analysis, and MATLAB (Mathworks, version 2006 or later) and Fluidigm Real-Time PCR Analysis software (Fluidigm) for qPCR data analysis.

Equipment setup

Obtain flow and control layer cell culture chip molds based on the AutoCad DXF chip design file (Supplementary Data) using one of several organization that provide microfluidic fabrication services, such as: Trianja (http://www.trianja.com), SIMTech Microfluidics Foundry (http://www.simtech.a-star.edu.sg/smf), , or FlowJEM (http://www.flowjem.com). Additionally, the Stanford Microfluidics Foundry provides a summer school for microfabrication techniques (http://stanford.edu/group/foundry).

The cell culture chip contains on-chip elastomeric valves that are actuated by an external pressure source. Gómez-Sjöberg, *et al.*[22] developed a setup that uses 3-way solenoid valves that are computer-controlled by a custom USB interface. This control system can be used generally for multilayer PDMS chips. Detailed instructions for constructing the control system and the related software and drivers are available at http://www.microfluidics.ethz.ch/chip_culture_protocol.

Prepare 'valve control computer' and 'analysis computer' with software listed in the Equipment list.

PROCEDURE

Chip fabrication from existing molds TIMING 36 h

1| Place flow and control mold wafers inside a closed wafer carrier box with a small beaker containing a few drops of TMCS. Incubate for 60 min and use wafers within 1 h following the incubation.

2| Make an aluminum foil container by molding foil around a 110-mm diameter Petri dish. To make the flow layer, weigh 38 g of PDMS in a 100ml disposable cup and add curing agent at a 1:10 weight-to-weight ratio (curing agent:PDMS, 3.8 g) for each mold. Mix in an orbital mixer for 3 min at 2000 RPM and de-foam for 5 min at 2200 RPM. Pour 40 g of the resulting PDMS over wafer.

3| De-gas the PDMS flow layer by placing the aluminum foil container in a larger Petri dish in a vacuum desiccator. Make sure that the PDMS does not overflow and that inrushing air does not tip the wafer when refilling the desiccator with air.

4| To cure the PDMS flow layer, cover and bake for 1 h at 80 °C. Make sure the substrate is leveled.

5| To make the control layer, in a 100ml disposable cup first weigh 22 g PDMS and add curing agent at 1:10 ratio (2.2g) for each mold. Mix in an orbital mixer for 3 min at 2000 RPM and de-foam for 5 min at 2200 RPM. Place the cup containing mixed PDMS in a vacuum desiccator until all air bubbles have been removed (~20min). Pour PDMS over a wafer covering three quarters of substrate and, using a spin coater, spin the control mold wafer for 12 s at 500RPM, then for 1 min at 2500 RPM to achieve a control layer thickness of approximately 30 μm. To cure the control layer, cover and bake on a level surface for 1 h at 80 °C.

6| To coat glass slides with a thin PDMS layer, first clean 50x75-mm glass slides by 45 min sonication in ddH_2O. After sonication, dry the slides at 80 °C for ~45min. Weigh and mix 1:10 PDMS (38g PDMS, 3.8g curing agent) as in step 2. Using spin coater, spin 1:10 PDMS onto 50x75 mm slides for 15 s at 500 RPM then 60 s at 2500 RPM. Bake at 80 °C for 1.5 h to cure the PDMS.

7| Remove PDMS from the flow layer by cutting out around channels and peel PDMS carefully off the wafer. Align and punch the indicated holes using a 20-gauge round hole punch. Capture all punched plugs on tape. Clean the flow layer after punching by coating with tape and pressing tape into the mold.

8| Plasma treat the control wafer and cut-out PDMS flow layer for 15 s at 45 W using the plasma machine. Position flow layer cut-outs above control layer (still on mold) under low magnification. Make alignment marks on the two layers coincident, and bring the layers together. Irreversibly bond flow to control layer by baking for 2 h at 80 °C.

9| Cut out chip from around the channels and carefully peel them off the control wafer. Punch the remaining control layer holes. Clean and plasma treat (15 s at 45 W) surfaces of the PDMS-coated slide and control-flow assembly. Position the chip on a PDMS-coated slide and bake at 80 °C for minimum 36 h before use. This final bake is essential to minimize the amount of un-crosslinked polymers remaining in the PDMS. After the chip making procedure is mastered, rate of chip failure due to manufacturing defect is <10%.

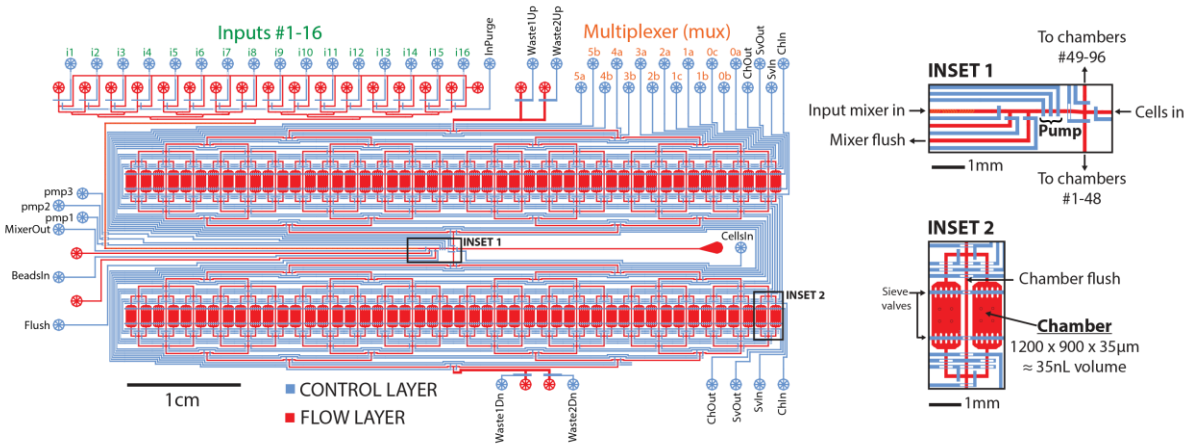

FIG 3. Cell culture chip layout. The chip contains 96 individually addressable chambers and can be connected to up to 16 input reagent vessels . Cells, media, and reagents are contained in the red "flow" layer, whereas membrane valves are created by the blue "control" layer. The multiplexer (mux) valves control which chamber or chambers are selected. Cells can be loaded into chambers using the CellsIn port. Cell and reagent input vials are pressurized with 5% CO2 to 3–10 psi (200–700 mbar) and delivered to the chip through microbore tubing by pressure-driven flow. Input lines converge and pass through a herringbone mixer, enabling the researcher to select reagents one at a time or to mix multiple reagents before they enter chambers. PBS connected to the InPurge line clears the input manifold and mixer when selecting a new input, and the waste flows out through the mixer flush outlet. Inset 1 shows an on-chip peristaltic pump that can generate precisely metered flow to chambers, which enables replacement of a specific fraction of the chamber volume. Pumping precision (1 pump cycle) is ~0.35 nl. Inset 2 shows an enlarged view of the microfluidic chambers, which are ~1 mm2 in area and 35 µm in height for a ~35 nl volume. Typically 100–200 large (i.e. 3T3 fibroblast) or 200–300 small (i.e. RAW264.7 macrophages) cells are grown in a chamber. Sieve valves at the entrance and exit of each chamber enable to trap large cells and particles (>20 µm diameter). A chamber flush line enables to clear the flow path before directing new reagent to chambers.

Setting up the chip control system TIMING 1 day

10| Assemble a 48-valve control system (six manifolds with eight pneumatic solenoid valves each, operated by two-valve controller boxes) connected to a pressurized air source, and install USB driver software (see Equipment setup).

11| Mount pneumatic solenoid valve assembly and control boxes near the microscope. Please note that use of a portable mounting frame is convenient for transporting the control system between multiple microscopes (see FIG 3A for example mounting frame). Make sure that water-filled Tygon microbore tubing from each pneumatic valve connect to the chip on the microscope stage and actuate control lines on the chip (FIG 3E).

12| On the mounting frame, additionally attach four 5-port Luer manifolds end-to-end connected to a pressurized 5% CO_2 source through a 0–30-psi pressure regulator. Attach Tygon microbore tubing to each manifold port of sufficient length to reach vials containing reagents for input into the chip. This tubing is used to pressurize the reagents for injection into the chip (FIG 2F).

13| Set up cell culture chip graphical user interface (GUI) software (available at web link reported in the Equipment setup).

14| (OPTIONAL) It is good practice to clean the control line tubing for every new chip. For this purpose, use a syringe or pressurized reservoir to fill each control line with 6% H_2O_2. Elevate tube ends to prevent them from being drained by gravity. Incubate H_2O_2 in the control lines for 1 h.

15| Place tube ends in a container and elevate pressure within the system to expel H_2O_2. Rinse each tube with ddH_2O.

Chip preparation on a microscope TIMING 1–2 h

16| Clean residual PDMS from the bottom of the microscope slide using a razor blade. Apply scotch tape to the glass surface to remove residual PDMS and dust particles. Inspect the chip under low magnification periodically until the bottom surface is visually free of dust or PDMS.

17| Position chip on microscope stage so that all chambers of chip are visible. Tighten stage screws to secure position (FIG 2B).

18| Using a syringe or a pressurized reservoir, fill each control line tube with ddH_2O (FIG 3D).

19| Connect control line tubes to the chip (FIG 2E and FIG 3).

20| Turn control line pressure to 0. Push "Close All" button on GUI (FIG 4). Gradually increase control line pressure to 25 psi (1.72 bar). Inspect the chip to ensure there is no delamination leading to leakage outside chip or between control and flow layers.
?TROUBLESHOOTING

21| Test that control lines are connected correctly by closing valves in the GUI software and ensuring that the appropriate valve is closed on the chip by inspection under low magnification.

22| Connect waste vials to Waste1Up and Waste1Dn flow outlets on the chip (FIG 3).

23| Secure tubes so that stage movement does not apply force on the chip (FIG 2B).

Chip surface treatments TIMING 6 h–overnight

24| To promote cell adhesion, chamber surfaces can be treated with proteins including fibronectin, collagen, and gelatin. In our tests with mouse 3T3 fibroblast and RAW macrophage cell lines, fibronectin provides rapid and reliable cell attachment.

25| Prepare four input vials (FIG 2G) containing 1 ml of pluronic (0.2% wt/vol in PBS), 1 ml of fibronectin (100 μ g/ml), 1 ml of medium, and 1 ml of PBS, respectively. Set inlet pressure to 7 psi (480 mBar).

26| Connect pluronic and fibronectin vials to input #1 and #2 on chip, medium to input #3, and PBS to InPurge flow inlets (FIG 3).

27| Flush air from tubes by opening inlet valves for pluronic, fibronectin, medium, and PBS, one at a time and directing flow through Input Flush (FIG 3) until air has been eliminated from flow path for each input.

28| Remove air from the chip: First, close all chip outlets (Waste1Up, Waste2Up, Waste1Dn, and Waste2Dn). Second, open multiplexer and chamber valves.

29| Remove any stray air bubbles by applying flow pressure to a closed channel to force air out through the PDMS matrix.

30| To block non-chamber surfaces with pluronic to prevent cell attachment in these areas: first, close all valves that allow flow to chambers by selecting "All Chambers" in the chamber dropdown box and activating "Flush" and "Ch In Closed" checkboxes in the software GUI (FIG 3). Second, close all flow outlets on chip by ensuring Waste1Up, Waste2Up, Waste1Dn, and Waste2Dn are all closed. Finally, open input #1 (pluronic), MixerOut, and Pump to allow pluronic flow into the non-chamber areas of the chip. As pluronic flows in, air in the non-chamber areas of the chip is pushed out through the PDMS. After all air has been removed from the chip (~15 min), continue incubation with pluronic for 1 h.

31| Wash away pluronic from chip using PBS: first, close input #1 (pluronic) and open InPurge (PBS). Open Waste1Up and Waste1Dn to allow PBS to flow through the chip. Continue to allow PBS flow across all non-chamber surfaces for 30 min. CRITICAL STEP: Pluronic must be completely washed from chip. Residual pluronic may enter chambers and prevent cell adhesion.

32| Treat chamber surfaces with fibronectin: close InPurge (PBS) inlet and open Input #2 (fibronectin). Allow fibronectin to flow through the non-chamber areas of the chip, displacing the PBS, for 10 min. Finally, open valves to allow flow to chambers by using GUI to open ChIn, ChOut, and de-selecting "Flush" and "Ch In Closed" in the Multiplexer panel. Again close exits from chip (Waste1Up and Waste1Dn). Now fibronectin will flow into chambers, displacing the air in the chambers. Incubate fibronectin in the chambers for between 2 h and overnight.

Preparing cell suspension and loading cells into chip TIMING 2–4 h

33| Prepare a single-cell suspension of cells with concentration $5x10^5$–$2x10^6$ cells/ml. The typical volume consumed during cell loading into 96 chambers is 25–50 µl. Preparing suspensions toward the high end of the concentration range specified above enables faster loading due to fewer seeding rounds . Use of microbore PEEK tubing helps to prevent clumping of cells during loading. Connect the vial to the cell input channel on the chip and pressurize with 5% CO_2 at 3 to 5 psi.

?TROUBLESHOOTING

34| Load cells into chambers automatically (option A) or manually (option B). Please note that either option is essentially equivalent.

A. Automated cell loading using scripting

i. Using a cell suspension at $5x10^5$ cells/ml, force cells to flow into each chamber and immediately acquire a 10x phase image of the chamber. Cells will appear as circular bright spots in the image, which can be detected by applying an intensity threshold to the image.

ii. Count and record the number of detected cells loaded in each chamber. Cells begin adhering to the fibronectin surface within minutes.

iii. After completing one round of seeding, wait 5 min, and repeat steps Ai and Aii above. Cells from the previous seeding round remain attached as additional cells are loaded. Acquire a second image and update the cell count for each chamber.

iv. Repeat steps Ai and Aii automated seeding until the cell count for each chamber reaches a specified target (such as 150 fibroblasts or 200 macrophages). The target number of cells per chamber is chosen based on the cell size and growth rate to achieve ~80% confluence during the experiment.?TROUBLESHOOTING

B. Manual cell loading

i. Perform a similar procedure as for option A above but using visual estimation of cell count in each chamber.

ii. Manually force cells to flow to each chamber in turn.

iii. After one seeding round, evaluate which chambers require additional cells and seed additional cells in the chamber after a few minutes have elapsed to allow cell adherence.

?TROUBLESHOOTING

Imaging and feeding cells TIMING 4 Set up time-lapse imaging in the microscope control software: store stage positions for each imaging location and/or chamber of interest. Specify a desired time lapse between images to be acquired in sequence. For imaging cell growth, typically a 30-min interval between image acquisitions is sufficient. 10x magnification phase imaging is sufficient to monitor cell growth in the chip.

36| Feed cells in the chip at predefined intervals as detailed below. Please note that the following numbers have been satisfactory for a variety of cell types, but it might be necessary to perform experiments to determine the optimal feeding volume and frequency required by different cell types. For one feeding round, use on-chip pump to exchange 30% of the volume in each chamber containing cells. One pump cycle replaces approximately 1% of chamber volume. Therefore, to replace 30% of chamber volume, operate the pump for 30 cycles. The pump is composed of three microfluidic valves in series. The following valve control sequence performs one pump cycle: [0 0 1] – [1 0 1] – [1 0 0] – [1 1 0] – [1 1 1], where 0 indicates the valve is open (depressurized) and 1 indicates the valve is closed (pressurized). The time delay between each valve operation determines the flow rate. Maximum pump speed is limited by the response time of the pneumatic solenoid valves and driving electronics. We typically operate in the range of 0.1–0.05-s delay between pump valve operations, for flow rates 30–60 nl/min.

37| Repeat the feeding procedure detailed in step 36 every 2 h. The feeding interval can be adjusted to 1 h for dense cultures or every 3 h for sparse cultures. In our experience with 3T3 fibroblasts and RAW264.7 macrophages, 2-h feeding intervals with 30% chamber replacement generates

optimal cell growth. Occasionally (perhaps 5% of experiments), debris may enter the chip, which block the flow.

?TROUBLESHOOTING

38| Acquire phase contrast images at the previously specified locations during feeding to monitor cell health. Hardware focus technologies (such as Perfect Focus System, Nikon) help to maintain focus at many locations across the large chip surface.

?TROUBLESHOOTING

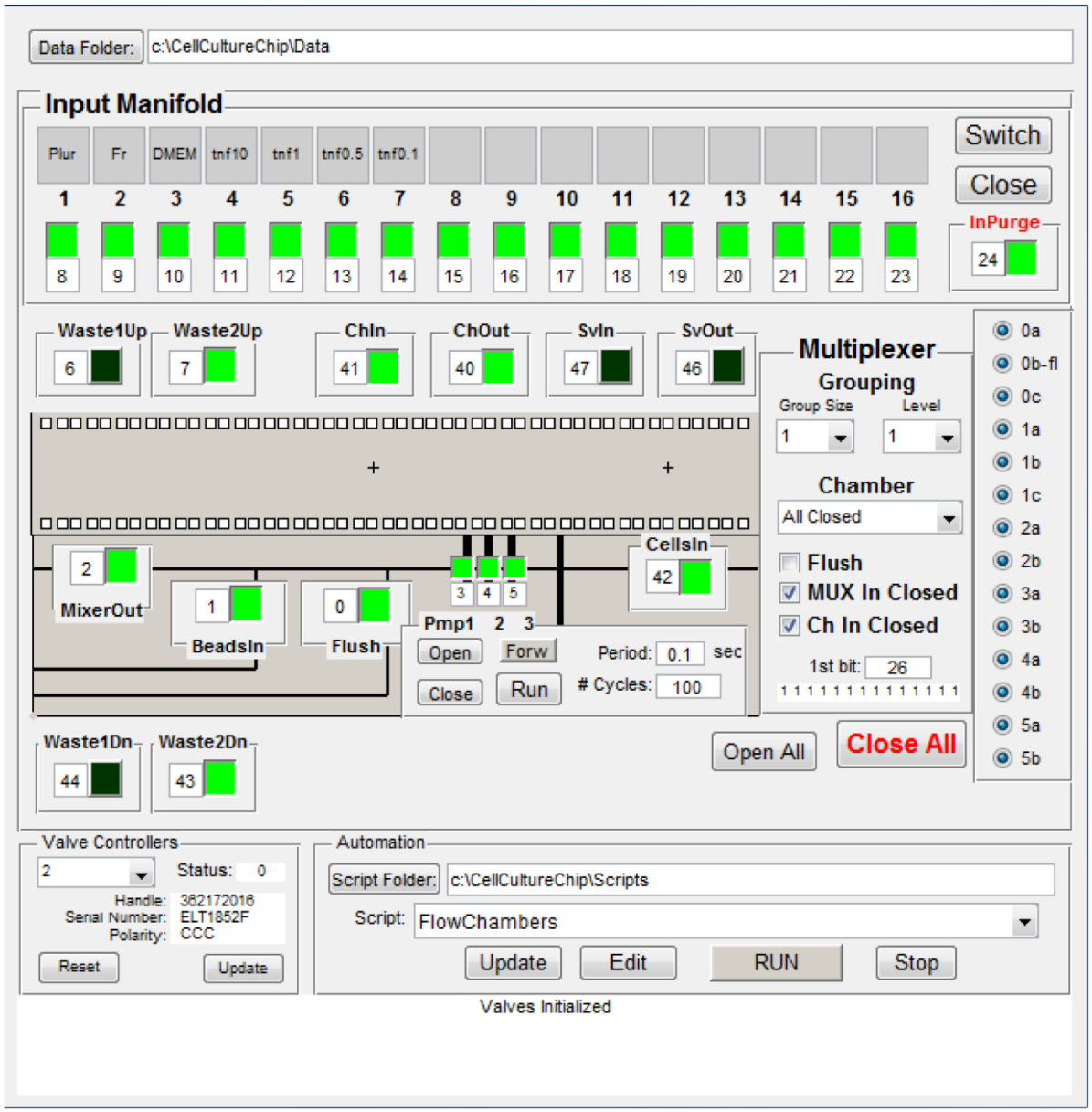

FIG. 4. Cell culture chip control graphical user interface. The software enables the researcher to perform the manual actuation of on-chip valves and confers the ability to run automated scripts to carry out sequential valve operations that implement cell culture and stimulation functions.

Conducting a cell stimulation experiment TIMING variable 2 h to 2 weeks

39| Prepare in vials solutions of the experimental input reagents at desired concentrations, such as cytokines at different dilutions in media. For example, TNF dilutions may span from 0.01 to 100ng/ml to test the NF-κB dose response. To test the role of stimulus timing, researchers may deliver pulses having varied duration or frequency. Inputs may be combined using the on-chip mixer. Use PTFE tubing to connect input vials to the chip.

40| Connect inputs to chip, pressurize with 5% CO_2 at 7 psi, and prime each input directing flow through flush output on the chip until air in the tubing and channel is replaced by fluid from the vial.

41| Program cell stimulation for each chamber: for each input time, record the chambers receiving the input, the mode of input (pumping to replace a fraction of chamber volume or pressure-driven flow to fully replace volume), and which inputs to select. For example, for 10-min tumor necrosis factor (TNF) input pulses spaced at 1-h intervals, at times 0 min and 60 min chambers would receive TNF, whereas at 10 min and 70 min the would receive the cell medium.

CRITICAL STEP: Log the timing of each stimulus delivery, as well as times of image acquisitions, so that image data can be properly aligned with stimulation timing.

42| Fine tune imaging positions and focus using microscope software before starting experiment. Specify imaging settings for fluorescence acquisition: for imaging nuclear-cytoplasm shuttling dynamics, we acquire GFP and dsRed channels using a 20x long-distance objective. Perform at least one round of imaging before starting the experiment, then start stimulation script to begin experiment. Perform imaging and chip operations as independent processes. Continue imaging as in-chip stimulation experiment proceeds.

43| Wait for completion of the experiment.

44| After the stimulation experiment is complete, cells may be fixed and stained for to relate dynamic signaling response to additional protein endpoint measurements. Alternatively, live cells may be harvested from chip for gene expression analyses.

Retrieving cells from chip for gene expression analysis TIMING 1 h

45| Prepare a 96-well plate in which 5 µl of lysis buffer solution (Reagent setup) is added to one well for each chamber of cells to be retrieved from the chip. For example, an experiment to measure gene expression at 30-min intervals over 24 h uses half the plate (48 chambers, one per time point).

46| Connect a vial containing 1 ml trypsin to chip input.

47| Use a length of 10 cm of 0.02" OD PEEK tubing to connect the chip output to the waste (FIG 3C).

48| Deliver trypsin to each chamber containing cells. Allow 1–3 min for cell detachment. Please note that efficiency of cell retrieval by this method is typically ~90%.

49| For each chamber containing detached cells for collection: Position unconnected end of PEEK tubing into a well containing lysis buffer on 96-well plate; force 1–3 µl of cell medium to flow

through each chamber containing detached cells and collect the outflow through PEEK tubing into 96-well plate containing 5 µl of lysis buffer (FIG 3C); flush 3 µl of PBS through the tubing to clear them for the contents of the next chamber (collect outflow on Kimwipe).
?TROUBLESHOOTING

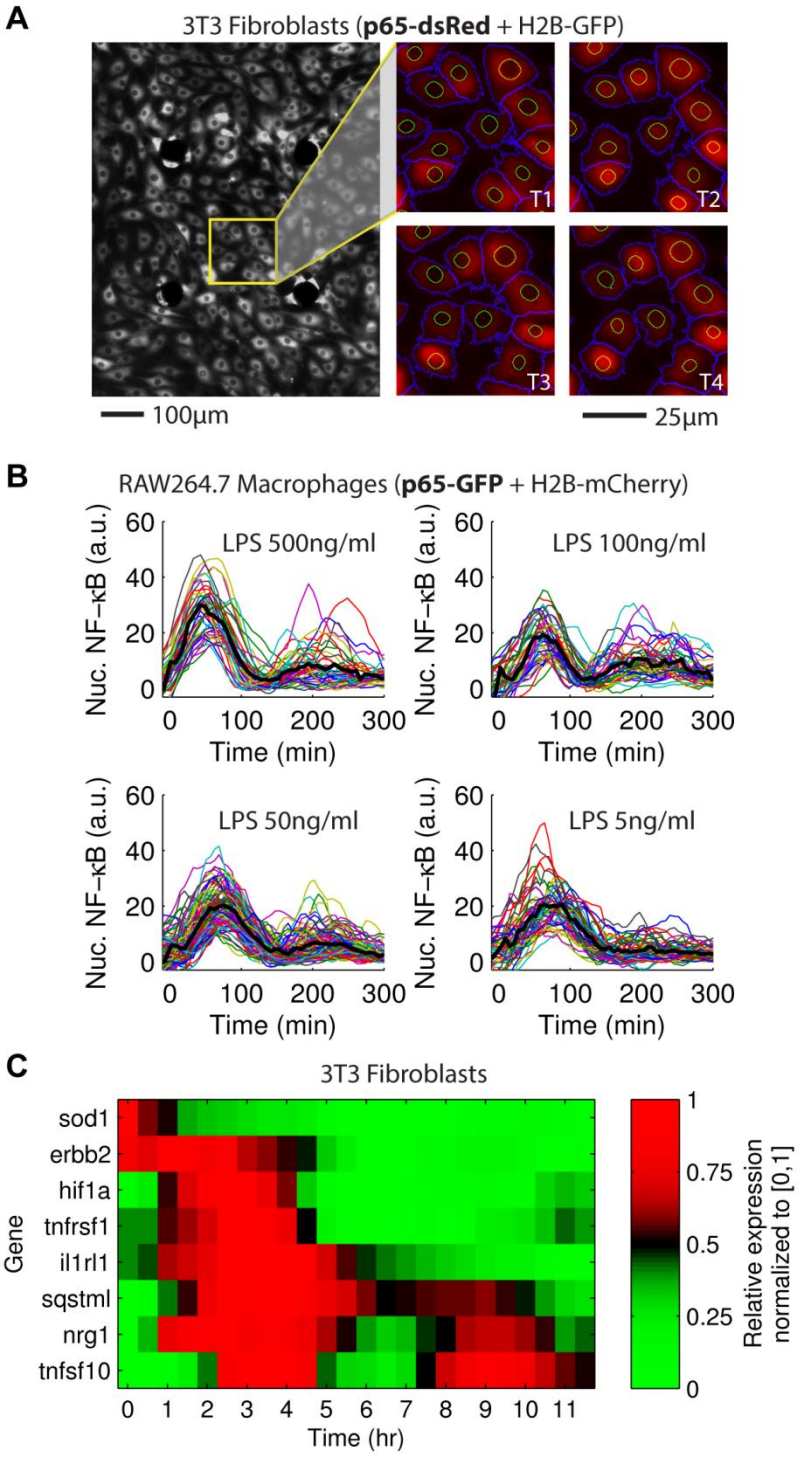

FIG 5. Anticipated results. (A) Live fluorescence imaging of 3T3 fibroblast cells under TNF stimulation expressing p65-dsRed and H2B-GFP fusion proteins and automated image analysis. The left grayscale image is composed of two stitched vertical adjacent images in the chamber and shows p65-dsRed fluorescence. The four dark spots arranged in a rectangular pattern are PDMS pillars included in the chip design to prevent chamber collapse. In the right panel of four images, red fluorescence is due to p65-dsRed, nuclear outline (yellow) is determined from H2B-GFP image

(not shown), and cytoplasmic outline (blue) is determined from the p65-dsRed image. To quantify NF-κB activation over time, nuclear p65-dsRed fluorescence intensity is measured relative to cytoplasmic p65-dsRed fluorescence intensity. Images corresponding to four consecutive time points are shown (T1–T4). (B) Single-cell responses to step changes in lipopolysaccharides (LPS) concentration in RAW264.7 macrophages. Panels correspond to cells in different chambers on the chip given the indicated LPS dose at time T=0. The Y axis shows mean nuclear intensity of NF-κB (p65) fluorescence. Colored lines indicate different cells. (C) Expression of eight genes at 30 min time points after on-chip stimulation of a population of a few hundred cells with TNF. Two chambers comprised each of the 24 time points, using a total of 48 chambers on the chip. Values are relative expression ($2^{Ct\_gapdh - Ct\_gene}$) are normalized to a value from 0 to 1 to facilitate heatmap display to compare the temporal expression patterns of the different genes.

High-throughput qPCR using Fluidigm BioMark™ System TIMING 4 h

50| Thaw 2x CellsDirect reaction mix on ice as well as the 20x TaqMan™ gene expression assays (18 µM TaqMan™ primer pairs) of interest. For studies of inflammatory signaling, relevant assays might include NF-κB regulated genes

CRITICAL STEP: Make sure that thawing of the 2x CellsDirect reaction mix is complete and mix thoroughly this reagent before use.

51| Prepare in a 1.5-ml tube a primer pool containing each TaqMan™ assay (initial concentration 20x) diluted 100 times in TE buffer to a final concentration of 0.2x. In this example, if the final volume of the assay mix is 150 µl and there are 48 TaqMan™ genes, add 1.5 µl of each TaqMan™ assay and complete with 78 µl of TE buffer.

52| Prepare in a 1.5-ml rube a reaction mix having the following components:

Component	Volume to add per reaction (µl)	Final concentration
2× CellsDirect reaction mix	5	1×
TE buffer	1.5	
Primer pool (0.2x or 180 nM)	2.5	45 nM
SuperScript III/Platinum Taq mix (from CellsDirect kit)	1	

53| Distribute the 10 µl of the reaction mix in 48 wells of a 96 well plate.

PAUSE POINT: The plate can be stored at –20 °C for 3 months.

54| Load 1 µl of cell lysate prepared in step 49 into each well

55| Perform one-step reverse transcription (RT) and specific target amplification (STA) reaction using the thermal cycling protocol below:

Cycle number	RT	Taq Activation	STA – 14 cycles	
			Denaturation	Annealing/Extension

1	15 min at 50 °C			
2		2 min at 95 °C		
3-16			15 sec at 95 °C	4 min at 60 °C
Hold				4 °C

56| Dilute the RT-STA product from step 55 by one third by adding 22 µl TE buffer to each reaction mixture. Please note that dilutions between one half and one fifth are also possible at this stage.

57| Split a 96-well plate in two halves. To each of the left-hand half 48 wells of the plate, add 3 µl of Fluidigm 2x assay loading reagent and 3 µl of each individual TaqMan™ assay (20X).

58| To the right-hand 48 wells, add 3.4 µl of the diluted cDNA solution obtained in step 53, 3.75 µl of the TaqMan™ master mix, and 0.4 µl of 20x gene sample loading reagent.

59| Follow instructions in the Fluidigm Real-Time PCR User Guide (http://www.fluidigm.com/home/fluidigm/Support/UG/Real-Time-PCR_Analysis_ug_68000088.pdf) to first prime the microfluidic qPCR chip (48.48 Dynamic Array™ IFC) with assays and samples, perform the qPCR, and use the Fluidigm Real-Time PCR Analysis software to calculate cycle threshold (Ct) values for each qPCR reaction.

60| Export the Ct values calculated in step 59 from Fluidigm software using the File → Export menu command and under "Save as type" selecting "Heat Map Results (*.csv)". This selection generates a comma-separated value (csv) file containing Ct values in table format with genes (assays) in columns and conditions (samples) in rows.

61| Import the Ct data from the file generated in step 60 into Matlab using the *csvread* function. In Matlab, Ct and relative expression can be readily explored and plotted. Relative gene expression can be calculated as 2^(Ct_reference – Ct_gene).

Automated analysis of microscopy images TIMING variable

62| Transfer images from the microscope computer to the analysis computer, in which CellProfiler will have been installed (see Equipment setup).

63| Using CellProfiler, use the "IdentifyPrimaryObjects" module to segment nuclei in images with a nuclear label (i.e. H2B-GFP fluorescent fusion protein), which automatically calculates and applies a threshold to the image so that only bright objects (nuclei) remain..

64| In CellProfiler, use the "IdentifySecondaryObjects" module to segment cytoplasm in images with cytoplasmic fluorescence (such as p65-dsRed) using the nuclei segmented in step 63 as a seed for each cytoplasm segmentation.

65| Use the "MeasureObjectIntensity" module in CellProfiler to quantify total and mean fluorescence for nucleus and cytoplasm in each image.

66| Use the "ExportToSpreadsheet" module in CellProfiler to save cell locations and fluorescence measurements in an Excel document.

67| Use the "TrackObject" module in CellProfiler to connect objects between images and produce single-cell trajectories of nuclear and cytoplasmic fluorescence over time. Alternatively, use a tracking algorithm implemented in Matlab to extract trajectories (such as http://physics.georgetown.edu/matlab/code.html)

TROUBLESHOOTING

Troubleshooting advice is detailed in Table 1.

Table 1. Troubleshooting Table

Step	Problem	Possible reason	Solution
20	Chip delamination	Poor bonding between layers	Use plasma treatment to increase bond strength
33	Cell clumping during loading	Cells left in suspension for too long	Agitate cell vial by gentle vortexing or tapping Trim ends of tubing
34Aiv and 34Biii	Poor cell attachment	Poor surface treatment	Ensure pluronic is washed away thoroughly before fibronectin treatment
34Aiv and 34Biii	Poor cell health in chip	Incomplete PDMS curing	Bake chip for an additional 24–48 h
		Cell medium evaporation from vial	Ensure that the cell medium input vials are tightly sealed to prevent evaporation
		Cell medium evaporation from chip	Ensure 95% humidity around chip and seal tubing slots on stage cover with tape
37	Debris are causing the chip to clog	Dust particles are present in the tubing	Flush inlet tubing briefly with cell medium or PBS before connecting to chip
		Cellular aggregates	Ensure cells fully dissociated by trituration before loading
		Particulates in media and/or serum	Pass cell medium and/or serum and reagents through a 0.2-μm syringe filter prior to preparing input vials
38	Microscope losing focus over time	Chip moving on stage during experiment	Secure tubing tightly to the stage using tape or stage clips to ensure that there is no force on chip during stage movement
49	Inconsistent volume in 96-well plate after cell retrieval	Evaporation from wells during retrieval procedure	Cover each well individually with tape immediately following cell retrieval

Timing

- Chip fabrication from existing molds, steps 1–9 (36 h)
- Setting up chip control system, steps 10–15 (1 day)
- Chip preparation on microscope, steps 16–23 (1–2 h)
- Applying chip surface treatments, steps 24–32 (6 h–overnight)
- Preparation of cell suspension and loading cells into chip, steps 33–34 (2–4 h)
- Imaging and feeding cells, steps 35–38 (4 h–overnight)
- Conduct cell stimulation experiment, steps 39–44 (variable, 2 h to 2 weeks)
- Retrieve cells from chip for gene expression analysis, steps 45–49 (1 h)
- High-throughput qPCR using Fluidigm BioMark System, steps 50–61 (4 h)
- Automated analysis of microscopy images, steps 62–67 (variable)

Anticipated Results

This protocol enables researchers to perform multiplexed stimulation and imaging of cells in high-throughput fashion. The correct application of the protocol enables to generate image data that convey information about single-cell dynamics under parallel input conditions extracted using automated methods (FIG 4A and B). When combined with high-throughput gene expression technologies, such as the BioMark™ system, using the cell culture chip enables the analysis of up to 96 genes in cells under complex stimulation patterns sampled finely in time (30 min between gene expression time points over a 12-h total duration in the example detailed here) (FIG 4C). Overall, this microfluidic single-cell analysis pipeline provides a new paradigm for live-cell studies, which overcomes problems with cell manipulation, precision, and automation to unravel complex questions around dynamic responses and their heterogeneity at the single cell level.

AUTHOR CONTRIBUTIONS

R.K. optimized the protocol and developed methods for cell retrieval and gene expression analysis, and wrote the manuscript. R.G.S. and A.A.L. are the original developers of the microfluidic cell culture chip and software. S.T. optimized the protocol for cell signaling studies and supervised the signaling project. All authors edited the manuscript.

ACKNOWLEDGEMENTS

We acknowledge S. Quake for supervising earlier stages of this work, M. Covert and his group for useful discussions and for making an earlier version of the image analysis software available, and for the gift of 3T3 cells with p65-DsRed fusion protein. This work was partly supported by a Swiss National Science Foundation grant to S. Tay.

COMPETING FINANCIAL INTERESTS

A.A.L. is an employee of Fluidigm Corporation. The other authors declare that they have no competing financial interests.

REFERENCES

1. Fernandez-Suarez, M. & Ting, A.Y. Fluorescent probes for super-resolution imaging in living cells. *Nature reviews. Molecular cell biology* **9**, 929-943 (2008).
2. Tay, S. et al. Single-cell NF-kappaB dynamics reveal digital activation and analogue information processing. *Nature* **466**, 267-271 (2010).
3. Albeck, J.G., Mills, G.B. & Brugge, J.S. Frequency-modulated pulses of ERK activity transmit quantitative proliferation signals. *Mol Cell* **49**, 249-261 (2013).
4. You, X. et al. Intracellular protein interaction mapping with FRET hybrids. *Proc Natl Acad Sci U S A* **103**, 18458-18463 (2006).
5. Reits, E.A. & Neefjes, J.J. From fixed to FRAP: measuring protein mobility and activity in living cells. *Nature cell biology* **3**, E145-147 (2001).
6. Kim, S.A., Heinze, K.G. & Schwille, P. Fluorescence correlation spectroscopy in living cells. *Nat Methods* **4**, 963-973 (2007).
7. Muramoto, T. et al. Live imaging of nascent RNA dynamics reveals distinct types of transcriptional pulse regulation. *Proc Natl Acad Sci U S A* **109**, 7350-7355 (2012).
8. Delebecque, C.J., Lindner, A.B., Silver, P.A. & Aldaye, F.A. Organization of intracellular reactions with rationally designed RNA assemblies. *Science* **333**, 470-474 (2011).
9. Yunger, S., Rosenfeld, L., Garini, Y. & Shav-Tal, Y. Quantifying the transcriptional output of single alleles in single living mammalian cells. *Nature protocols* **8**, 393-408 (2013).
10. Puchner, E.M., Walter, J.M., Kasper, R., Huang, B. & Lim, W.A. Counting molecules in single organelles with superresolution microscopy allows tracking of the endosome maturation trajectory. *Proc Natl Acad Sci U S A* **110**, 16015-16020 (2013).
11. Shim, S.H. et al. Super-resolution fluorescence imaging of organelles in live cells with photoswitchable membrane probes. *Proc Natl Acad Sci U S A* **109**, 13978-13983 (2012).
12. Spiller, D.G., Wood, C.D., Rand, D.A. & White, M.R. Measurement of single-cell dynamics. *Nature* **465**, 736-745 (2010).
13. Germain, R.N., Robey, E.A. & Cahalan, M.D. A decade of imaging cellular motility and interaction dynamics in the immune system. *Science* **336**, 1676-1681 (2012).
14. Kulesa, P.M. & Fraser, S.E. Cell dynamics during somite boundary formation revealed by time-lapse analysis. *Science* **298**, 991-995 (2002).
15. Cai, L., Dalal, C.K. & Elowitz, M.B. Frequency-modulated nuclear localization bursts coordinate gene regulation. *Nature* **455**, 485-490 (2008).
16. Neumann, B. et al. High-throughput RNAi screening by time-lapse imaging of live human cells. *Nat Methods* **3**, 385-390 (2006).

17. Junkin, M. & Tay, S. Microfluidic single-cell analysis for systems immunology. *Lab Chip* **14**, 1246-1260 (2014).
18. Levskaya, A., Weiner, O.D., Lim, W.A. & Voigt, C.A. Spatiotemporal control of cell signalling using a light-switchable protein interaction. *Nature* **461**, 997-1001 (2009).
19. Bugaj, L.J., Choksi, A.T., Mesuda, C.K., Kane, R.S. & Schaffer, D.V. Optogenetic protein clustering and signaling activation in mammalian cells. *Nat Methods* **10**, 249-252 (2013).
20. Grier, D.G. A revolution in optical manipulation. *Nature* **424**, 810-816 (2003).
21. Milias-Argeitis, A. et al. In silico feedback for in vivo regulation of a gene expression circuit. *Nature Biotechnology* **29**, 1114-1116 (2011).
22. Gómez-Sjöberg, R., Leyrat, A.A., Pirone, D.M., Chen, C.S. & Quake, S.R. Versatile, fully automated, microfluidic cell culture system. *Analytical chemistry* **79**, 8557-8563 (2007).
23. Vedel, S., Tay, S., Johnston, D.M., Bruus, H. & Quake, S.R. Migration of cells in a social context. *Proc Natl Acad Sci U S A* **110**, 129-134 (2013).
24. Cheong, R., Wang, C.J. & Levchenko, A. High content cell screening in a microfluidic device. *Molecular & cellular proteomics : MCP* **8**, 433-442 (2009).
25. Cheong, R., Wang, C.J. & Levchenko, A. Using a microfluidic device for high-content analysis of cell signaling. *Sci Signal* **2**, pl2 (2009).
26. Cheong, R., Rhee, A., Wang, C.J., Nemenman, I. & Levchenko, A. Information transduction capacity of noisy biochemical signaling networks. *Science* **334**, 354-358 (2011).
27. Frank, T. & Tay, S. Flow-switching allows independently programmable, extremely stable, high-throughput diffusion-based gradients. *Lab Chip* **13**, 1273-1281 (2013).
28. Hung, P.J., Lee, P.J., Sabounchi, P., Lin, R. & Lee, L.P. Continuous perfusion microfluidic cell culture array for high-throughput cell-based assays. *Biotechnology and bioengineering* **89**, 1-8 (2005).
29. Chung, K., Rivet, C.A., Kemp, M.L. & Lu, H. Imaging single-cell signaling dynamics with a deterministic high-density single-cell trap array. *Anal Chem* **83**, 7044-7052 (2011).
30. Faley, S.L. et al. Microfluidic single cell arrays to interrogate signalling dynamics of individual, patient-derived hematopoietic stem cells. *Lab Chip* **9**, 2659-2664 (2009).
31. Roach, K.L. et al. High throughput single cell bioinformatics. *Biotechnol Prog* **25**, 1772-1779 (2009).
32. Melin, J. & Quake, S.R. Microfluidic large-scale integration: the evolution of design rules for biological automation. *Annual review of biophysics and biomolecular structure* **36**, 213-231 (2006).
33. Vollmers, C., Sit, R.V., Weinstein, J.A., Dekker, C.L. & Quake, S.R. Genetic measurement of memory B-cell recall using antibody repertoire sequencing. *Proceedings of the National Academy of Sciences of the United States of America* **110**, 13463-13468 (2013).
34. Kalisky, T. & Quake, S.R. Single-cell genomics. *Nat Methods* **8**, 311-314 (2011).
35. Ottesen, E.A., Hong, J.W., Quake, S.R. & Leadbetter, J.R. Microfluidic digital PCR enables multigene analysis of individual environmental bacteria. *Science* **314**, 1464-1467 (2006).

36. Warren, L., Bryder, D., Weissman, I.L. & Quake, S.R. Transcription factor profiling in individual hematopoietic progenitors by digital RT-PCR. *Proc Natl Acad Sci U S A* **103**, 17807-17812 (2006).
37. Qin, D., Xia, Y. & Whitesides, G.M. Soft lithography for micro- and nanoscale patterning. *Nature protocols* **5**, 491-502 (2010).
38. Lecault, V. et al. High-throughput analysis of single hematopoietic stem cell proliferation in microfluidic cell culture arrays. *Nat Methods* **8**, 581-586 (2011).
39. Unger, M.A., Chou, H.P., Thorsen, T., Scherer, A. & Quake, S.R. Monolithic microfabricated valves and pumps by multilayer soft lithography. *Science (New York, NY)* **288**, 113-116 (2000).
40. Thorsen, T. Microfluidic Large-Scale Integration. *Science (New York, NY)* **298**, 580-584 (2002).
41. Berthier, E., Young, E.W. & Beebe, D. Engineers are from PDMS-land, Biologists are from Polystyrenia. *Lab Chip* **12**, 1224-1237 (2012).
42. Millet, L.J., Stewart, M.E., Sweedler, J.V., Nuzzo, R.G. & Gillette, M.U. Microfluidic devices for culturing primary mammalian neurons at low densities. *Lab on a Chip* **7**, 987-994 (2007).
43. Kolnik, M., Tsimring, L.S. & Hasty, J. Vacuum-assisted cell loading enables shear-free mammalian microfluidic culture. *Lab Chip* **12**, 4732-4737 (2012).
44. Landenberger, B., Hofemann, H., Wadle, S. & Rohrbach, A. Microfluidic sorting of arbitrary cells with dynamic optical tweezers. *Lab Chip* **12**, 3177-3183 (2012).
45. Wall, E.A. et al. Suppression of LPS-induced TNF-alpha production in macrophages by cAMP is mediated by PKA-AKAP95-p105. *Sci Signal* **2**, ra28 (2009).

3. DIGITAL SIGNALING DECOUPLES ACTIVATION PROBABILITY AND POPULATION HETEROGENEITY

This chapter under review at *eLife.*

Ryan A. Kellogg[1], Chengzhe Tian[2], Tomasz Lipniacki,[3] Stephen R. Quake,[4] Savaş Tay[1]*

Affiliations:
[1]Department of Biosystems Science and Engineering, ETH Zürich, Switzerland 4058.

[2]Niels Bohr Institute, University of Copenhagen, 2100 Copenhagen, Denmark

[3]Institute of Fundamental Technological Research, Polish Academy of Sciences, Warsaw, Poland.

[4]Department of Bioengineering, HHMI, Stanford University

*Correspondence: savas.tay@bsse.ethz.ch

R.A.K. performed dose-duration experiments, analyzed experiment and modeling results, prepared figures, and wrote the manuscript.

Abstract

Digital signaling enhances robustness of cellular decisions in noisy environments, but it is unclear how digital systems transmit temporal information about a stimulus. To understand how temporal input information is encoded and decoded by the NF-κB system, we studied transcription factor dynamics and gene regulation under dose- and duration-modulated inflammatory inputs. Mathematical modeling predicted and microfluidic single-cell experiments confirmed that stimulus area (concentration × duration) controls the fraction of cells that activate NF-κB in the population. However, stimulus shape determined NF-κB dynamics, cell-to-cell variability and gene expression phenotype. A sustained, weak stimulation lead to heterogeneous activation and delayed timing that is transmitted to gene expression. In contrast, a transient, strong stimulus with the same area caused rapid and uniform dynamics. These results show that digital NF-κB signaling enables multidimensional control of cellular phenotype via input profile, allowing parallel and independent control of single-cell activation probability and population heterogeneity.

Introduction

Cells must make decisions in noisy environments and have to decrease the chance of an errant response. One way cells can reduce sensitivity to noise is through digital or switch-like activation, such that only sufficiently strong signal exceeds an internal threshold and initiates a response. Switch-like activation occurs through diverse mechanisms (Shah and Sarkar, 2011). For example, observations in Xenopus oocytes showed that the MAPK pathway converted graded progesterone input to digital output in p42

MAPK that determined oocyte maturation (Petty et al., 1998). Subsequently, similar observations were seen for the JNK pathway (Bagowski and Ferrell, 2001). The scaffolding protein Spe5 was found to mediate digital MAPK activation of mating in yeast (Malleshaiah et al., 2010). More recently it was found that inflammasome signaling leads to all-or-none caspase1 activation that mediates apoptosis (Liu et al., 2013). Both amplitude (dose) and duration of input signals provide information that regulates cellular decisions. The duration of EGF stimulation modulates ERK dynamics and controls differentiation (Ahmed et al., 2014; von Kriegsheim et al., 2009b; Santos et al., 2007). Glucose sensing in plants showed that cells have gene regulatory network mechanisms to allow similar responses to a short, intense or sustained, moderate stimulus (Fu et al., 2014). Lymphocytes must precisely measure both antigen affinity and frequency to decide differentiation and proliferation (Gottschalk et al., 2012; Iezzi et al., 1998; Miskov-Zivanov et al., 2013). Although digital pathway activation allows robust cellular decision across a wide range of systems, it is not clear how digital signaling impacts processing of dose and duration information.

NF-κB is a critical regulator of phenotype in immunity and disease (Hayden and Ghosh, 2008), and responds digitally to TNF stimulation (Tay et al., 2010). NF-κB activation occurs for a multitude of cell stress and inflammatory signals that converge on the IKK (IκB Kinase) signaling hub, which induces degradation of the cytoplasmic inhibitor IκB and liberates NF-κB to enter the nucleus and regulate gene expression (Hayden and Ghosh, 2008). Multi-layered negative and positive feedback lead to complex pathway dynamics including oscillations (Hoffmann et al., 2002; Kellogg and Tay, 2015; Nelson et al., 2004; Tay et al., 2010). Although it is not fully resolved how NF-κB coordinates gene and phenotype regulation, it is known that the dynamics of NF-κB activation is involved in input-output specificity and information transmission (Ashall et al., 2009; Behar and Hoffmann, 2013; Selimkhanov et al., 2014; Werner et al., 2005). The core IκB-NF-κB regulatory module is well-studied and appears largely consistent across multiple stimulation contexts (Hoffmann et al., 2002; Hughey et al., 2014; Nelson et al., 2004; Tay et al., 2010), however the role of module upstream of IKK activation including receptor-ligand binding and adaptor protein assembly in input-encoding remains unclear.

To probe how diverse IKK-upstream signaling architectures impact NF-κB processing of pathogen- and host-associated inflammatory inputs, we used microfluidic cell culture to precisely modulate dose and duration of LPS and TNF stimuli and measured NF-κB dynamics using live-cell imaging (Figure 1) (Junkin and Tay, 2014; Kellogg et al., 2014). We found that LPS induces NF-κB activation in a digital way where cells respond in an all-or-none fashion, but in a distinct manner from TNF, with greater ultrasensitivity and pronounced input-dependent activation delay. Computational modeling predicted and experiments confirmed that LPS stimulus "area" (concentration × duration) controls the percentage of cells that activate in the population. Importantly, dynamics of NF-κB activation depend on input shape, so that a Long-duration, Low-dose (LL) signal induces delayed, heterogeneous activation timing in the population while a Short-duration, Strong-amplitude (SS) signal with the same area causes rapid activation without cell-to-cell timing variability (Figure 1). These results reveal a function for digital signaling beyond simple noise filtering: digital activation controls fate along a two dimensional space by allowing an input signal to independently control the population response (percentage of responding cells) and single-cell response (transcription factor dynamics and gene expression phenotype) though modulation of signal area and shape.

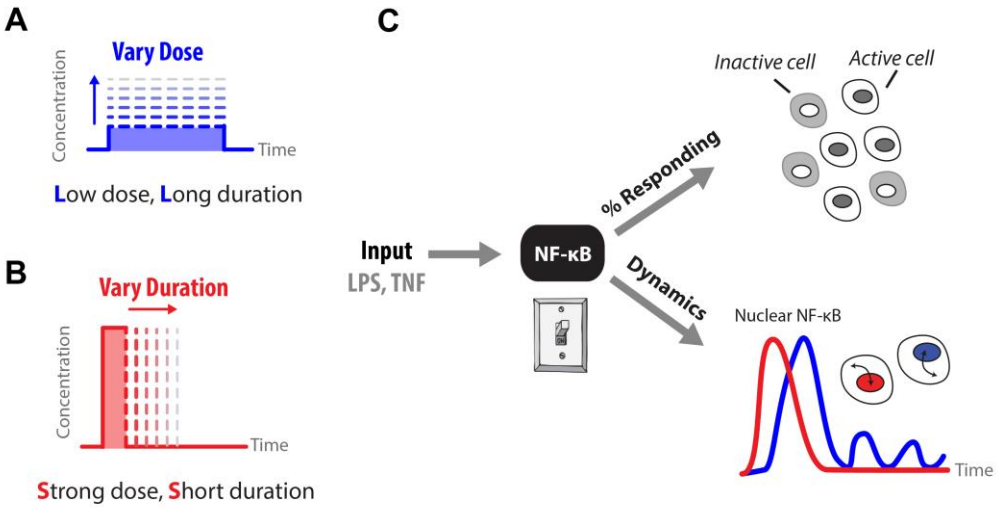

Figure 1. How does input profile determine digital signaling response? Since the amplitude and time profile of input signals depends on biological context, such as distance to an infection site or pathogen loading, we use microfluidics to manipulate dose (A) and duration (B) of LPS and TNF input signals, which induces digital activation of NF-κB. C) Switch-like digital NF-κB responses are analyzed in terms of fraction of cells that activate in the population and heterogeneity in the dynamic responses in activating cells.

Results

NF-κB switch dynamics distinguish pathogen (LPS) and host (TNF) signals

To initially evaluate the behavior of the LPS/NF-κB pathway, we stimulated 3T3 NF-κB reporter cells (Lee et al., 2009; Tay et al., 2010) with different concentrations of LPS in a microfluidic system (Gómez-Sjöberg et al., 2007; Kellogg et al., 2014), and performed time-lapse live microscopy to record NF-κB nucleus-cytoplasm translocation over time (Figure 2A). We found that LPS-exposed cells activated NF-κB in an ultrasensitive, all-or-none (digital) fashion. The population consisted of cells either fully responding or completely ignoring the LPS input, with the percentage of responding cells in the population scaling with LPS concentration, from 5% at 0.25ng/ml to 100% at 500ng/ml (Figure 2B, 2D). NF-κB dynamics in activating cells showed small oscillations beyond the first peak. When ligand is flowed continuously through the chamber to replace ligand loss due to cellular internalization, oscillations sustain for the duration of the stimulus (Figure 2—figure supplement 1A). Under low intensity LPS stimulation most cells did not respond (Figure 2C, 2D). This was a similar effect as previously observed under TNF (Tay et al., 2010). While both LPS and TNF are digital in preserving first peak area, the TNF-induced NF-κB initial peak becomes flatter and wider with increasing response time but unchanging onset time for decreasing input dose, while LPS experiences greater dose-dependent onset delay and timing variability and maintains a consistent peak shape (Figure 2C and Figure 2—figure supplement 1B). The dose-response curve for LPS was steeper than that for TNF (fitted to Hill dynamics reveals Hill coefficients of 2 and 1.5, respectively) (Figure 2C, Figure 2—figure supplement 1C, Figure 5—figure supplement 1B). These results indicate that the LPS pathway activates in a switch-like manner, with

increasing fraction of cells in the population responding as dose is increased, but with distinct activation dynamics compared to TNF input.

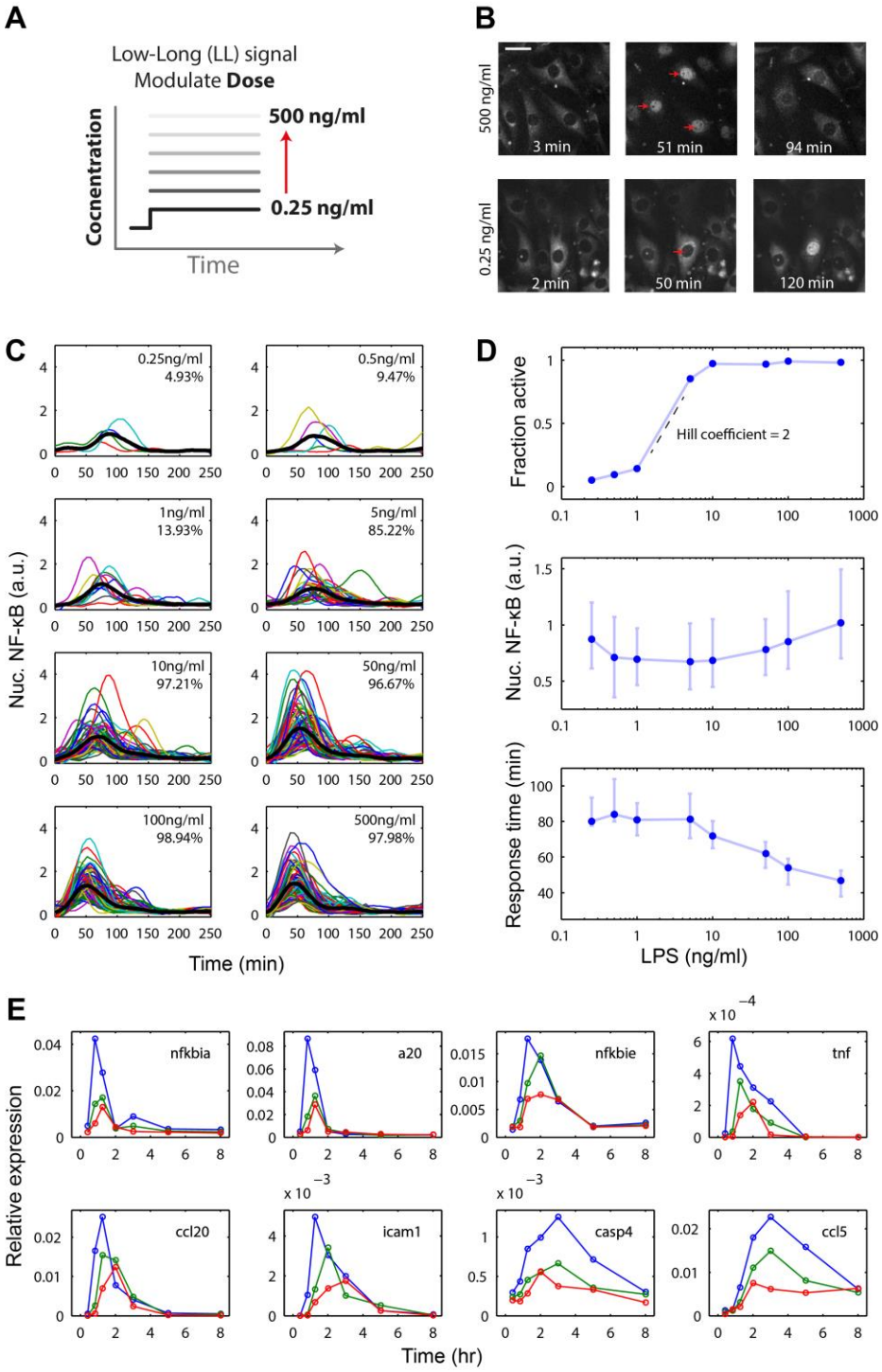

Figure 2. Digital, time-delayed NF-κB activation under varied LPS dose stimulation. (A) Cells process pathogen signal dose and duration to dynamically activate NF-κB, which induces gene

expression and coordinates the innate immune response. We test the role of pathogen load by varying LPS concentration from 0.25 ng/ml to 500 ng/ml using microfluidic cell culture. (B) Time series images of NF-κB activation following LPS treatment. Top row: high LPS dose causes nearly 100% of cells to respond synchronously. Bottom row: at low LPS concentration, less than 5% of cells respond and initiate NF-κB activation with variable, delayed timing. The cells respond digitally, with nearly all cytoplasmic NF-κB moving into the nucleus. The response amplitude (indicated by peak intensity of nuclear p65-dsRed fluorescence) depends on the initial NF-κB abundance in the nucleus and exhibits high variability across doses. (C) Trajectories of NF-κB activation (intensity of nuclear p65-dsRed) tracked in single cells over time for LPS doses ranging from 500 to 0.25 ng/ml. As the LPS dose decreases, response timing becomes delayed and variable, and the percent of responding cells in the population drops. Black line: mean dynamic profile over active cells. (D) Across the eight LPS doses tested: top panel - dose response curve of the fraction of active cells, middle panel – the intensity of nuclear NF-κB at the peak of the response, and lower panel – the delay time until initiation of the response. Peak nuclear NF-κB amplitude does not change in a significant way across 1000-fold change in LPS dose. The dose response shows a sharp drop in fraction of active cells between 1 and 5ng/ml concentration, indicating that the activation threshold is within this range for most cells. With lower dose, the delay time increases in both median duration and variability. (E) NF-κB dependent gene expression dynamics under varied LPS concentrations (blue – 500ng/ml, green – 100ng/ml, red – 50ng/ml). With lower LPS concentration, several genes show delayed induction.

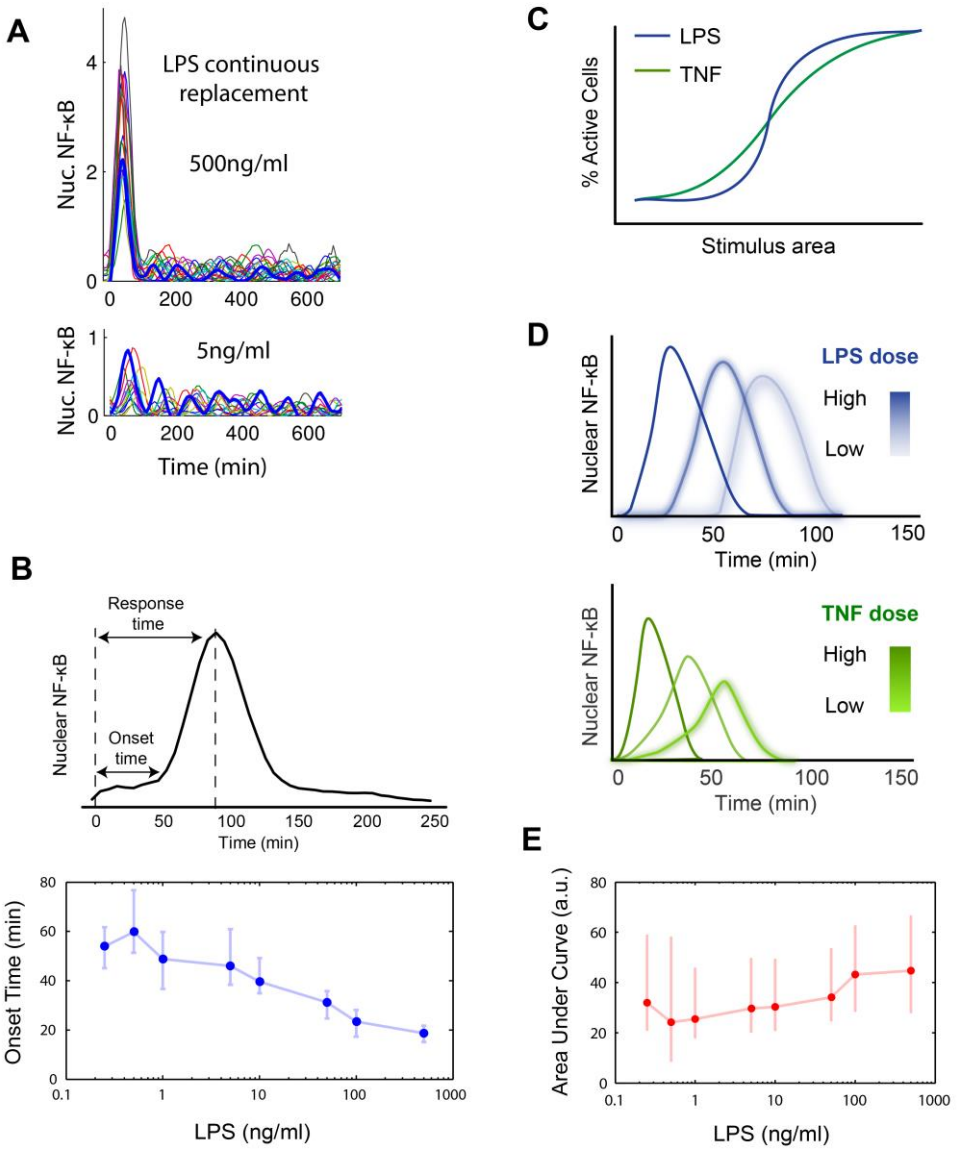

Figure 2–figure supplement 1. (A) Sustained NF-κB oscillations for continuously perfused LPS achieving constant LPS concentration. Bolded blue line: example cell. (B) Analysis of the LPS induced NF-κB nuclear localization peak. Lower LPS doses induce a pronounced onset delay, but the peak shape is mostly conserved across different doses. (C) Fraction of active cells for LPS vs TNF. (D) First peak time profile for LPS vs TNF. LPS leads to greater dose-dependent delay than TNF and a more conserved peak shape. (E) Area under the NF-κB localization curve show little change across all doses tested. Error bars show variability between individual cells (standard deviation) and dots show the mean values.

Response timing and single-cell heterogeneity depends on stimulus intensity

We next analyzed dynamics of the NF-κB response in those cells that activate. Notably, there were differences in the timing of the response for high versus low dose. High dose long duration input caused a

rapid response with the response peak occurring at approximately 35 minutes after stimulation. In contrast, low dose long duration (LL) input delayed the response significantly. At lowest doses the median delay until the peak of the response exceeded 80 minutes. The response at sustained, weak stimulation also exhibited large heterogeneity in the timing dynamics of the response (Figure 2C, 2D).

We next asked whether this delayed response impacted LPS and NF-κB mediated gene expression. We explored how the increase in delay for 500ng/ml LPS versus 50ng/ml LPS impacted gene regulation. Notably, gene expression of early and intermediate genes exhibited a dose-dependent delay (Figure 2E). The extent and magnitude of the dose-dependent delay and heterogeneity differs from TNF stimulation of the same cell type (Tay et al., 2010). While decreasing TNF dose altered the response slope, LPS response maintained a stereotypical peak shape that shifts later in time with lower dose (Figure 2E). Delayed gene expression observed under LPS stimulation contrasts with the TNF-α case in which we do not observe gene expression delay, with fixed gene activation peaks while the activation timing shifts for LPS (Tay et al, 2010) (Figure 2E). For early genes IκBα and A20, gene expression peak is shifted from 30 min to 1 hr after stimulation. IκBϵ expression shifts from maximum expression at 1 hr to 2 hr, and from 30 min to 2 hours for TNF mRNA under LPS input. Intermediate genes *Ccl2* and *Icam* shift expression peaks from 1hr to 2hr and from 1 hr to 3 hr (Figure 2E), respectively. Late genes *Ccl5* and *Casp4* do not reflect the delayed NF-κB activation due to slower induction kinetics. Overall, these results indicate that LPS induces digital NF-κB activation with an input dose-dependent delay that carries through to gene expression dynamics.

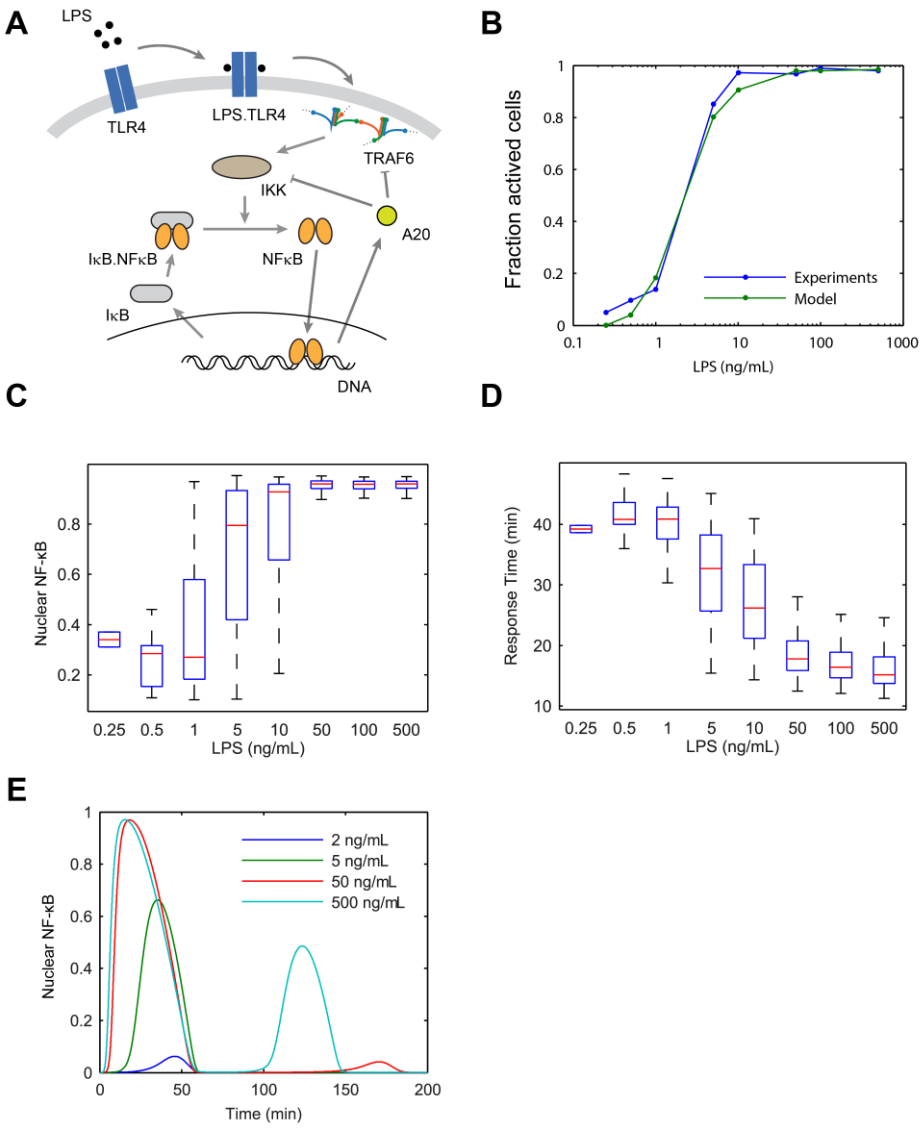

Figure 3. Model scheme and simulation of LPS dose modulation. (A) The scheme of the model. LPS binds TLR4 leading to TRAF6 activation which cooperatively activates IKK. Active IKK induces IκB degradation which allows NF-κB to enter the nucleus and upregulate expression of IκB and A20. New IκB sequesters NF-κB in the cytoplasm and A20 inhibits upstream pathway activation by IKK and TRAF6. (B) Simulated versus experimental LPS dose response. (C) NF-κB peak intensities (expressed as proportion of total NF-κB molecules in the nucleus). Although the model reproduces experimentally observed change in peak amplitude with dose, the extent of amplitude dose dependence is greater in the model. (D) NF-κB response time as function of LPS dose. (E) Sample simulated curves of nuclear NF-κB fractions under LPS treatment. Model parameters for the core NF-κB – IκB module are unchanged from the TNF model (Tay et al., 2010)**. Parameters for the LPS-specific portion of the model (Listed in Table 5 of Supplementary Mathematical Methods) are fit by minimizing L2-norm error between the model-estimated fraction of active cells and the experimentally measured fractions through a combination of automated and manual fitting (Supplementary Mathematical Methods).**

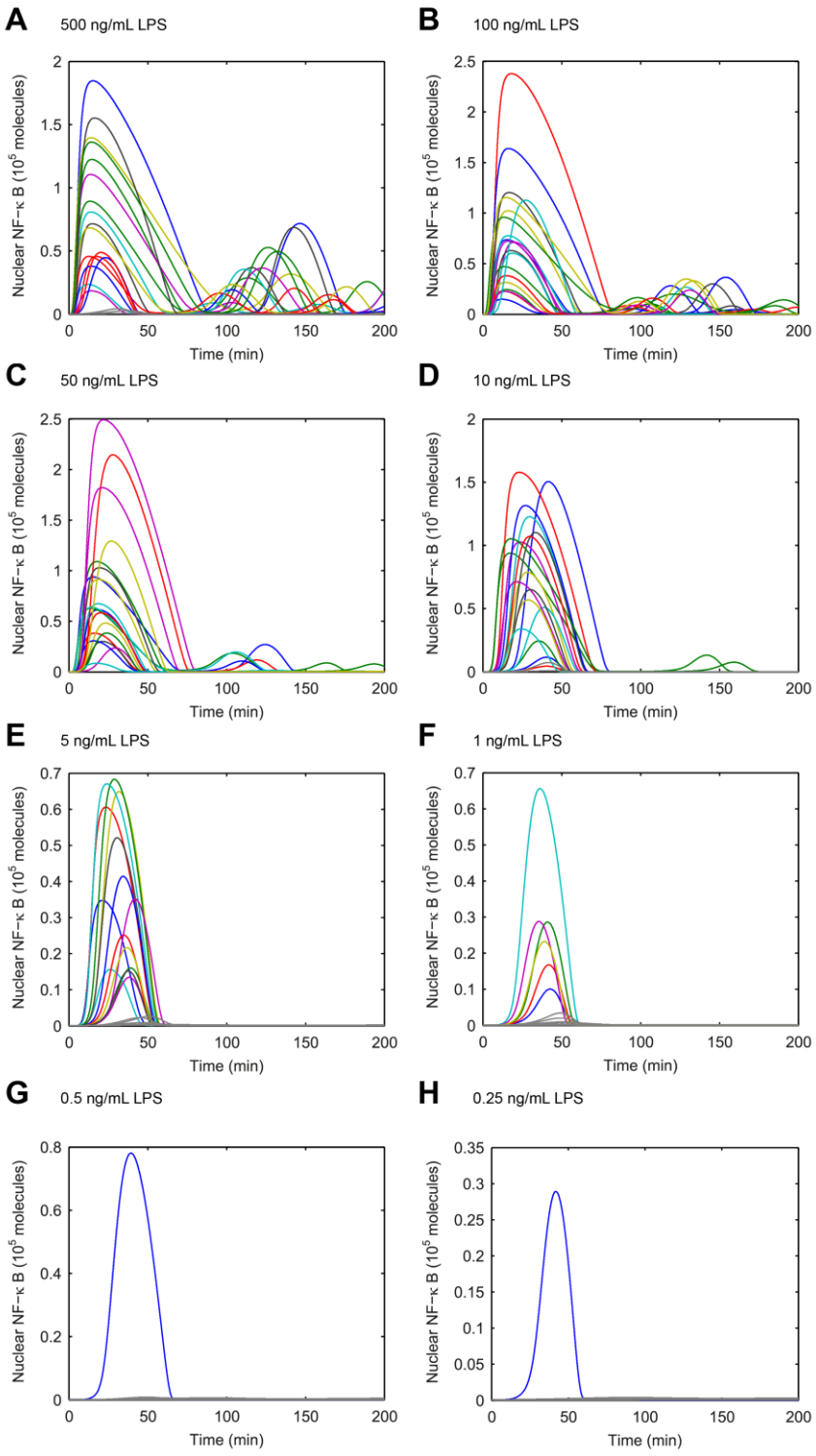

Figure 3–figure supplement 1. Simulated NF-κB trajectories for various doses of LPS treatment. LPS concentration decreases over time due to cellular internalization in sealed microfluidic chambers, leading to damped oscillations.

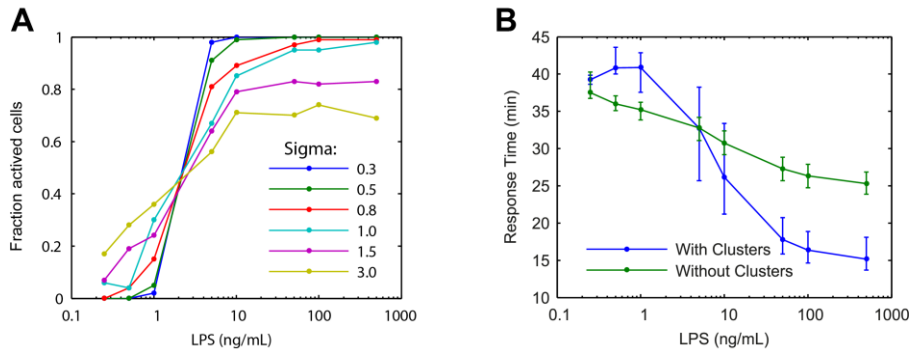

Figure 3—figure supplement 2. (A) Extrinsic noise is generated by selecting the number of TLR4 molecule for each cell from a lognormal distribution. Fraction of active cells was analyzed for increased TLR4 variability (parameter Sigma). With higher TLR4 number variability, the change in fraction of active cells becomes more gradual with changing LPS concentration. (B) Simulation response delay under varied LPS dose with and without clustering. Clustering mediating cooperative IKK activation is required to reproduce the experimentally observed response delay with decreasing LPS dose.

Cooperative IKK activation underlies dose-dependent response delay

To study how various pathway components upstream of IKK influence input information transfer to NF-κB, we developed a model of LPS-induced NF-κB switch activation. LPS activates NF-κB by TLR4 engagement via CD14, leading to TLR4 dimerization. TLR4 dimers recruit MyD88, IRAK2/4, and other adaptor proteins leading to higher-order assembly of Myddosome and TRAF6 lattice structures, which cooperatively activates IKK (Lin et al., 2010; Yin et al., 2009; Zanoni et al., 2011). Following IKK activation, nuclear NF-κB induces expression of IκBα, which negatively regulates NF-κB and IKK, respectively. Experimental IκBα expression kinetics were similar for LPS and TNF, despite induction delay under LPS (Figure 2E). Multiple efforts have modeled NF-κB pathway dynamics under TNF stimulation (Ashall et al., 2009; Hoffmann et al., 2002; Lipniacki et al., 2007; Paszek et al., 2010; Pękalski et al., 2013; Tay et al., 2010). We based our mathematical model on the core IKK-NF-κB regulatory module (Tay et al., 2010), which has been extensively validated experimentally.

To extend the NF-κB core model for LPS, we added species for LPS, TLR4, and TRAF6 (Supplementary Mathematical Methods) (Figure 3A). To introduce variability in the model we allowed fluctuation in the number of TLR4 receptor molecules between cells. TLR4 is expressed at relatively low level compared to CD14 and furthermore varies significantly between cells in the population (Zanoni et al., 2011). To account for cooperative activation due to Myddosome assembly and TRAF6 lattice formation, we model IKK phosphorylation by TRAF6 using Hill kinetics. The model reproduced the observed LPS induced NF-κB dynamics in single cells for different LPS doses (Figure 3B-D and Figure 3—figure supplement 1). The distinct feature of the proposed LPS model is the Myddosome formation leading to cooperative activation of IKK (Hill coefficient = 4), which simultaneously assures delay in activation observed experimentally for low doses, and steeper response curve than in the case of TNF stimulation (Figure 3 and Figure 2—figure supplement 1). Although the model reproduces experimentally observed change in peak amplitude with dose, the extent of amplitude dose dependence is greater in the model due to the

conservative Hill coefficient of 4. Model parameters for the core NF-κB – IκB module are unchanged from the TNF model (Tay et al., 2010). Parameters for the LPS-specific portion of the model (Listed in Table 5 of Supplementary Mathematical Methods) are fit by minimizing L2-norm error between the model-estimated fraction of active cells and the experimentally measured fractions through a combination of automated and manual fitting (Supplementary Mathematical Methods).

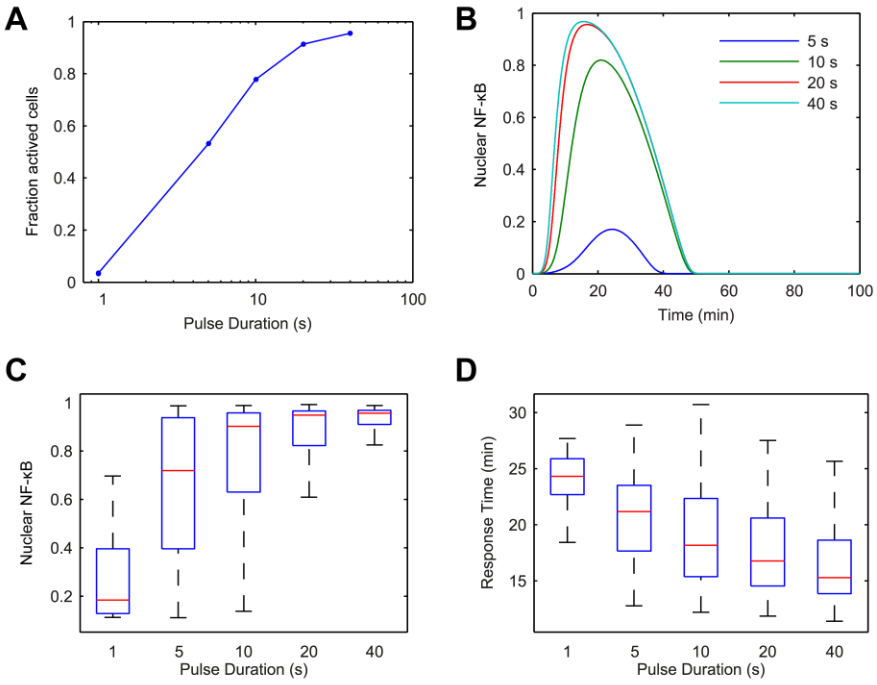

Figure 4. Model simulation predicts that stimulus duration controls fraction of activating cells and response timing variability. (A) Simulated fractions of activated cells under increasing duration of 500 ng/ml LPS pulse. (B) Sample simulated curves of NF-κB under 5 – 40 s duration LPS (500ng/ml) pulse. (C) Distributions of nuclear NF-κB amplitude and (D) response times of activating cells under various durations of LPS treatment.

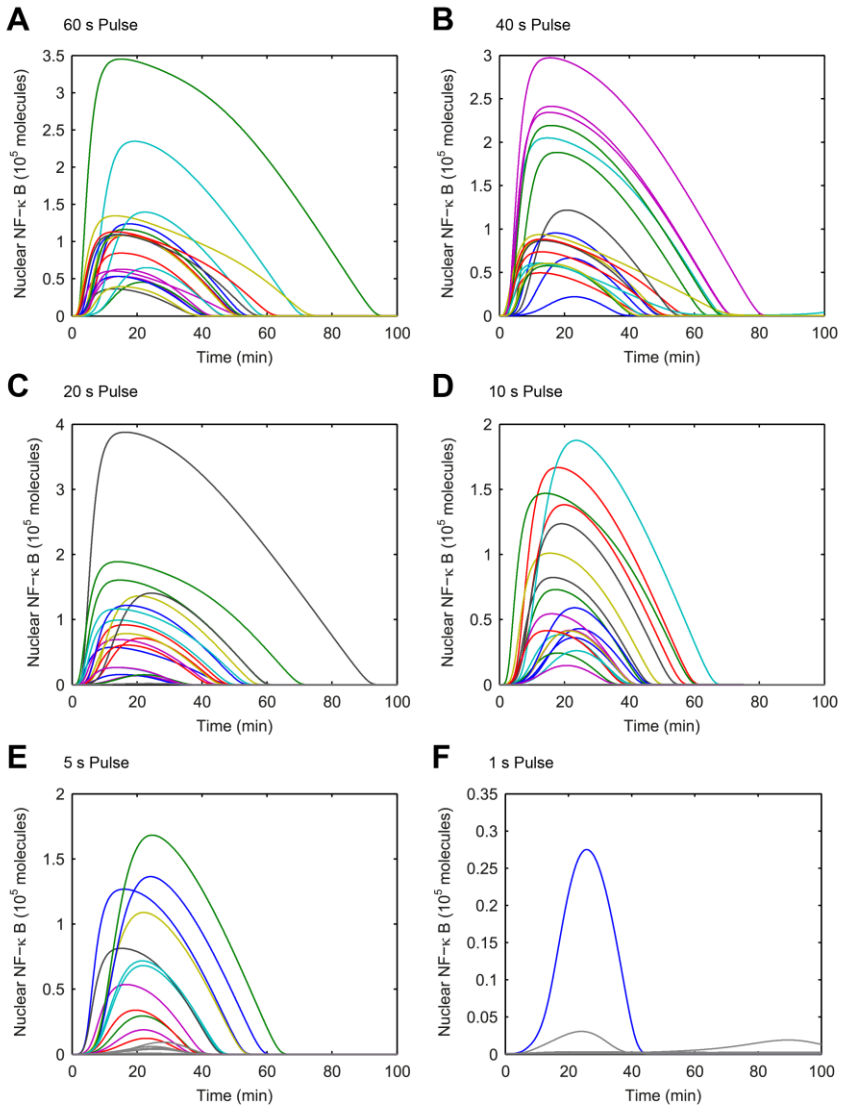

Figure 4–figure supplement 1. (A-F) Simulated NF-κB single-cell trajectories with randomly sampled numbers of TLR4 and NF-κB for 1 to 60 s durations of LPS exposure. The concentration of LPS is 500 ng/mL. Color: activated cells. Gray: inactivated cells.

Input duration controls activation probability independent of response heterogeneity

Cellular environments like infected tissue encode information in both amplitude and duration of input signals (Fu et al., 2014; Gottschalk et al., 2012). To understand how pathogen input signal duration and input area (concentration × duration) impact digital NF-κB signaling, we performed a simulated screen across a large range of LPS concentration and duration combinations using our model. We first observed that just as LPS concentration modulates fraction of active cells so does duration. Simulations keeping concentration high and changing input duration on a short, sub-minute timescale altered the percent of activating cells (Figure 4). Nearly all cells respond for durations exceeding one minute at 500ng/ml.

Notably, in contrast to changing concentration under constant long duration, which introduces timing delay and heterogeneity (Figure 2C, 3D), simulating sub-minute duration of a high amplitude signal controlled fraction of active cells while maintaining uniformly timed, rapid NF-κB responses (Figure 4B, 4D and Figure 4—figure supplement 1).

We experimentally provided pulsed LPS at 500ng/ml for sub-minute durations using microfluidic cell culture (Figure 5A). In agreement with simulation predictions, we found that precisely controlled stimulus duration regulated the activation of cells in the population in a strongly all-or-none manner, with 1 to 40 second duration LPS exposure (500 ng/ml) activating ~3-88% of the population (Figure 5B and Supplementary Videos 1-2). Short duration (i.e. 1s) stimulation, mimicking very brief exposure to bacteria, activated a small percentage of cells in the population. Moreover, under short duration, strong amplitude (SS) input, responses were fast and uniform in contrast to low, long (LL) stimulation that led to delayed, variable responses (Figure 5B, top row). For example, 3-5% activation occurred for both a 1s short pulse at 500ng/ml LPS (SS signal) and a 0.25 ng/ml constant input signal (LL signal) (Figure 5B, Figure 2D). However, modulating duration of the SS signal from 1 second to 40 seconds (activating 3.3% and 87.5% the population, respectively) changes median response timing by less than 2 minutes (Figure 5B). In contrast, modulating concentration of the LL signal from 0.25 to 500 ng/ml (activating 4.9% and 98% of the population, respectively) changes the response time more than 35 minutes (reduced from 80 to 43 minutes). Moreover, while the variability in the response time scales with dose under LL stimulation, timing variability remains low under duration-modulated SS stimulation (Figure 4D, 5C). From an immunological perspective, this experiment indicates that brief but high pathogen load leads to uniform and strong NF-κB response in the population, while chronic low-grade pathogen exposure leads to population variability and delay.

We next changed the stimulus type to TNF instead of LPS. In vivo, TNF is secreted from immune cells that come in contact with pathogenic signals like LPS. Again, we observed the phenomena that the fraction of active cells changed while the response timing did not (Figure 5—figure supplement 1). Together, these results indicated that SS input achieves control over the fraction of cells activating without affecting the dynamics in the response. Therefore duration sensing allows control of percentage of cells that produce a response without affecting response timing or heterogeneity. This contrasts to amplitude (concentration) sensing, where response dynamics in activating cells differs for high versus low amplitude. Since NF-κB dynamics influence gene expression, duration modulation to control percent population activation is therefore a strategy to achieve more homogeneous gene expression and phenotype outcomes between cells.

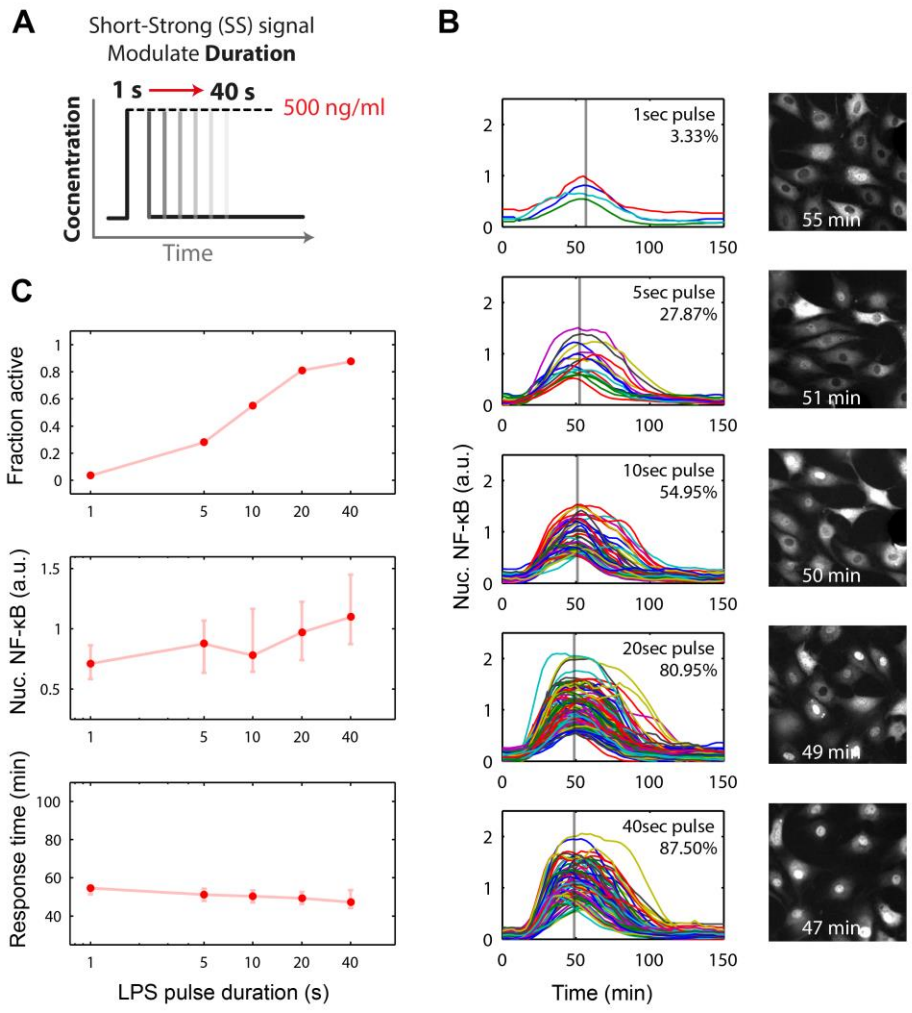

Figure 5. Short duration LPS pulse stimulation modulates responding cell fraction and fast, uniformly timed response. (A) LPS duration is manipulated using microfluidic cell culture in the range of 1-40 seconds. Dose is held constant at 500 ng/ml. (B) Single cell NF-κB trajectories for 1-40s duration LPS pulse stimulation. Short pulse LPS reduces variation in timing in the start of NF-κB activation. (C) Top panel: Fraction of active cells as a function of LPS pulse duration. Middle panel: NF-κB nuclear response intensity as a function of LPS pulse duration. Lower panel: Time of the NF-κB response peak as a function of LPS pulse duration. Error bars indicate standard deviation from the mean. Timing variability is dramatically reduced under short-pulsed stimulation (see Fig 2D for comparison to constant stimulation.

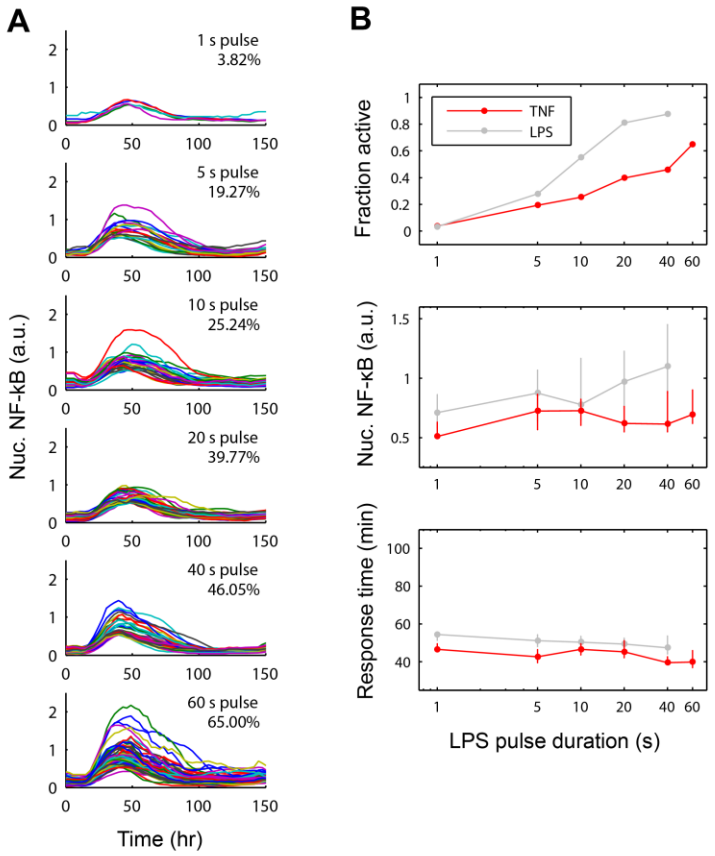

Figure 5—figure supplement 1. NF-κB dynamics under pulsed stimulation with TNF at 10ng/ml concentration. (A) Single cell NF-κB trajectories for TNF pulse durations of 1, 5, 10, 20, 40, and 60 seconds. The number and percent of activated cells is indicated in the plot. (B) Comparison of active NF-κB cell fraction (top), response amplitude (middle), and response time (bottom) under LPS vs TNF pulses. The fraction-active curve is less steep under TNF than LPS.

Stimulus area determines fraction of active cells in the population

We sought to fully characterize the relationship between signal amplitude and duration in NF-κB switch activation. Since modulating either amplitude or duration was able to change the percentage of activating cells, we hypothesized that the fraction of activation may depend on the area of the input (concentration × duration). Indeed, mathematical analytical analysis suggested that percent activating cells should scale with the input area (Supplementary Mathematical Methods).

To validate our mathematical analysis and clarify how digital activation integrates stimulus dose and duration, we performed simulations. Each simulation series fixed the LPS stimulus dose and varied duration from 1 to 500 seconds. The output of these simulations as a function of stimulus duration shows multiple dose-response curves that do not coincide, indicating that duration is not the only predictor of switching probability or fraction of active cells (Figure 6A). However, when instead plotted as a function

of stimulus area (concentration × duration), all simulation series closely coincide, indicating that stimulus area clearly determines the percentage of cells that activate in the population (Figure 6A).

To illustrate further the relationship between stimulus area and percentage of active cells, we plotted for each simulation dose the minimum duration needed to achieve 10%, 50%, and 90% activation (Figure 6B). This analysis revealed a reciprocal relationship between dose and duration in NF-κB switch activation (high dose requires less duration to achieve activation and vice versa). Simulations therefore supported analytical derivation of an "Area Rule", in which concentration × duration determines the percentage of cells that activate in the population for a given stimulus.

Importantly, for concentrations which achieve less that 100% activation, increasing the duration infinitely will not further increase the active fraction (Figure 6B). Once duration is sufficiently long to activate the maximal potential cell fraction for a given dose, further increases in area by lengthening duration do not further increase percentage of active cells, indicating a limitation in the Area Rule.

We next simulated whether the Area Rule holds for fluctuating signals. When we compared a constant input signal to square wave input signals, with one square wave that "starts high" and another that "starts low", simulation revealed an equal percentage of activating cells when the two opposing square waves have equal area (i.e., the duration is a multiple of the square wave period) (Figure 6C). Further, the fraction of active cells matched that for a constant input signal with the same area (Figure 6C). Performing identical simulations using a model of TNF induced NF-κB activation (Tay et al., 2010), we found that the Area Rule held also for the TNF network (Figure 6—figure supplement 1).

We found that in both the LPS amplitude-modulated and duration-modulated microfluidic experiments, stimulus area is an accurate predictor of fraction of active cells in the population (Figure 7A), as predicted by the model simulations. A majority of cells activate when LPS stimulation exceeds 3×10^3 ng-s/ml area. Together, experimental findings, simulations, and mathematical analysis demonstrate how cells integrate amplitude and duration of input signals in switch-like pathway activation. Stimulus area determines the effective "probability" that a given cell activates NF-κB (based on the percentage that activate in the population). These results indicate that the pathogen load (i.e. LPS dose) and duration of exposure (i.e. LPS pulse duration) are integrated by NF-κB system, and together determine the population response.

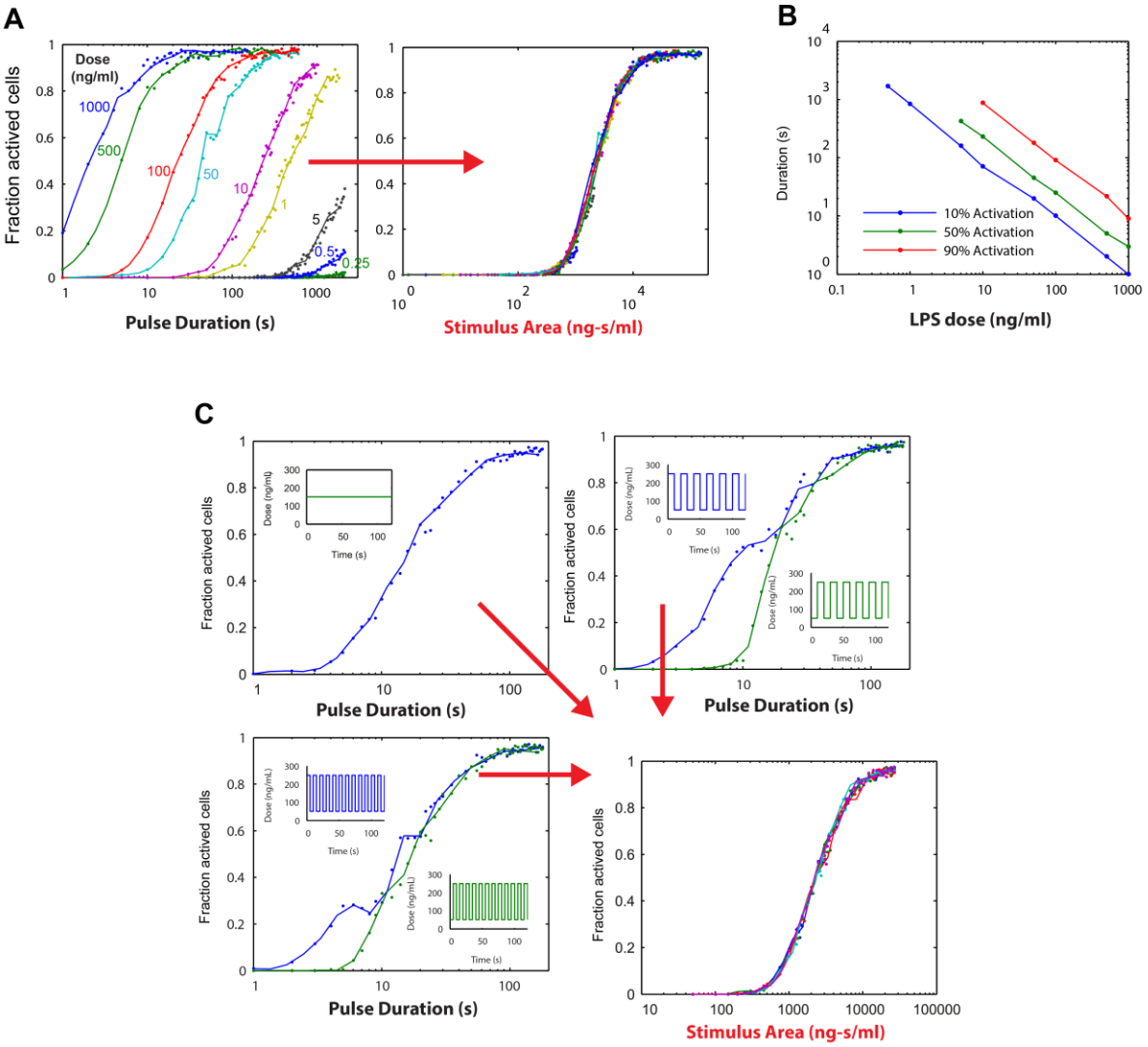

Figure 6. Simulations demonstrating an "Area Rule", i.e. the relationship between LPS stimulus area and fraction of active cells. (A) The simulated fractions of activated cells for pulsed inputs of LPS with various doses and durations. Each fraction is estimated by 500 independent simulations. When the points are plotted as a function of stimulus area (rather than duration), all points fall on the same curve, indicating that stimulus area tightly controls the fraction of active cells. (B) The minimal duration for certain fractions of activation as a function of dose. The minimal duration is determined by searching for the first tested time point where the estimated fractions of activation are above the threshold. The doses for which the threshold level cannot be achieved are not shown in the figure. Blue: 10% activation; Green: 50% activation; Red: 90% activation. (C) Further verification of the relationship between stimulus area and active cell fraction using square wave input profiles. Equal-area input was generated using either a single pulse (top left), square wave with 10 s period (lower left), or square wave with 20 s period (top right). Regardless of input shape, all simulated points fall on the same curve when plotted as a function of stimulus area. For square wave inputs, one input begins high (blue) while another input (green) begins low. Note that the

curves intersect for durations 10 s, 20 s, 30 s (or 20 s, 40 s, 60 s, … for the input with 20 s period) when area under the two signals is the same.

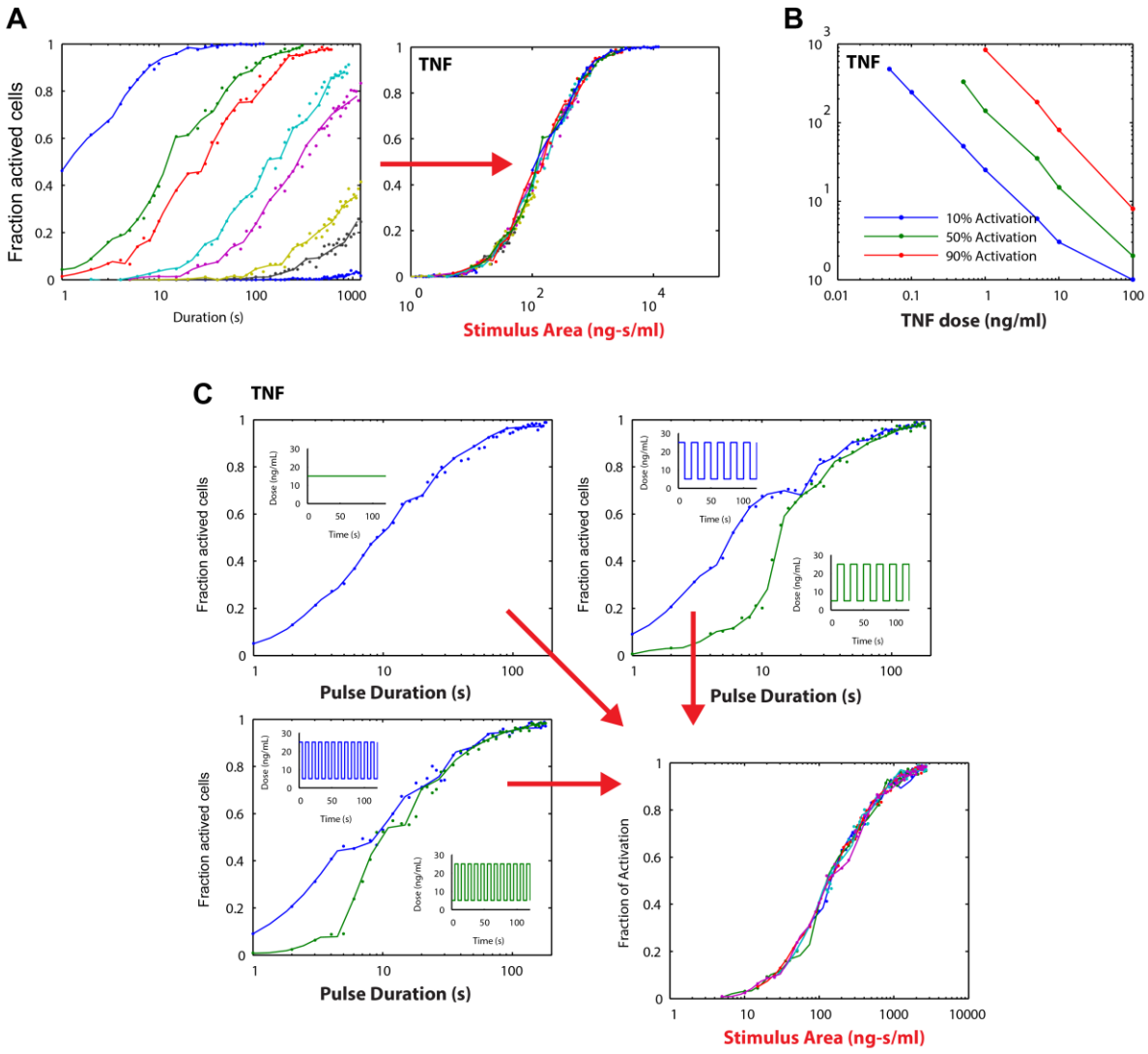

Figure 6—figure supplement 1. Stimulus area simulation using a TNF model (Tay et al., 2010) revealed that the "Area Rule" holds also for TNF.

Amplitude and duration information transfer via digital NF-κB activation

We showed that modulating stimulus amplitude altered response dynamics by changing the amount of activation delay. In contrast, modulating stimulus duration did not affect activation delay but changed the population variability. These findings indicate tradeoffs in dose versus duration sensing. Duration sensing allows for controlling only the population response while not affecting the single-cell response, so that it

is possible to achieve homogeneous dynamics and uniform phenotype in a desired proportion of cells. In contrast it may be useful to transmit information that can instruct different dynamics and phenotype, which is achieved by modulating dose. While dose information is transmitted through the NF-κB digital response, duration information is lost at the single cell level.

However, transmitting information using only dose modulation necessarily changes the percentage of cells in the population that respond. In physiological settings it may be desirable to transmit information without affecting population response, i.e. for a signal to affect response dynamics in activating cells without impacting the proportion that activate. To achieve this requires modulating both dose and duration to maintain input area, leading to a shift in input shape from a SS to a LL signal. Cells distinguish an SS versus LL signal profile based on NF-κB and gene expression dynamics. We show that an intense, brief (SS) signal induces distinct dynamics than a weak, sustained (LL) signal but the percentage of cells responding is the same in both cases (Figure 2C, Figure 5B). Response timing and intensity are dynamic features that provide information for discriminating input shape. Indeed, potting response delay as a function of stimulus area shows that SS and LL signals can be distinguished on the basis of response delay (Figure 7B). Cells can discern the category of the signal (whether SS or LL) for a given input area based on whether the response time falls above or below a separation line (Figure 7B). Modulating input amplitude associated with higher timing variability than input duration modulation for controlling the fraction of active cells (Figure 7—figure supplement 1A). Because response amplitude exhibits high variability between cells, amplitude alone does not provide sufficient information to discriminate an SS versus LL signal (Figure 7—figure supplement 1B). Physiological cues are in fact commonly transmitted by changing from an SS to an LL input profile (Fu et al., 2014; Iezzi et al., 1998). Biological systems therefore appear to take advantage of the unique ability of digital signaling to separate control of population and single-cell dynamics, by modulating input area to determine the proportion of cells that activate in the population and input shape to instruct to determine phenotype outcomes in the activating subset of cells (Figure 7).

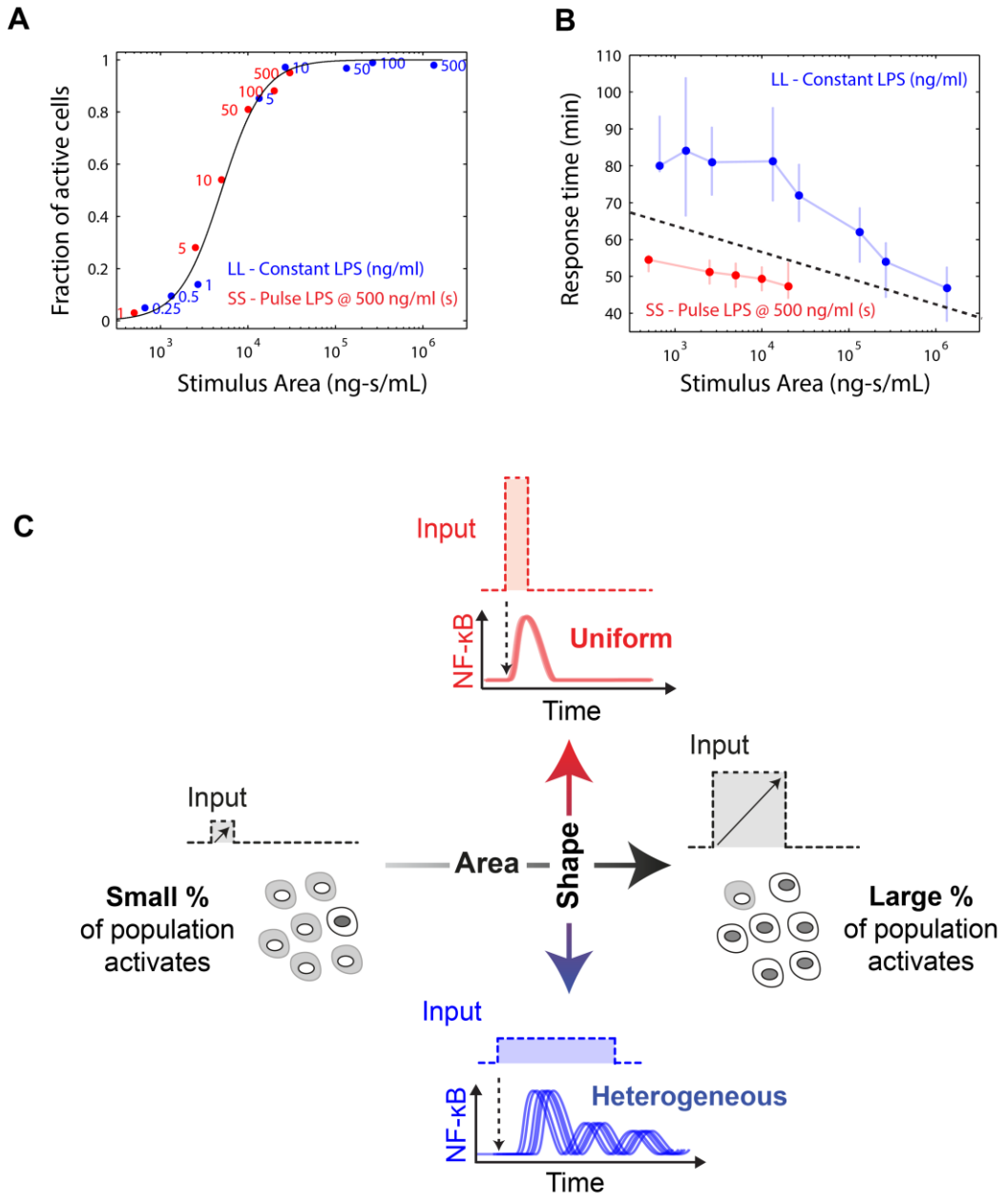

Figure 7. Stimulus area determines NF-κB population response. (A) Stimulus area determines fraction of active cells. The experimentally tested dose and duration inputs fall on the same hill-like activation curve when plotted as a function of stimulus area, as predicted by model simulations, indicating that total integrated ligand concentration (stimulus area) controls the probability of cell activation. These results show that pathogen load (i.e. LPS dose) and duration of exposure (i.e. LPS pulse duration) are integrated by NF-κB system, and together determine the population response. (B) Response time discriminates between sustained, low intensity (blue) and transient, high intensity (red) stimulus. (C) Input profile controls digital responses along two axes: Area controls the fraction of activated cells in the population. Shape controls dynamic heterogeneity in responding cells.

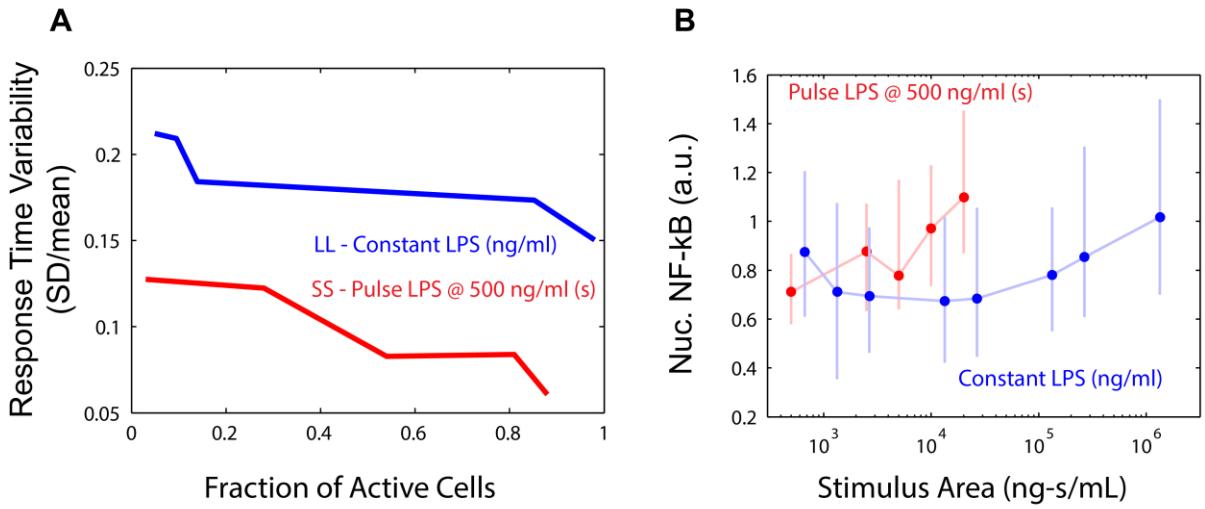

Figure 7—figure supplement 1. A) Comparison of cell-to-cell dynamic heterogeneity for different fractions of active cells for either constant or pulsed input (Figures 2 and 5). Pulsed (duration-modulated) LPS input (red) achieves lower response time variability than constant (dose-modulated) input for the same fraction of active cells. B) Unlike response delay, response intensity does not provide sufficient information to distinguish between pulsed LPS and constant LPS signals.

Discussion

This study asked how stimulus amplitude and duration determine NF-κB digital activation. Modeling and experiments showed that NF-κB activation is achieved by integrating the input: stimulus area (concentration × duration) controlled the percentage of cells that activated for both a "foreign" pathogen signal LPS and a "self" immune signal TNF (population response). Modeling did not perfectly reproduce the NF-κB dynamic trajectories in the data, and in particular showed more dose-dependent first peak amplitude variation than observed in experiments. However, switch dynamics and gene expression phenotype varied depending on the input dose (single-cell response), with rapid homogeneous responses at high dose and delayed heterogeneous responses at low dose. Dynamics of transcription factor activation determine the timing and specificity of gene expression and phenotype responses (Kobayashi et al., 2009; Purvis et al., 2012; Werner et al., 2005). Therefore, intercellular signaling systems may achieve distinct phenotype outcomes by controlling the input shape (whether SS or LL) – while input area determines percentage of cells that respond (Figure 7B). Greater heterogeneity with decreasing dose and decreased heterogeneity under short duration input is measured by coefficient of variation (Figure 7—figure supplement 1).

In lymphocyte signaling, T and B cells cell fate depends on both antigen quality (affinity) and quantity (amount of presented antigen). Antigen quality is encoded in the duration of receptor-antigen contact, with characteristic interaction times on the order of seconds (Altan-Bonnet and Germain, 2005;

Gottschalk et al., 2012; Miskov-Zivanov et al., 2013). T and B cell receptor binding with antigen-MHC triggers digital activation and cell fate control via NF-κB (Gerondakis et al., 2014; Kingeter et al., 2010; Oh and Ghosh, 2013; Shinohara et al., 2014). A reciprocal relationship is observed between antigen quality and quantity in lymphocyte activation: Higher antigen affinity requires lower dose of antigen to trigger T cell proliferation, and inversely, lower affinity requires higher dose (Gottschalk et al., 2012). Moreover, an intense, transient compared to a weak, sustained signal induces positive versus negative selection of naïve thymic T cells (Iezzi et al., 1998) and T helper cell differentiation into alternatively CD4 or CD8 status (Adachi and Iwata, 2002). Therefore analogous to our findings, while a combination of antigen dose and contact duration determines the probability of activation, input shape determined by relationship between antigen quality and quantity decides the phenotypic outcome of lymphocyte activation.

We show that switch-like signaling enables parallel and independent control over response probability and response dynamics: while stimulus area (concentration × duration, or antigen quantity × quality) regulates the percentage of cells that respond, the stimulus shape (for example, whether short-strong or low-long, or antigen quality/quantity ratio) determines the response timing and gene expression phenotype in responding cells. Dose and duration sensing may be beneficial in different contexts. Dose information is encoded in the delay timing and heterogeneity of NF-κB response. On the other hand, modulating duration on the sub-minute timescale does not regulate response dynamics. Indeed, achieving control of percentage active in a population without introducing heterogeneity requires modulating duration of a high-dose input (Figure 4). It was shown that signaling dynamics mediates transfer of input dose information (Selimkhanov et al., 2014). We find that while dose information is transmitted through dynamics of NF-κB activation, on short (minute) timescales duration information is lost in the single-cell response but retained in the population response (fraction of activated cells).

Between the innate immune signals TNF and LPS, we found that LPS exhibits greater ultrasensitivity (a steeper stimulus-response curve) and more pronounced activation delay than TNF. Both of these features are explained by higher coopertivity in IKK activation for LPS than for TNF (Figure 3—figure supplement 2B). Distinct higher-order adapter protein architectures may activate IKK with different effective coopertivities (Kazmierczak and Lipniacki, 2010). While TNF signaling activates formation of a filamentous amyloid complex involving RIP1 and RIP3 kinases, LPS signaling is mediated through helical assembly of the Myddosome complex (Lin et al., 2010) which interfaces with a TRAF6 lattice structure to activate IKK (Yin et al., 2009). Heterogeneity in switching threshold between cells may arise from cell-to-cell expression differences in signalosome components such as RIP1/3, MyD88, IRAK2/4, and TRAF6, leading to altered kinetics of signalosome assembly and IKK activation. Because the IKK hub mediates NF-κB responses for a multitude of input types and coordinates cross-talk with other signaling pathways, understanding how different signalosome architectures induce specific responses paves the way to interventions directed at switch-like signaling to modulate population and individual cell dynamics towards therapeutic outcomes (Behar et al., 2013; Negro et al., 2008).

In this study we have shown that the switch-like character of NF-κB activation enables orthogonal control over two critical aspects of the response – probability of activation (fraction of active cells) and the heterogeneity of response – through the area and shape of the input profile. Secretion of signaling molecules often occurs in discrete or quantized way in the form of secretory bursts, and particularly in the case of short range paracrine signaling, cells may produce brief but intense secretion to achieve, for

example, low probability but high predictability responses (non-heterogeneous dynamics). Overall these results expand the repertoire of functions for digital signaling beyond increasing robustness to also facilitate multidimensional phenotype control based on temporal information in input signals.

REFERENCES

Adachi, S., and Iwata, M. (2002). Duration of calcineurin and Erk signals regulates CD4/CD8 lineage commitment of thymocytes. Cell. Immunol. *215*, 45–53.

Ahmed, S., Grant, K.G., Edwards, L.E., Rahman, A., Cirit, M., Goshe, M.B., and Haugh, J.M. (2014). Data-driven modeling reconciles kinetics of ERK phosphorylation, localization, and activity states. Mol. Syst. Biol. *10*, 718.

Albeck, J.G., Mills, G.B., and Brugge, J.S. (2013). Frequency-Modulated Pulses of ERK Activity Transmit Quantitative Proliferation Signals. Mol. Cell *49*, 249–261.

Altan-Bonnet, G., and Germain, R.N. (2005). Modeling T cell antigen discrimination based on feedback control of digital ERK responses. PLoS Biol. *3*, 1925–1938.

Aoki, K., Yamada, M., Kunida, K., Yasuda, S., and Matsuda, M. (2011). Processive phosphorylation of ERK MAP kinase in mammalian cells. Proc. Natl. Acad. Sci. U. S. A. *108*, 12675–12680.

Arumugam, M., Raes, J., Pelletier, E., Le Paslier, D., Yamada, T., Mende, D.R., Fernandes, G.R., Tap, J., Bruls, T., Batto, J.-M., et al. (2011). Enterotypes of the human gut microbiome. Nature *473*, 174–180.

Ashall, L., Horton, C. a, Nelson, D.E., Paszek, P., Harper, C. V, Sillitoe, K., Ryan, S., Spiller, D.G., Unitt, J.F., Broomhead, D.S., et al. (2009). Pulsatile stimulation determines timing and specificity of NF-kappaB-dependent transcription. Science *324*, 242–246.

Baeuerle, P. a, and Baltimore, D. (1988). Activation of DNA-binding activity in an apparently cytoplasmic precursor of the NF-kappa B transcription factor. Cell *53*, 211–217.

Bagowski, C.P., and Ferrell, J.E. (2001). Bistability in the JNK cascade. Curr. Biol. *11*, 1176–1182.

Baker, R.G., Hayden, M.S., and Ghosh, S. (2011). NF-κB, inflammation, and metabolic disease. Cell Metab. *13*, 11–22.

Baltimore, D. (2009). Discovering NF- k B. 1–4.

Beer, N.R., Wheeler, E.K., Lee-Houghton, L., Watkins, N., Nasarabadi, S., Hebert, N., Leung, P., Arnold, D.W., Bailey, C.G., and Colston, B.W. (2008). On-chip single-copy real-time reverse-transcription PCR in isolated picoliter droplets. Anal. Chem. *80*, 1854–1858.

Behar, M., and Hoffmann, A. (2013). Tunable signal processing through a kinase control cycle: The IKK signaling node. Biophys. J. *105*, 231–241.

Behar, M., Barken, D., Werner, S.L., and Hoffmann, A. (2013). Theory The Dynamics of Signaling as a Pharmacological Target. Cell *155*, 448–461.

Bhatia, S.N., and Ingber, D.E. (2014). Microfluidic organs-on-chips. Nat. Biotechnol. *32*, 760–772.

Ca, A. (1998). Calcium oscillations increase the efficiency and specificity of gene expression. *392*, 933–936.

Cai, L., Dalal, C.K., and Elowitz, M.B. (2008). Frequency-modulated nuclear localization bursts coordinate gene regulation. Nature *455*, 485–490.

Dolmetsch, R.E., Lewis, R.S., Goodnow, C.C., and Healy, J.I. (1997). Differential activation of transcription factors induced by Ca2+ response amplitude and duration. Nature *386*, 855–858.

Eldar, A., and Elowitz, M.B. (2010). Functional roles for noise in genetic circuits. Nature *467*, 167–173.

Elowitz, M.B., Levine, A.J., Siggia, E.D., and Swain, P.S. (2002). Stochastic gene expression in a single cell. Sci. Signal. *297*, 1183.

Fu, Y., Lim, S., Urano, D., Tunc-ozdemir, M., Phan, N.G., and Elston, T.C. (2014). Theory Reciprocal Encoding of Signal Intensity and Duration in a Glucose-Sensing Circuit. Cell *156*, 1084–1095.

Furusawa, Y., Obata, Y., Fukuda, S., Endo, T. a, Nakato, G., Takahashi, D., Nakanishi, Y., Uetake, C., Kato, K., Kato, T., et al. (2013). Commensal microbe-derived butyrate induces the differentiation of colonic regulatory T cells. Nature *504*, 446–450.
Gerondakis, S., Fulford, T.S., Messina, N.L., and Grumont, R.J. (2014). NF-κB control of T cell development. Nat. Immunol. *15*, 15–25.
Gómez-Sjöberg, R., Leyrat, A. a., Pirone, D.M., Chen, C.S., and Quake, S.R. (2007). Versatile, fully automated, microfluidic cell culture system. Anal. Chem. *79*, 8557–8563.
Gottschalk, R. a., Hathorn, M.M., Beuneu, H., Corse, E., Dustin, M.L., Altan-Bonnet, G., and Allison, J.P. (2012). Distinct influences of peptide-MHC quality and quantity on in vivo T-cell responses. Proc. Natl. Acad. Sci. *109*, 881–886.
Han, Q., Bagheri, N., Bradshaw, E.M., Hafler, D. a., Lauffenburger, D. a., and Love, J.C. (2012). From the Cover: Polyfunctional responses by human T cells result from sequential release of cytokines. Proc. Natl. Acad. Sci. *109*, 1607–1612.
Hao, S., and Baltimore, D. (2013). RNA splicing regulates the temporal order of TNF-induced gene expression. Proc. Natl. Acad. Sci. U. S. A. *110*, 11934–11939.
Hayden, M.S., and Ghosh, S. (2008). Shared Principles in NF-kB Signaling. Cell *132*, 344–362.
Hoffmann, A., and Baltimore, D. (2006). Circuitry of nuclear factor kappaB signaling. Immunol. Rev. *210*, 171–186.
Hoffmann, A., Levchenko, A., Scott, M.L., and Baltimore, D. (2002). The IkappaB-NF-kappaB signaling module: temporal control and selective gene activation. Science *298*, 1241–1245.
Hong, J.W., Studer, V., Hang, G., Anderson, W.F., and Quake, S.R. (2004). A nanoliter-scale nucleic acid processor with parallel architecture. Nat. Biotechnol. *22*, 435–439.
Hornung, G., and Barkai, N. (2008). Noise propagation and signaling sensitivity in biological networks: a role for positive feedback. PLoS Comput. Biol. *4*, e8.
Hughey, J.J., Gutschow, M. V, Bajar, B.T., and Covert, M.W. (2014). Single-cell variation leads to population invariance in NF- κB signaling dynamics.
Huh, D., Kim, H.J., Fraser, J.P., Shea, D.E., Khan, M., Bahinski, A., Hamilton, G. a, and Ingber, D.E. (2013). Microfabrication of human organs-on-chips. Nat. Protoc. *8*, 2135–2157.
Iezzi, G., Karjalainen, K., and Lanzavecchia, A. (1998). The Duration of Antigenic Stimulation Determines the Fate of Naive and Effector T Cells. Immunity *8*, 89–95.
Iliescu, C., Taylor, H., Avram, M., Miao, J., and Franssila, S. (2012). A practical guide for the fabrication of microfluidic devices using glass and silicon. Biomicrofluidics *6*, 16505–1650516.
Imayoshi, I., Isomura, A., Harima, Y., Kawaguchi, K., Kori, H., Miyachi, H., Fujiwara, T., Ishidate, F., and Kageyama, R. (2013). Oscillatory control of factors determining multipotency and fate in mouse neural progenitors. Science *342*, 1203–1208.
Junkin, M., and Tay, S. (2014). Microfluidic single-cell analysis for systems immunology. Lab Chip *14*, 1246–1260.
Kazmierczak, B., and Lipniacki, T. (2010). Spatial gradients in kinase cascade regulation. IET Syst. Biol. *4*, 348–355.
Kellogg, R.A., and Tay, S. (2015). Noise Facilitates Transcriptional Control under Dynamic Inputs. Cell *160*, 381–392.
Kellogg, R.A., Gómez-Sjöberg, R., Leyrat, A.A., and Tay, S. (2014). High-throughput microfluidic single-cell analysis pipeline for studies of signaling dynamics. Nat. Protoc. *9*, 1713–1726.
Kingeter, L.M., Paul, S., Maynard, S.K., Cartwright, N.G., and Schaefer, B.C. (2010). Cutting edge: TCR ligation triggers digital activation of NF-kappaB. J. Immunol. *185*, 4520–4524.
Knutson, C.G., Mangerich, A., Zeng, Y., Raczynski, A.R., Liberman, R.G., Kang, P., Ye, W., Prestwich, E.G., Lu, K., Wishnok, J.S., et al. (2013). Chemical and cytokine features of innate immunity characterize serum and tissue profiles in inflammatory bowel disease. Proc. Natl. Acad. Sci. U. S. A. *110*, E2332–E2341.
Kobayashi, T., Mizuno, H., Imayoshi, I., Furusawa, C., Shirahige, K., and Kageyama, R. (2009). The cyclic gene Hes1 contributes to diverse differentiation responses of embryonic stem cells. 1870–1875.

Von Kriegsheim, A., Baiocchi, D., Birtwistle, M., Sumpton, D., Bienvenut, W., Morrice, N., Yamada, K., Lamond, A., Kalna, G., Orton, R., et al. (2009a). Cell fate decisions are specified by the dynamic ERK interactome. Nat. Cell Biol. *11*, 1458–1464.
Von Kriegsheim, A., Baiocchi, D., Birtwistle, M., Sumpton, D., Bienvenut, W., Morrice, N., Yamada, K., Lamond, A., Kalna, G., Orton, R., et al. (2009b). Cell fate decisions are specified by the dynamic ERK interactome. Nat. Cell Biol. *11*, 1458–1464.
Lee, T.K., Denny, E.M., Sanghvi, J.C., Gaston, J.E., Maynard, N.D., Hughey, J.J., and Covert, M.W. (2009). A noisy paracrine signal determines the cellular NF-kappaB response to lipopolysaccharide. Sci. Signal. *2*, ra65.
Leman, M., Abouakil, F., Griffiths, A.D., and Tabeling, P. (2014). Droplet-based microfluidics at the femtolitre scale. Lab Chip.
Levine, J.H., Lin, Y., and Elowitz, M.B. (2013a). Functional roles of pulsing in genetic circuits. Science *342*, 1193–1200.
Levine, J.H., Lin, Y., and Elowitz, M.B. (2013b). Functional roles of pulsing in genetic circuits. Science *342*, 1193–1200.
Lin, S.-C., Lo, Y.-C., and Wu, H. (2010). Helical assembly in the MyD88-IRAK4-IRAK2 complex in TLR/IL-1R signalling. Nature *465*, 885–890.
Lipniacki, T., Puszynski, K., Paszek, P., Brasier, A.R., and Kimmel, M. (2007). Single TNFalpha trimers mediating NF-kappaB activation: stochastic robustness of NF-kappaB signaling. BMC Bioinformatics *8*, 376.
Liu, B., Bhatt, D., Oltvai, Z.N., Greenberger, J.S., and Bahar, I. (2014). Significance of p53 dynamics in regulating apoptosis in response to ionizing radiation, and polypharmacological strategies. Sci. Rep. *4*, 6245.
Liu, T., Yamaguchi, Y., Shirasaki, Y., Shikada, K., Yamagishi, M., Hoshino, K., Kaisho, T., Takemoto, K., Suzuki, T., Kuranaga, E., et al. (2013). Single-Cell Imaging of Caspase-1 Dynamics Reveals an All-or-None Inflammasome Signaling Response. Cell Rep. *8*, 974–982.
Mali, P., Yang, L., Esvelt, K.M., Aach, J., Guell, M., DiCarlo, J.E., Norville, J.E., and Church, G.M. (2013). RNA-guided human genome engineering via Cas9. Science *339*, 823–826.
Malleshaiah, M.K., Shahrezaei, V., Swain, P.S., and Michnick, S.W. (2010). The scaffold protein Ste5 directly controls a switch-like mating decision in yeast. Nature *465*, 101–105.
Marcus, J.S., Anderson, W.F., and Quake, S.R. (2006). Microfluidic single-cell mRNA isolation and analysis. Anal. Chem. *78*, 3084–3089.
McDonnell, M.D., and Ward, L.M. (2011). The benefits of noise in neural systems: bridging theory and experiment. Nat. Rev. Neurosci. *12*, 415–426.
Meffert, M.K., and Baltimore, D. (2005). Physiological functions for brain NF-kappaB. Trends Neurosci. *28*, 37–43.
Miskov-Zivanov, N., Turner, M.S., Kane, L.P., Morel, P. a, and Faeder, J.R. (2013). The duration of T cell stimulation is a critical determinant of cell fate and plasticity. Sci. Signal. *6*, ra97.
Negro, A., Dodge-Kafka, K., and Kapiloff, M.S. (2008). Signalosomes as therapeutic targets. Prog. Pediatr. Cardiol. *25*, 51–56.
Nelson, D.E., Ihekwaba, A.E.C., Elliott, M., Johnson, J.R., Gibney, C.A., Foreman, B.E., Nelson, G., See, V., Horton, C.A., Spiller, D.G., et al. (2004). Oscillations in NF-kappaB signaling control the dynamics of gene expression. Science *306*, 704–708.
Oh, H., and Ghosh, S. (2013). NF- j B: roles and regulation in different CD4 + T-cell subsets. 41–51.
Pantazis, P., and Supatto, W. (2014). Advances in whole-embryo imaging: a quantitative transition is underway. Nat. Rev. Mol. Cell Biol. *15*, 327–339.
Paszek, P., Ryan, S., Ashall, L., Sillitoe, K., Harper, C. V, Spiller, D.G., Rand, D. a, and White, M.R.H. (2010). Population robustness arising from cellular heterogeneity. Proc. Natl. Acad. Sci. U. S. A. *107*, 11644–11649.
Pękalski, J., Zuk, P.J., Kochańczyk, M., Junkin, M., Kellogg, R., Tay, S., and Lipniacki, T. (2013). Spontaneous NF-κB activation by autocrine TNFα signaling: A computational analysis. PLoS One *8*.

Petty, M.C., Introduc-, L.F.A., Aca-, F.L.S., Clays, K., Armstrong, N.J., Jr, J.E.F., and Machleder, E.M. (1998). The Biochemical Basis of an All-or-None Cell Fate Switch in Xenopus Oocytes. *280*, 895–899.
Purvis, J.E., and Lahav, G. (2013). Encoding and decoding cellular information through signaling dynamics. Cell *152*, 945–956.
Purvis, J.E., Karhohs, K.W., Mock, C., Batchelor, E., Loewer, A., and Lahav, G. (2012). P53 Dynamics Control Cell Fate. Science *336*, 1440–1444.
Sanchez-Freire, V., Ebert, A.D., Kalisky, T., Quake, S.R., and Wu, J.C. (2012). Microfluidic single-cell real-time PCR for comparative analysis of gene expression patterns. Nat. Protoc. *7*, 829–838.
Santos, S.D.M., Verveer, P.J., and Bastiaens, P.I.H. (2007). Growth factor-induced MAPK network topology shapes Erk response determining PC-12 cell fate. Nat. Cell Biol. *9*, 324–330.
Scha, R., Okuno, T., Hassdorf, R., Shigeto, K., Ono, T., Bode, M., Pietzsch, O., Wiesendanger, R., Getzlaff, M., Wiesendanger, R., et al. (2002). Microfluidic Large-Scale Integration. *4437*.
Selimkhanov, J., Taylor, B., Yao, J., Pilko, A., Albeck, J., Hoffmann, A., Tsimring, L., and Wollman, R. (2014). Systems biology. Accurate information transmission through dynamic biochemical signaling networks. Science *346*, 1370–1373.
Sen, R., and Baltimore, D. (1986). Multiple nuclear factors interact with the immunoglobulin enhancer sequences. Cell *46*, 705–716.
Shah, N. a, and Sarkar, C. a (2011). Robust network topologies for generating switch-like cellular responses. PLoS Comput. Biol. *7*, e1002085.
Shinohara, H., Behar, M., Inoue, K., Hiroshima, M., Yasuda, T., Nagashima, T., Kimura, S., Sanjo, H., Maeda, S., Yumoto, N., et al. (2014). Positive feedback within a kinase signaling complex functions as a switch mechanism for NF-κB activation. Science *344*, 760–764.
Sinha, M.K., Sturis, J., Ohannesian, J., Magosin, S., Caro, F., Stephens, T., Heiman, M.L., and Polonsky, K.S. (1996). Ultradian Oscillations of Leptin Secretion in Humans between midnight and early morning hours and lowest around noon to mid-afternoon . In the. Biochem. Biophys. Res. Commun. *738*, 733–738.
Spiller, D.G., Wood, C.D., Rand, D. a, and White, M.R.H. (2010). Measurement of single-cell dynamics. Nature *465*, 736–745.
Tay, S., Hughey, J.J., Lee, T.K., Lipniacki, T., Quake, S.R., and Covert, M.W. (2010). Single-cell NF-kappaB dynamics reveal digital activation and analogue information processing. Nature *466*, 267–271.
Walker, J.J., Terry, J.R., and Lightman, S.L. (2010). Origin of ultradian pulsatility in the hypothalamic-pituitary-adrenal axis. Proc. Biol. Sci. *277*, 1627–1633.
Warmflash, A., Zhang, Q., Sorre, B., Vonica, A., Siggia, E.D., and Brivanlou, A.H. (2012). Dynamics of TGF-β signaling reveal adaptive and pulsatile behaviors reflected in the nuclear localization of transcription factor Smad4. Proc. Natl. Acad. Sci. U. S. A. *109*, E1947–E1956.
Warren, L., Bryder, D., Weissman, I.L., and Quake, S.R. (2006). Transcription factor profiling in individual hematopoietic progenitors by digital RT-PCR. Proc. Natl. Acad. Sci. U. S. A. *103*, 17807–17812.
Wee, K.B., Yio, W.K., Surana, U., and Chiam, K.H. (2012a). Transcription factor oscillations induce differential gene expressions. Biophys. J. *102*, 2413–2423.
Wee, K.B., Yio, W.K., Surana, U., and Chiam, K.H. (2012b). Transcription factor oscillations induce differential gene expressions. Biophys. J. *102*, 2413–2423.
Werner, S.L., Barken, D., and Hoffmann, A. (2005). Stimulus specificity of gene expression programs determined by temporal control of IKK activity. Science *309*, 1857–1861.
Whitesides, G.M. (2006). The origins and the future of microfluidics. Nature *442*, 368–373.
Wu, H. (2013). Essay Higher-Order Assemblies in a New Paradigm of Signal Transduction. 287–292.
Yang, H., Wang, H., Shivalila, C.S., Cheng, A.W., Shi, L., and Jaenisch, R. (2013). Resource One-Step Generation of Mice Carrying Reporter and Conditional Alleles by CRISPR / Cas-Mediated Genome Engineering. Cell *154*, 1370–1379.
Yin, Q., Lin, S.-C., Lamothe, B., Lu, M., Lo, Y.-C., Hura, G., Zheng, L., Rich, R.L., Campos, A.D., Myszka, D.G., et al. (2009). E2 interaction and dimerization in the crystal structure of TRAF6. Nat. Struct. Mol. Biol. *16*, 658–666.

Yissachar, N., Fischler, T.S., Cohen, A.A., Reich-zeliger, S., Russ, D., Shifrut, E., and Porat, Z. (2013). Short Article Dynamic Response Diversity of NFAT Isoforms in Individual Living Cells. Mol. Cell *49*, 322–330.
Zambrano, S., Bianchi, M.E., and Agresti, A. (2014). High-throughput analysis of NF-κB dynamics in single cells reveals basal nuclear localization of NF-κB and spontaneous activation of oscillations. PLoS One *9*, e90104.
Zanoni, I., Ostuni, R., Marek, L.R., Barresi, S., Barbalat, R., Barton, G.M., Granucci, F., and Kagan, J.C. (2011). CD14 Controls the LPS-Induced Endocytosis of Toll-like Receptor 4. Cell *147*, 868–880.

Materials and methods

Cell lines

We used p65-knockout 3T3 fibroblasts (courtesy Markus Covert) modified using lentiviral vectors to express p65-DsRed under its endogenous promoter along with an H2B-GFP nuclear reporter, as described previously (Lee et al., 2009). The cell line was clonally derived to express at p65-DsRed at lowest detectable level to preserve near endogenous expression.

Automated microfluidic cell culture system

Automated microfluidic cell culture was performed as previously described (Kellogg et al., 2014; Tay et al., 2010, Gomez-Sjoberg). Briefly, microfluidic chambers were fibronectin treated and seeded with cells at approximately 200 cells/chamber. Cells were allowed to grow for one day with periodic media replenishment until 80% confluence. To stimulate cells, media equilibrated to 5% CO2 and containing the desired LPS amount was delivered to chambers, leading to a step increase in LPS concentration. All LPS doses were tested in parallel in a single chip. Following stimulation, chambers were sealed and imaged at 5-6 minute intervals.

Image acquisition and data analysis

DsRed and GFP channels were acquired using a Leica DMI6000B microscope at 20x magnification with a Retiga-SRV CCD camera (QImaging). One or two images were acquired per chamber and stitched if required using ImageJ (Pairwise stitching plugin). CellProfiler software (www.cellprofiler.org) and custom Matlab software was used to automatically track cells and quantify NF-κB translocation, and automated results were manually compared with images to ensure accuracy prior to further analysis. Mitotic cells were excluded from analysis. NF-κB activation was quantified as mean nuclear fluorescence intensity normalized by mean cytoplasm intensity. Area of the first peak was integrated after baseline correction from the time of LPS stimulation to the first minimum for each cell using Matlab function *trapz*. For peak analysis data was smoothed (Matlab functions smooth) followed by peak detection (Matlab function *mspeaks*) to extract NF-κB peak properties (intensity, area, delay) with manual verification using a custom interface in Matlab.

Gene Expression

Cells were seeded at 10000 cells/well in a 96-well plate and left to attach overnight before stimulation with LPS (1 – 500 ng/ml). Cells were then lysed, the RNA reverse-transcribed and cDNA pre-amplified (specific target amplification with the set of 24 primers) using the One-Step RT-PCR kit from Invitrogen.

Quantitative PCR was carried out on 48.48 dynamic arrays from Fluidigm according to manufacturer instructions, and expression was normalized to GAPDH.

4. NOISE FACILITATES TRANSCRIPTIONAL CONTROL UNDER DYNAMIC INPUTS

The contents of the chapter published in Cell: Kellogg, R.A., and Tay, S. (2015). Noise Facilitates Transcriptional Control under Dynamic Inputs. Cell 160, 381–392. doi:10.1016/j.cell.2015.01.013

Ryan A. Kellogg[1], Savaş Tay[1*]

1. Department of Biosystems Science and Engineering, ETH Zürich, Switzerland 4058.

* Correspondence: savas.tay@bsse.ethz.ch

R.A.K. performed frequency-modulated TNF microfluidic experiments, simulations based on existing NF-κB model, analyzed experimental and simulation results, prepared figures, and wrote the manuscript.

SUMMARY

Cells must respond sensitively to time-varying inputs in complex signaling environments. To understand how signaling networks process dynamic inputs into gene expression outputs and the role of noise in cellular information processing, we studied the immune pathway NF-κB under periodic cytokine inputs using microfluidic single-cell measurements and stochastic modeling. We find that NF-κB dynamics in fibroblasts synchronize with oscillating TNF signal and become entrained, leading to significantly increased NF-κB oscillation amplitude and mRNA output compared to non-entrained response. Simulations show that intrinsic biochemical noise in individual cells improves NF-κB oscillation and entrainment whereas cell-to-cell variability in NF-κB natural frequency creates population robustness, together enabling entrainment over a wider range of dynamic inputs. This wide range is confirmed by experiments where entrained cells were measured under all input periods. These results indicate that synergy between oscillation and noise allows cells to achieve efficient gene expression in dynamically changing signaling environments.

INTRODUCTION

Understanding how cells efficiently process information in rapidly changing and noisy environments is a fundamental problem in biology. Cells experience environments that fluctuate over time during physiological conditions such as inflammation, where oscillating input signals can occur due to pulsatile secretion of signaling molecules from immune cells, (Goldbeter et al., 1990; Han et al., 2012), propagating signaling waves (Falcke, 2003; Schutze et al., 2011; Yde et al., 2011), or by coupling between upstream pathways (Gerard and Goldbeter, 2012; Goldbeter and Pourquie, 2008; Yang et al., 2010; Yoshiura et al., 2007). How cells process such dynamic inputs into functional gene expression outputs is not well understood. Further, signaling systems are subject to biochemical noise originating from stochastic molecular interactions, leading to system noise and cell-to-cell variability in response to

input signals. While it is common belief that noise is harmful to information processing (Cheong et al., 2011), cell signaling pathways perform with remarkable robustness despite ever-present system noise and variability (Little et al., 1999). It is not clear how cell-signaling pathways overcome system noise and whether there are functional roles for noise in cellular information processing.

Signaling systems often employ oscillatory network architecture to process environmental inputs (Levine et al., 2013). For example, specific transcriptional responses can be achieved by encoding the dose or identity of a constant input signal by modulating oscillatory response dynamics (Kupzig et al., 2005). Theoretically, oscillation can be advantageous also in the processing of fluctuating and noisy input signals. For example, dynamic inputs that contain noise can be transmitted efficiently in an oscillating system through a phenomenon called stochastic resonance (Douglass et al., 1993), previously observed in neuronal circuits (McDonnell and Ward, 2011). Nevertheless, such a beneficial role for biochemical system noise in the processing of fluctuating environmental signals has not been shown.

To study how oscillation and system noise may interact in processing of dynamic input signals we consider the NF-κB system, a gene regulatory network central to immune functions and many diseases including autoimmunity and cancer (Hayden and Ghosh, 2008). NF-κB pathway activation by TNF cytokine leads to oscillations in p65:p50 heterodimer localization between the cytoplasm and nucleus (Hayden and Ghosh, 2008; Hoffmann et al., 2002; Nelson et al., 2004), mediated by NF-κB dependent induction of negative feedback genes of the IκB family (Fig. 1A). Pathway activation through IKK under TNF occurs in a digital, switch-like fashion (Tay et al., 2010).

NF-κB oscillations are subject to intrinsic and extrinsic noise, leading to variable timing between cells that obscures single-cell behavior in population analyses (Swain et al., 2002; Tay et al., 2010). Sources of extrinsic noise include different signaling histories and uneven cell division leading to variation in protein abundance (Huh and Paulsson, 2011). Variation in TNF receptor or NF-κB molecules create different response characteristics between cells (Tay et al., 2010). Significant contributions to intrinsic (biochemical) noise in NF-κB include burst-like transcription of IκB and A20 negative feedback genes, and receptor-ligand interaction at low ligand concentration (Elowitz et al., 2002; Tay et al., 2010). Another negative feedback gene IκBϵ is induced with a 45 min delay compared to IκBα, which is optimally timed for increasing cell-to-cell oscillation variability, suggesting that transcriptional noise might provide a functional advantage (Ashall et al., 2009; Paszek et al., 2010).

The function of NF-κB oscillation is not fully understood. Other pathways like p53 and Notch convert between oscillatory and non-oscillatory response to achieve specific cell fate responses (Dolmetsch et al., 1998; Kageyama et al., 2008; Purvis et al., 2012; Purvis and Lahav, 2013). The frequency of oscillation in ERK, Crz1, and NFAT4 is altered depending on input signal concentration, achieving expression control across diverse promoters through frequency modulation (Albeck et al., 2013; Berridge et al., 2003; Cai et al., 2008; Dolmetsch et al., 1998; Eldar and Elowitz, 2010; Shankaran et al., 2009; Yissachar et al., 2013). However, NF-κB oscillation frequency (90 to 100 min peak-to-peak interval) is unchanged across a wide range of input concentrations (Longo et al., 2013; Tay et al., 2010; Turner et al., 2010), and it is uncertain how NF-κB oscillation changes and directs gene expression in response to a fluctuating input.

Oscillatory systems can experience resonance, where a periodic stimulus leads to amplified output (Abraham et al., 2010; Pikovsky et al., 2003). Periodic input may also entrain or synchronize a

population of oscillators so that all oscillators adopt the same frequency and phase. Entrainment leading to resonant amplification of NF-κB oscillations may occur for input signals that fluctuate at a rate similar to the NF-κB natural frequency, increasing the sensitivity of the NF-κB system especially to small signals. Theoretical studies predict that periodic input to NF-κB may generate entrainment, quasiperiodic oscillations, or even chaos (Jensen and Krishna, 2012; Wang et al., 2011). Entrainment, with prominent examples from circadian rhythms and brain waves, allows oscillatory signaling and transcriptional pathways to synchronize and work in harmony (Reppert and Weaver, 2002; Varela et al., 2001). It is conceivable that entrainment could reduce cell-to-cell NF-κB oscillation variability, leading to homogenous transcriptional responses at the population level. Nevertheless, experimental studies are lacking on whether NF-κB can experience resonance and entrainment, and whether there is impact on gene expression output and variability (Longo et al., 2013; Tay et al., 2010; Turner et al., 2010).

Although noise is detrimental to signal transmission in linear systems, it can facilitate information transfer in a nonlinear system by decreasing the amplitude of a periodic input needed to achieve coupling (Collins et al., 1996; Lindner et al., 2004; Mori and Kai, 2002; Zhou et al., 2002). For example, input noise can facilitate sensory neuron processing (McDonnell et al., 2011) and intrinsic noise may cause oscillations to become more robust to perturbation (Paszek et al., 2010; Perc and Marhl, 2003; Vilar et al., 2002). Extrinsic noise (i.e. variation in signaling parameters between cells) may also impact entrainment due to increased population diversity, similar to bacterial bet hedging when external conditions change (Mondragon-Palomino et al., 2011; Suel et al., 2006; Wakamoto et al., 2013). However, it is not known how noise could affect entrainment of a complex and physiological mammalian system such as NF-κB.

To probe how oscillation and noise together determine NF-κB dependent transcription in dynamic settings, we used a microfluidics-based experimental pipeline that enabled automated cell stimulation, live imaging, and gene expression measurements (Gómez-Sjöberg et al., 2007; Junkin and Tay, 2014; Kellogg et al., 2014; Tay et al., 2010). We delivered various TNF cytokine inputs to p65-/- mouse 3T3 fibroblast cells expressing p65/DsRed fusion protein at near wild-type levels (Lee et al., 2008; Tay et al., 2010) (Fig 1B, 2A and 3A). The microfluidic chip utilizes computer controlled PDMS membrane valves, allowing constant perfusion or periodic pulsing of signaling factors. 96 independent cell culture experiments each with complex fluidic conditions can be maintained in parallel. Cell images acquired at 5 min intervals were automatically analyzed, extracting thousands of single-cell trajectories of NF-κB nuclear intensity over time (Kellogg et al., 2014). Following periodic TNF stimulation, cells were retrieved for gene expression analysis in a high-throughput microfluidic qPCR system to understand the influence of entrainment on target gene expression (Kellogg et al., 2014). Furthermore, we performed stochastic simulations using an established model of NF-κB (Tay et al., 2010), and varied both intrinsic and extrinsic noise to interpret our experimental findings and understand the role of noise and oscillations for NF-κB dynamic signal processing.

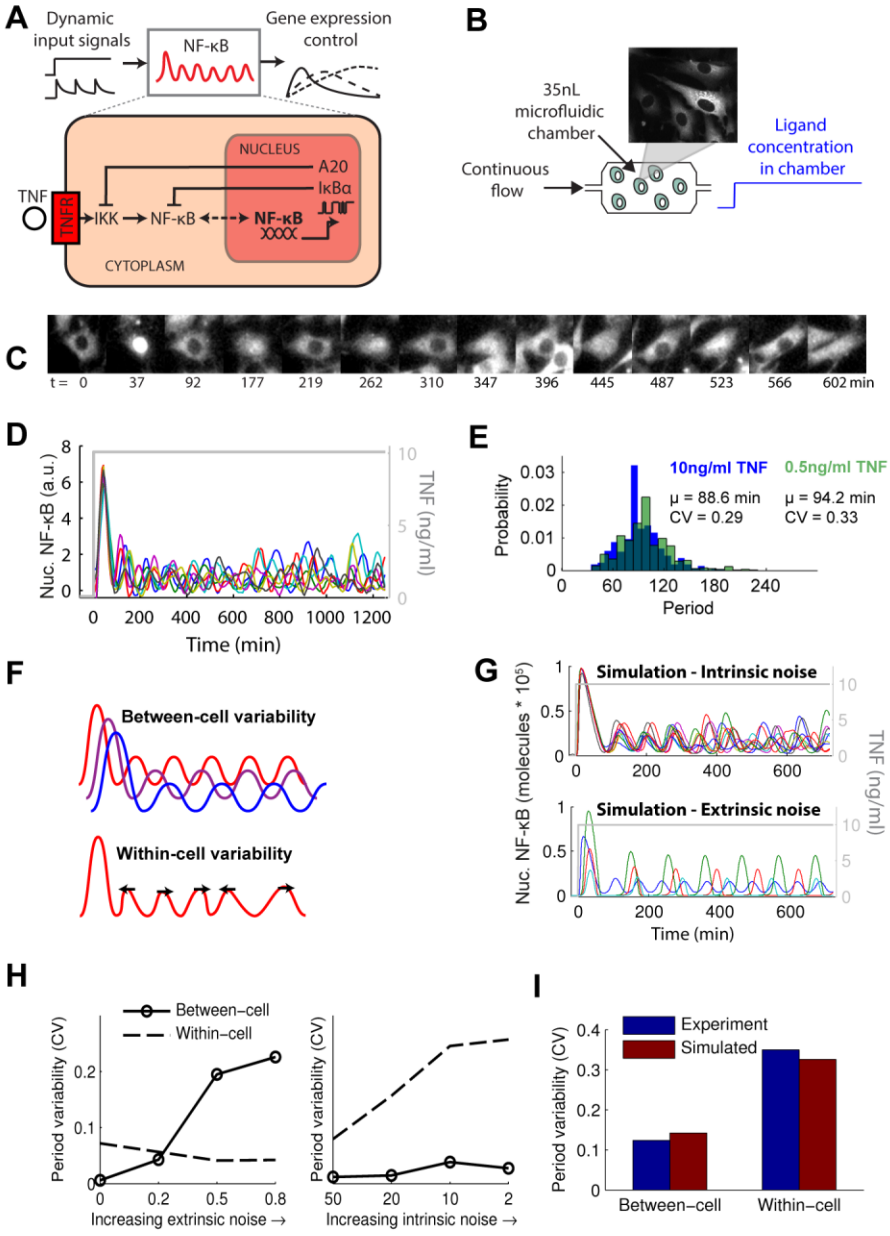

Figure 1. Noise origins of sustained NF-κB oscillation and heterogeneity

A) NF-κB transcription factor oscillates between cytoplasm and nucleus in response to inflammatory signals. NF-κB dynamics relay external signals to gene expression outputs. B) We deliver continuous or periodic inputs to cells using microfluidic cell culture. In continuous mode, TNF is flowed over cells to maintain constant concentration. C) We record single-cell NF-κB translocation using live cell microscopy. Images show nucleus-cytoplasm oscillations in NF-κB (p65-dsRed) under continuous TNF perfusion. (Scale bar: 10μm) D) Under constant 10ng/ml TNF concentration, NF-κB shows long sustaining, asynchronous oscillations. E) NF-κB oscillates with mean period ~90 min under constant high and low dose input (n = 40 cells). F) Pictorial depiction of within- and between-cell oscillation variability. While cells may have different mean periods (between-cell variability), each cell also exhibits fluctuation in its own oscillation (within-cell variability). G) Simulations with parameter settings from show that extrinsic noise increases

between-cell variability, and intrinsic noise increases within-cell variability. H) In simulations increasing extrinsic noise increases between-cell variability, while increasing intrinsic noise increases within-cell variability. I) Experimentally, we observe ~12% period fluctuation between different cells and 34% within the same cells under 10ng/ml TNF. Variability in simulated traces agrees with experimentally measured values. Intrinsic noise results from discrete regulation of gene activity. To affect transcriptional intrinsic noise, we increased gene copy number and proportionally decreased rate of IκB and A20 synthesis, and to increase extrinsic noise we increased variance of the log-normal distribution from which NF-κB and TNFR number are drawn with each model simulation (Extended Experimental Procedures). All other model parameters were unchanged from the previously published TNF NF-κB model (Tay et al., 2010).

RESULTS

Constant TNF stimulation generates sustained, noisy NF-κB oscillations

Previous studies of NF-κB dynamics were subject to TNF ligand loss due to degradation and cellular internalization, leading to damped oscillations (Tay et al., 2010). Here, constant TNF concentration was achieved by perfusion of fresh TNF-containing media using an on-chip peristaltic pump (Fig. 1B). Under constant TNF concentration, we observed NF-κB oscillations sustaining longer than 24 hours with mean period approximately 90 min (Fig. 1C-D and movie S1). Cells exhibited different natural frequencies (between-cell variability) and cycle-to-cycle timing fluctuation (within-cell variability) (Fig. 1F). NF-κB oscillation is robust to changes in dose, and lowered dose, which generates high receptor-ligand noise, modestly lengthened the average period and increased period variability (CV: coefficient of variation, in Fig. 1E). These findings show that NF-κB oscillation sustains under constant TNF input, pointing to a conserved function for oscillations.

To understand how noise underlies oscillation variability, we performed simulations of NF-κB dynamics under constant TNF concentration. We used a stochastic single-cell model, which faithfully reproduces the NF-κB dynamics in single 3T3 fibroblast cells used in this study (Tay et al., 2010). To affect transcriptional intrinsic noise, we increased gene copy number and proportionally decreased rate of IκB and A20 synthesis, and to increase extrinsic noise we increased variance of the log-normal distribution from which NF-κB and TNFR number are drawn with each model simulation (Extended Experimental Procedures). All other model parameters were unchanged from the previously published TNF NF-κB model (Tay et al., 2010). The simulations showed sustained oscillation and period characteristics similar to our experiments (Fig. 1G) (Lipniacki et al., 2004; Lipniacki et al., 2007; Tay et al., 2010). Varying intrinsic noise in the model associated with changes in cycle-to-cycle variability, while changing extrinsic noise affected variability in average (natural) oscillation period between cells (Fig. 1G-H). Magnitudes of variability for simulations matched that of experimental measurements, supporting an appropriate balance between intrinsic and extrinsic noise in the model (Fig. 1I).

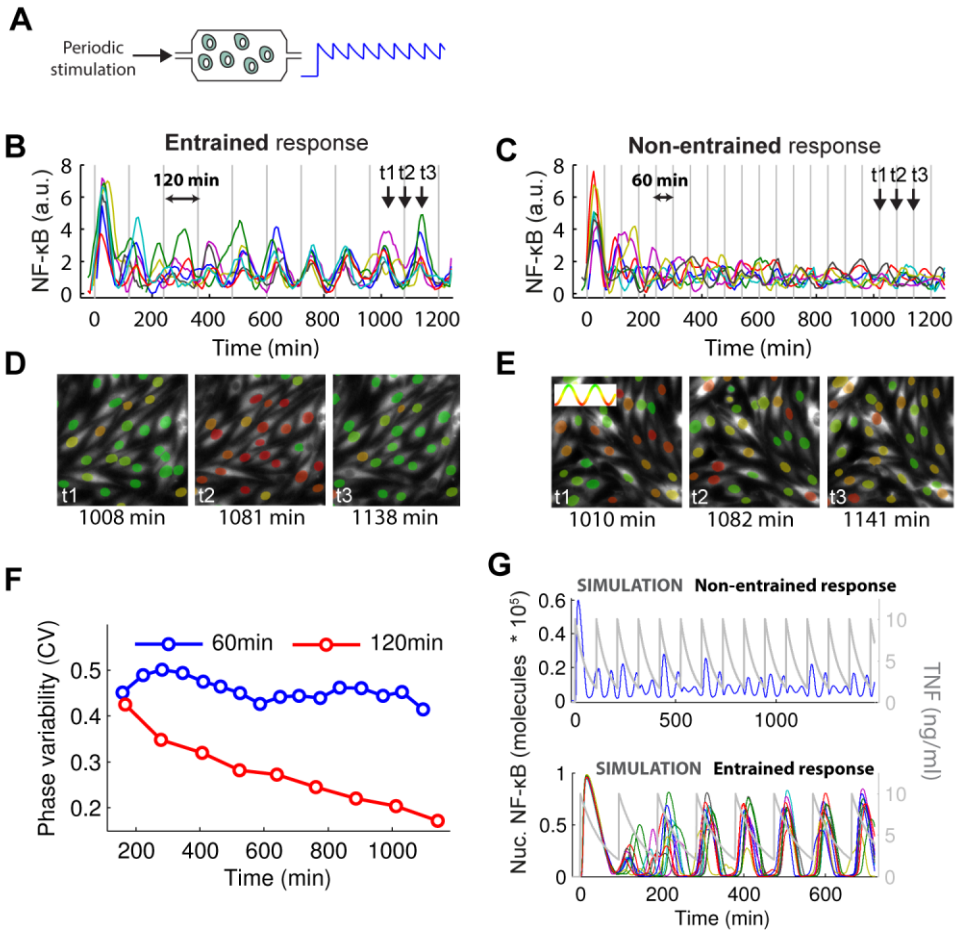

Figure 2. Periodic TNF stimulation can entrain or disrupt NF-κB oscillations

A) We deliver periodic inputs to cells using a microfluidic cell culture chip. In periodic mode, TNF is replaced at specified intervals, and ligand decay (due to cell uptake and degradation) leads to a periodic sawtooth concentration profile. B) Single-cell traces for stimulation at 120 min input period, which entrains and synchronizes NF-κB oscillations. C) Single-cell NF-κB trajectories measured for stimulation at 60 min input, which disrupts NF-κB oscillations. D) Image time-series for 120 min periodic input for times t1-t3 indicated by arrows in B. The entrained cell population oscillates synchronously. Inset: Nucleus color indicates nuclear NF-κB intensity from red (low) to green (high). (Scale bar: 25μm) E) Image time-series for 60 min periodic input for times t1-t3 indicated by arrows in B. The cell population does not synchronize. F) Phase variability for 60 min stimulation remains constant over time. In contrast, during 120 min stimulation (red), phase variability decreases as the cell population synchronizes over time. G) Simulations reproduce non-entrained and entrained responses. See also Figure S1.

Single-cell NF-κB dynamics becomes entrained under an oscillating cytokine signal

During inflammation cells operate under dynamic TNF signals, which may interfere with NF-κB oscillations needed for processing of input dose information and differential gene expression (Tay et al.,

2010). Depending on frequency and amplitude, periodic input to an oscillator like NF-κB can either entrain or disrupt the oscillation. Entrainment describes when the oscillator becomes phase-locked and synchronized with the driving stimuli (Pikovsky et al., 2003), with prominent examples in biology from circadian rhythms (Leloup and Goldbeter, 2003; Reppert and Weaver, 2002) and brain waves, to synthetic bacterial oscillators (Mondragon-Palomino et al., 2011). On the other hand, when entrainment cannot occur due a significant frequency mismatch between the oscillator and input signal, the result is a disrupted oscillation that is quasiperiodic or even chaotic (Jensen and Krishna, 2012; Pikovsky et al., 2003). How NF-κB responds to sustained periodic inputs that could entrain NF-κB oscillations has not been experimentally investigated so far.

To test the entrainment capacity of NF-κB and how oscillation contributes to gene expression control under fluctuating cytokine signals, we applied TNF inputs to fibroblasts using two stimulation periods (Fig. 2A): In the first case, TNF stimulus is applied every 120 minutes, which indeed efficiently entrained NF-κB after a transient (Fig. 2B). In the second case, TNF stimulus was provided every 60 minutes, which was sufficiently mismatched from the ~90 min NF-κB natural period to induce a disrupted, non-entrained NF-κB response in most cells (Fig. 2C). Movies S2-S4 show single-cells under these inputs as well as under 90 min input, and Supplementary Figure S1 shows the difference between entrained cells and cells oscillating under constant TNF signal. Images selected at three timepoints show that for 60 min input NF-κB oscillations remain asynchronous in the population, and for 120 min input NF-κB oscillates synchronously across cells (Fig. 2D-E, also see and supplementary movies S2-S4). Population phase variability, a measure of synchrony, remains high during the timecourse with 60 min stimulation, but it quickly reduces during 120 min stimulation as the population entrains (Fig. 2F, and S1C). Simulations with our comprehensive NF-κB model also reproduced non-entrained and entrained responses under similar inputs (Fig. 2G).

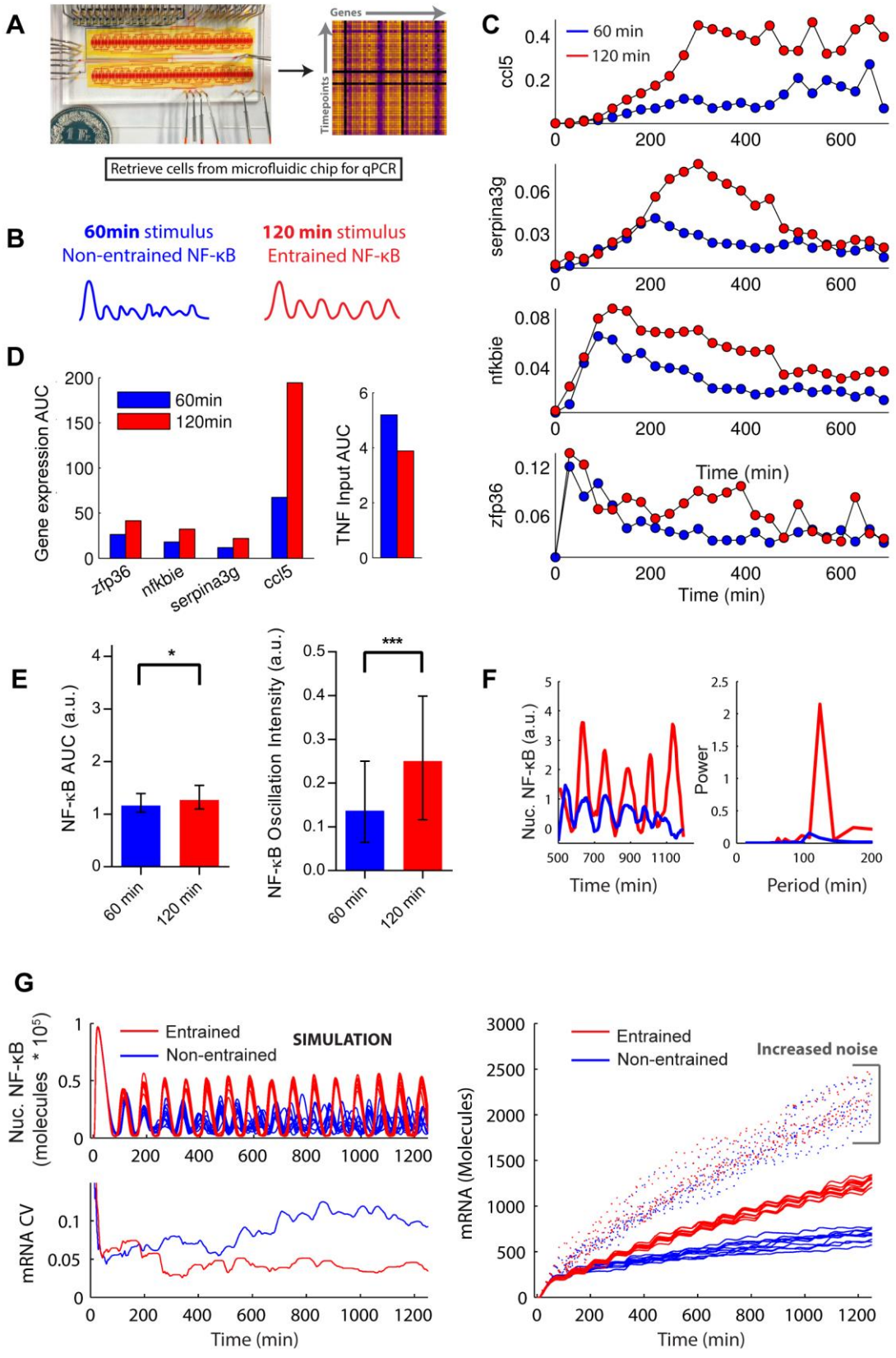
A
Genes
Timepoints
Retrieve cells from microfluidic chip for qPCR
B
60min stimulus
Non-entrained NF-κB
120 min stimulus
Entrained NF-κB
C
60 min
120 min
ccl5
serpina3g
nfkbie
zfp36
Time (min)
D
Gene expression AUC
60min
120min
zfp36
nfkbie
serpina3g
ccl5
TNF Input AUC
E
NF-κB AUC (a.u.)
NF-κB Oscillation Intensity (a.u.)
60 min
120 min
F
Nuc. NF-κB (a.u.)
Time (min)
Power
Period (min)
G
Nuc. NF-κB (molecules * 10^5)
Entrained
Non-entrained
SIMULATION
mRNA CV
Time (min)
mRNA (Molecules)
Increased noise

Figure 3. Entrained NF-κB oscillations improve transcriptional efficiency

A) Cells are cultured and provided periodic stimulation on chip and harvested for qPCR analysis. B) TNF stimulation with 60 min period (blue) leads to non-entrained NF-κB response, and most individual cells do not synchronize with the input. C) NF-κB regulated gene expression under non-entrained (60 min stimulation) and entrained (120 min stimulation). Higher transcriptional output is seen when NF-κB oscillations are entrained. Enhanced transcription occurs consistently for early, middle, and late genes. The effect is most pronounced for late responding genes (i.e. ccl5). D) Gene expression output measured by area under curve (AUC). AUC is higher for entrained compared to non-entrained NF-κB response. Although 120 min stimulation increases transcript production, it is not due to higher TNF exposure, which is lower compared to 60 min stimulation. E) Analysis of single cell NF-κB trajectories shows modest increase in response area ($p = 0.04$) and strong increase in oscillation energy ($p = 0.0002$) (bars indicate median +/- interquartile range, p-values by Mann-Whitney test.) F) Example NF-κB trajectories (for later part of timecourse starting at 500 min) and corresponding power spectra for 60 and 120 min input, showing stronger oscillation under entrained (120 min) input. G) Stochastic NF-κB simulation of cells under either entraining or non-entraining input (left) and gene expression output (right). Due to nonlinear binding of NF-κB to DNA, stronger oscillation under entraining input creates increased gene expression output, in agreement with experiments. Increasing intrinsic noise amplifies oscillations and leads to even higher transcription output. mRNA cell-to-cell variability (measured by Coefficient of Variation, CV) is lower for entrained cells, indicating that entrainment reduces cell-to-cell mRNA variability compared to non-entrained cells. See also Figure S2 and S3.

Entrained NF-κB oscillation improves gene expression efficiency and reduces cell-to-cell variability

NF-κB regulates hundreds of pro and anti-inflammatory genes (Hao and Baltimore, 2013). To understand the influence of entrained vs. disorderly NF-κB dynamics in gene expression, we measured time-dependent expression of target genes for 120 min and 60 min periodic TNF stimulation using microfluidic qPCR (Fig. 3A-B, S2, and S3). Cells stimulated in independent chambers of the cell culture chip were harvested for expression analysis at 30 minute time increments (Fig 3A) (See protocols in (Kellogg et al., 2014)). Under the entraining 120 min input, gene expression output is notably enhanced, especially in genes with later induction times (Fig. 3C, red lines). In contrast, 60 min input that leads to non-entrained NF-κB response caused an impaired transcriptional response (Fig. 3C, blue lines). Importantly, the difference in measured mRNA expression is not due to a difference in total TNF exposure, as there is greater TNF exposure for 60 minute input (Fig. 3D).

We analyzed single-cell NF-κB trajectories for entrained and non-entrained conditions to identify what might give rise to the observed gene expression difference. Since differences are most evident in the later part of the timecourse, we focused our analysis to time after 500 min. We measured NF-κB area under the curve (AUC) and determined the extent that each trace is oscillatory vs. non-oscillatory by power spectral analysis. The AUC is a measure of total NF-κB protein localization into the nucleus, which did not change in a significant way to explain the observed gene expression difference. Entrained compared to non-entrained cells showed only 9% increase in NF-κB area. However, we measured 83% increase in NF-κB oscillatory energy (Fig. 3E). Non-entraining input at 60 min mostly resulted in non-oscillatory localization profiles, while entraining input at 120 min resulted in strong oscillations with large amplitude (Fig. 3F).

To understand how increased oscillation magnitude under entraining input could lead to higher transcriptional output, we simulated traces for 60 and 120 min sawtooth input, similar to those used in experiments. Simulated NF-κB single-cells exhibited similar changes in area and oscillatory energy for entrained vs. non-entrained conditions (Fig. 3G and S2). However, the existing transcriptional model, which assumed that NF-κB binding to DNA increases linearly with nuclear NF-κB concentration (Tay et al., 2010), did not reproduce increased gene expression for the entrained condition (Fig. S2). Experiments indicate that NF-κB binds DNA cooperatively with Hill coefficient ~4 (Phelps et al., 2000) (Fig. S2A). Introducing this nonlinearity in our model created significantly increased transcriptional output for entrained versus non-entrained conditions, in agreement with our experiments (Fig. 3G and S2C) (Wee et al., 2012). Increasing intrinsic noise led to stronger oscillations and further amplified the NF-κB induced gene expression (Fig. 3G). Thus, entraining input leads to strengthening of NF-κB oscillations, which are further amplified by noise to drive increased transcriptional output.

We asked whether entrainment could reduce cell-to-cell variability in transcriptional output in our simulations. Comparing the coefficient of variation of mRNA output over time indicates that cell-to-cell transcription variability is significantly reduced under entraining input (Fig. 3G). This result is consistent across simulated early, middle, and late-response genes (Fig. S3). With reduced mRNA variability between individual cells, oscillations appear even in the population averaged experimental timecourse, especially in late genes (Fig. 3C). Therefore, through entrainment that reduces gene regulatory and gene expression variability between cells, one may increase response homogeneity of a cell population.

These results reveal the important role for NF-κB oscillations in generating efficient transcription, and indicate that periodic signaling inputs can amplify transcriptional outputs by resonantly stimulating oscillatory pathways like NF-κB, with a beneficial role for intrinsic noise in further improving the transcriptional output. Moreover, simulations and experiments show reduced cell-cell variability in mRNA level for entraining input. Therefore entrainment provides a way to increase both expression output and homogeneity of a cell population.

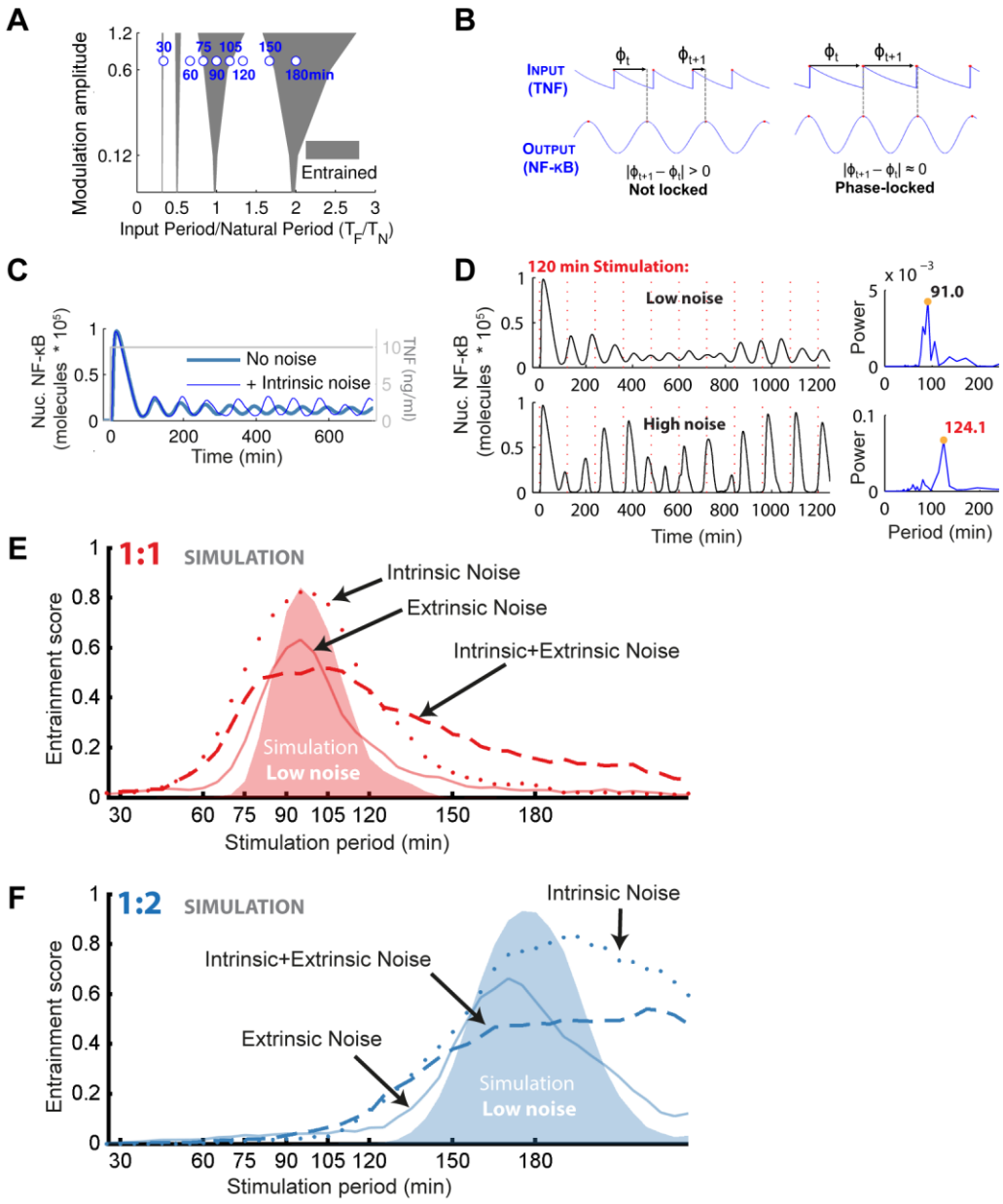

Figure 4. Stochastic modeling predicts entrainment to be robust and that noise underlies enhancement in oscillation and entrainment range

A) Deterministic Arnold tongues (grey shaded regions) computed for decay-type TNF input show that entrainment is readily achieved in narrow regions around 90 min and 180 min (TF/TN = 1, 2) periodic stimulation (10ng/ml TNF). Entrainment is also possible for 30 and 45 min input (TF/TN = 1/3, 1/2). Locations of experimentally tested values are indicated by blue circles. B) Input-output phase relationship and phase-locking. Phase between TNF input and NF-κB output is calculated as the distance from each NF-κB peak to the start of the previous TNF cycle, normalized by the input period. When phase change between cycles is less than a threshold ($|\phi t+1 - \phi t| < 0.15$), input and output are considered phase-locked. Locking can occur at 1:1 ratio (one input cycle for one output cycle), or other ratios such as 1:2 (one input cycle for two output cycles). C) Adding intrinsic noise amplifies and sustains NF-κB oscillations in the model under constant TNF input (example single

cell traces are shown). D) Comparison of entrainment in simulated NF-κB trajectories under low and high intrinsic noise. Under 120 min periodic TNF stimulation, high noise leads to an entrained response indicated by 120 min peak in the power spectrum. In contrast, the response under low noise is not entrained as seen in the power spectrum that shows weaker oscillations and only at the natural period. E-F) Entrainment simulation: Under low-noise simulation (extrinsic noise off, intrinsic noise reduced), entrainment occurs for narrow regions around 90 min stimulation period (1:1 entrainment, panel E) and around 180 min period (1:2 entrainment, panel F). Increasing intrinsic noise in the model broadens regions of entrainment (dotted line). Extrinsic noise alone also increases entrainment range for the population. Adding both extrinsic and intrinsic noise further expands entrainment. See also Figure S4.

Stochastic modeling shows noise-enhanced NF-κB oscillation and entrainment

We next turned to simulations to evaluate the robustness of NF-κB entrainment to changes in the TNF input period and the influence of noise. Using the deterministic implementation of our model, we simulated periodic TNF stimulation of NF-κB in single cells and calculated entrainment ranges. In the space spanned by input modulation amplitude and period (TF), entrainment occurs in triangular regions called Arnold Tongues (Fig. 4A) (Erzberger et al., 2013; Jensen and Krishna, 2012). On the edges of Arnold Tongues synchrony between the input and oscillator breaks down leading to quasiperiodic or aperiodic rhythms. Deterministic Arnold tongues for NF-κB indicated entrainment principally when stimulation period is near 1:1 or 1:2 ratio with the natural period and (TF/TN = 1, 2) (Fig. 4A), meaning that entrainment is expected when the stimulation occurs with a period near 90 min or near 180 min under 10ng/ml TNF input.

To understand the role of different noise levels in entrainment, we simulated periodic TNF signals with varied intrinsic and extrinsic noise conditions and quantified NF-κB phase locking by comparing phase of the next cycle $\phi t+1$ to that of the current cycle ϕt. If the phase difference $|\phi t+1 - \phi t|$ is less than a threshold (0.15) then the response was considered locked over that cycle (Fig. 4B). Our hybrid model based on Gillespie algorithm incorporates experimentally verified intrinsic noise in TNF receptor-ligand binding, which is dominant at small TNF doses, and in transcription of IκBα and A20 that constitute the main negative-feedback loops leading to oscillations (Tay et al., 2010). Particularly, transcriptional noise arises form stochastic interaction of NF-κB transcription factors with the two copies of IκBα and A20 genes. We reduced the transcriptional noise by increasing the gene copy number and proportionally reducing gene expression rate per copy to maintain unchanged gene expression and similar NF-κB natural oscillation period between models. With the stochastic model with greatly reduced intrinsic noise, entrainment occurs for narrow regions around 90 and 180 min stimulation under high dose (10 ng/ml) TNF periodic input (Fig. 4E-F), similar to those in the deterministic simulations. Simulations with high intrinsic noise under the same TNF input led to a significant broadening of the entrainment regions (Fig. 4E-F, dotted line). The intrinsic noise level in these simulations was matched to the experimental level in Figure 1. High intrinsic noise in our simulations increased NF-κB oscillation amplitude of single cells and supported sustained oscillations needed for entrainment (Fig. 4C). The power spectrum provides information about entrainment, and degree of entrainment is indicated by the relative amount of spectral power at the input period. Example simulated NF-κB single cell trajectories for 120 min input are seen in Figure 4D, showing significantly increased oscillation and spectral power at the input period for the high noise case. To determine how noise effects depend on TNF dose and modulation level we simulated the same model using computationally efficient stochastic differential

equations, which showed that intrinsic noise improves NF-κB power at input period when the input modulation is smaller (i.e. weaker driving stimuli), as in higher-dose periodic TNF stimulation (Fig. S4).

Extrinsic noise generates cell-to-cell variability in NF-κB natural period (Fig. 1G-H). When the natural period in an individual cell is sufficiently close to the TNF input period, entrainment will occur. Extrinsic noise in the system thus increases the probability that at least a portion of cells in the population will entrain to a given input. When we included extrinsic in addition to intrinsic noise in our simulations, we observed a further broadening of entrainment ranges NF-κB (Fig. 4E-F). Overall, these simulations indicate that extrinsic and intrinsic noise together enable cells to entrain and drive efficient transcriptional responses for a wider range of dynamical inputs.

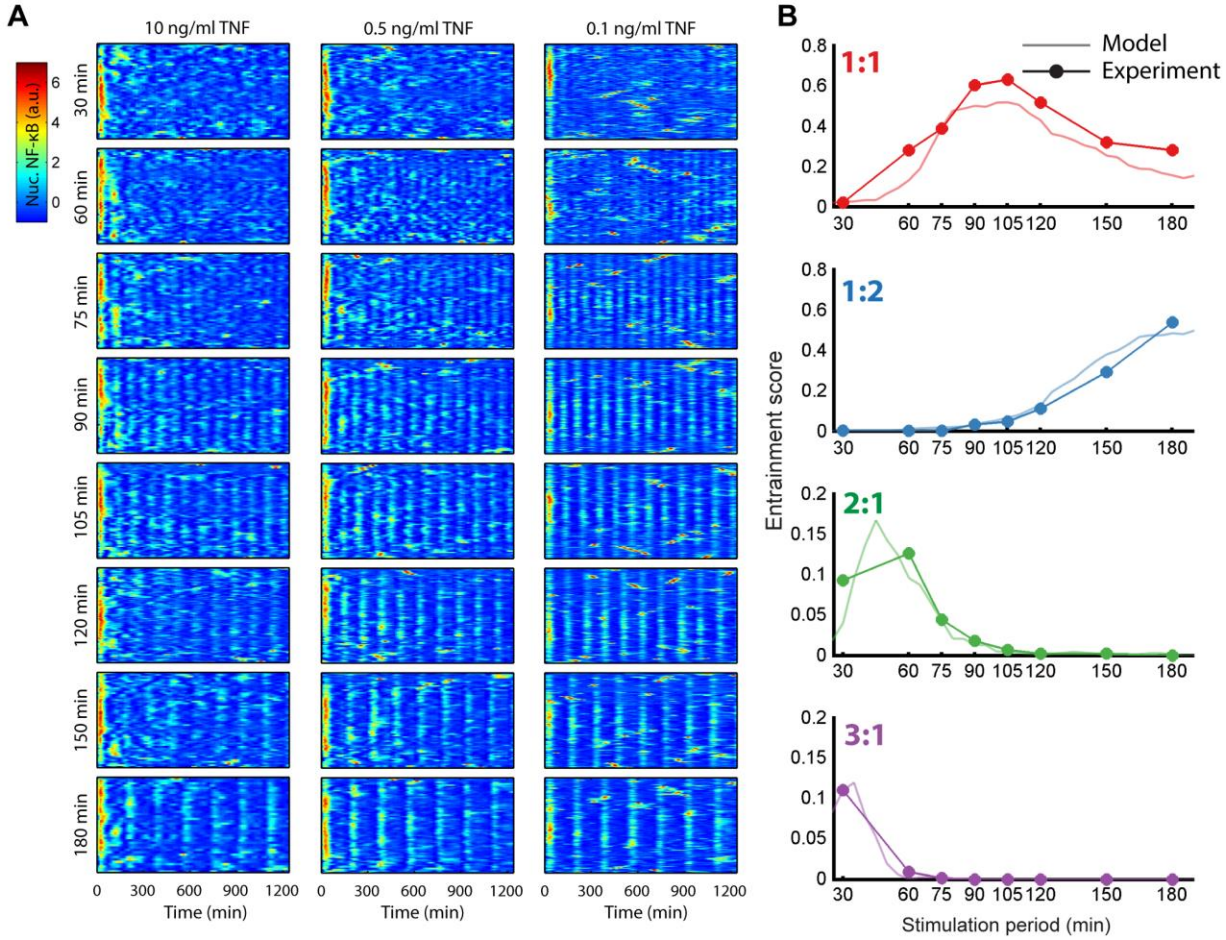

Figure 5. NF-κB entrainment range is wide and agrees with noisy model predictions

A) Heatmaps of single-cell NF-κB trajectories under different doses of TNF (10, 0.5, and 0.1 ng/ml) for stimulation periods ranging from 30 to 180 min. Color indicates NF-κB intensity from low (blue) to high (red). Entrainment of individual cells can be visualized with the appearance of well-aligned peaks. Entrainment and synchronization is pronounced for 90 and 180 min stimulation. Reduced dose leads to greater oscillation synchrony and improved entrainment across all stimulation periods (Fig. S5B). B) Comparison of entrainment scores for 10ng/ml stimulation in various locking modes shows agreement between experiments and noisy model prediction. All

model parameters were unchanged from the previously published TNF NF-κB model (Tay et al., 2010). See also Figure S5.

NF-κB entrainment range is very broad as predicted by noisy simulations

To experimentally test the robustness of NF-κB entrainment to changes in the input, we applied TNF inputs with 30 to 180 minute periods to fibroblasts cultured in separate chambers of the microfluidic system, under 3 different TNF doses of 10, 0.5 and 0.1 ng/ml (Fig. 5 and S5). The dataset contains analysis of approximately 2000 cells over 24hrs duration measured every 5 minutes, creating more than half a million data points (Movies S2-S4). Heatmaps with one row for each single cell NF-κB trajectory show population synchrony that improves with time (Fig. 5A). Periodic stimulation with reduced dose leads to even better entrainment (Fig. 5A). The fraction of NF-κB cycles locking to different entrainment ratios was computed for each stimulation condition, and as anticipated 1:1 locking is maximized when then stimulation period is near 90 min and 1:2 locking is maximized for 180 min stimulation (Fig. 5B). Surprisingly, we observed cells having entrained oscillations in every input period tested, even in those inputs like 120 min that are not predicted by the deterministic or low noise simulations. Good agreement is seen between experimental entrainment values and high-noise model simulations (both under 10 ng/ml TNF dose) incorporating both extrinsic and intrinsic noise and using model parameters published previously (Tay et al., 2010) (Fig. 5B). We did not observe dependence on cell density (Fig. S6).

A consequence of natural period diversity is entrainment heterogeneity, including the ability for different cells in the population to entrain at different ratios. Cells entrained at multiple ratios or did not entrain and exhibited quasiperiodic oscillation (Fig. 6C). Period probability follows a multimodal distribution, indicating simultaneous mixture of for example 1:1 and 1:2 locking responses in the population (Fig. 6A). Simulations incorporating only extrinsic noise also generate mixed locking responses, indicating that locking heterogeneity can arise from extrinsic noise (Fig. 6D).

Period distributions show narrowing with reduced TNF dose, supporting more effective entrainment (Fig. 6B). Comparing mean pairwise Spearman correlation for population responses at each input revealed increased correlation as dose decreases and at larger input periods (Fig. 6E). Therefore, NF-κB is more amenable to entrainment for input level in middle of its dose dynamic range (Tay et al., 2010) in agreement with simulation (Fig. S5C). Entrainment is more efficient under input periods larger than 60min, and frequencies larger than 0.02 min-1 (50 min period) are not observed in the single cell power spectra, indicating that NF-κB system acts like a filter that prevents transmittance of rapid TNF input fluctuations into transcription.

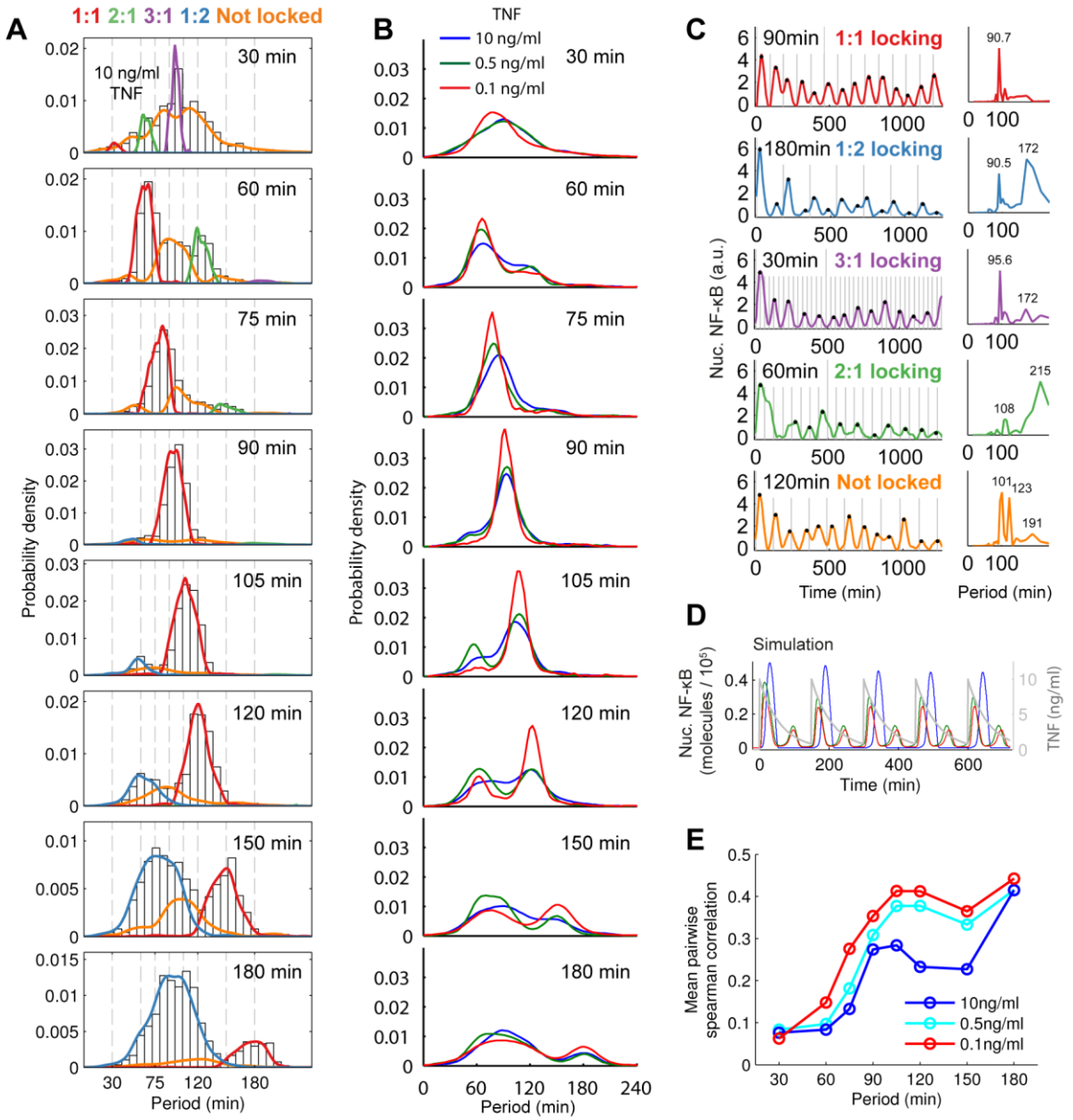

Figure 6. Population heterogeneity and dose dependence of entrainment response

A) Period probability distributions for 10ng/ml TNF input reveal entrainment at multiple ratios between the input and output period. Under 90 min input, the population entrains nearly homogeneously with a 90 min phase-locked oscillation (1:1 ratio, red line). In contrast, during 150 min stimulation cells may respond with a 150 min oscillation (1:1 ratio, red line), or a 75 min oscillation (1:2 ratio, blue line), or without phase-locking (orange line). B) Period distributions for multiple TNF concentrations. Lower concentration leads to period distribution narrowing, indicating improved entrainment and reduced cell-to-cell variability. C) Measured single-cell NF-κB traces for each locking ratio and an example quasiperiodic response (Not locked). D) Simulation with extrinsic noise shows that different locking ratios may occur simultaneously (blue line – 1:1 locking, red and green lines – 1:2 locking). E) Mean pairwise spearman correlation in NF-κB

indicating better population entrainment at lower input concentration and higher input periods. The NF-κB system efficiently filters rapid input fluctuations with periods shorter than 50 minutes. See also Figure S6.

DISCUSSION

Here we provide insight into the function of transcription factor dynamics and noise in gene expression control under fluctuating signaling inputs. Sustained, heterogeneous single-cell NF-κB oscillations synchronize to an oscillating TNF signal in a wide range of stimulation frequencies and become entrained. Entrainment causes amplification of NF-κB oscillations and increased gene expression (Fig. 7). Simulations predict that both intrinsic and extrinsic noise can improve NF-κB entrainment range, allowing cells to respond synchronously to broader range of inflammatory signals (Fig. 4). Single cell measurements confirmed that indeed NF-κB entrainment occurs in the broad range as predicted by stochastic modeling (Fig. 5). While extrinsic noise leads to differences in oscillation frequency between cells creating heterogeneous locking behavior and increases entrainment robustness of the population to changes in input period, a surprising finding is the beneficial role for intrinsic noise in dynamical signaling: Molecular fluctuation arising from low copy number feedback transcripts (IκB and A20) can act to enhance NF-κB oscillation and expand the range of inputs that entrain NF-κB and ultimately enhance target gene expression (Fig. 7). Increased gene expression was explained by incorporating data on nonlinear NF-κB - DNA binding affinity into the model, and we see the greatest differential regulation for late genes such as Ccl5 in agreement with findings that late genes are more sensitive to oscillatory regulation (Ashall et al., 2009; Wee et al., 2012).

Together, our results describe important functions for oscillation and noise in signaling networks. Transcription factor oscillation allows amplified pathway output in response to a periodic stimulus and thus increases system efficiency by reducing the amount of input signal needed to generate strong response. Oscillation moreover allows control of heterogeneity through synchronization of gene regulatory dynamics across the population. By enhancing oscillation and entrainment bandwidth, noise facilitates efficient transcription in dynamic signaling contexts.

Cytokines like TNF activate multiple signaling pathways, and resonant pathway stimulation provides a way to achieve specific responses. A low-dose signal, delivered periodically, could excite NF-κB oscillations and activate NF-κB signaling while avoiding activation of non-oscillatory pathways (such as AP-1). Entrainment with resonance also allows more efficient communication. Indeed, we show that a periodic resonant stimulus achieves greater pathway output while at the same time requiring fewer TNF molecules than a non-entraining stimulus.

Oscillation with resonance may act as a filter. Non-entraining inputs like rapid TNF fluctuations are effectively attenuated at the gene expression level. This may allow NF-κB system to filter out fast cytokine fluctuations that are not physiological (i.e. input noise). While NF-κB exhibits a robust natural period of ~90 min, researchers are finding oscillation in many signaling pathways with differing characteristic frequencies. Therefore the pathway specificity of a pleiotropic factor such as TNF might be tuned by changing the frequency with which it stimulates a cell. Nonetheless it is likely that oscillatory pathways are linked within and between cells more than is currently appreciated (Kupzig et al., 2005), and temporal filtering allows cells to achieve specific responses based on the frequency content of input signals.

NF-κB both responds to and drives cytokine production, and oscillatory cytokine production has been observed in activated single T cells (Han et al., 2012). Entrainment of NF-κB could be a coordination mechanism during infection, by controlling paracrine signals that instruct migration or fate determination of immune cells (Yde et al., 2011). TNF positive feedback in secretory immune cells such as macrophages could improve entrainment at higher cell density, creating a more amplified (and more homogeneous) response (Pekalski et al., 2013). The broad entrainment range of the NF-κB system allows cells to adapt their oscillation frequency and gene expression dynamics to match cytokine fluctuation in the environment.

Our findings suggest a surprising role for noise and oscillation in mammalian signal transduction and transcriptional control (Fig. 7). In dynamic, physiological signaling scenarios oscillations provides cells the ability to decode not only the amplitude but also frequency content of input signals. Inputs occurring near the natural frequency of an oscillatory system are amplified and generate higher gene expression output, while other input frequencies generate an attenuated response. By enhancing oscillation and entrainment at small signal modulation noise may improve the transfer of weaker dynamic signals in the NF-κB system. Entrainment allows efficient cell-cell communication, control of cell-cell heterogeneity, and possibility to selectively activate oscillatory pathways through resonant stimulation. The prevalence of oscillation in signaling networks suggests that cells are well-equipped for processing dynamic signals.

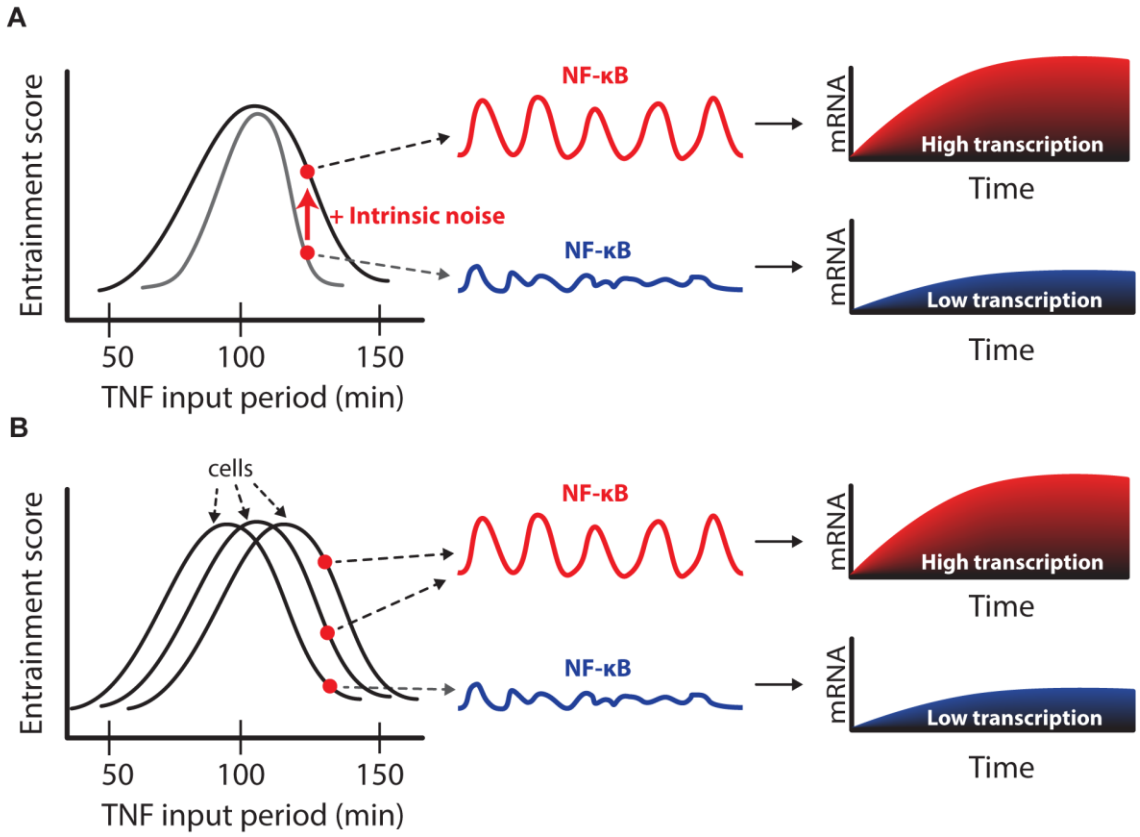

Figure 7. Role of intrinsic and extrinsic noise in NF-κB entrainment and enhanced gene expression

Entrainment score for different inputs shown on the left side; single-cell NF-κB time course shown in the middle; and the corresponding mRNA output is shown on the right. A) Black curve on the left shows the entrainment range of a given cell with intrinsic noise, and grey curve shows the narrower noise-free entrainment range. Signaling inputs at the edge of the entrainment range (red dots) cause non-entrained NF-κB responses and small amplitude (in blue), resulting in impaired gene expression output. Intrinsic noise improves the amplitude and the regularity of NF-κB oscillations (in red), resulting in increased gene expression output. Intrinsic noise can increase entrainment score and also the bandwidth, where cells entrain to a broader range of input periods. B) Extrinsic noise creates cell-to-cell variability in the entrainment range, resulting in a broader entrainment bandwidth for the population. Population variability in entrainment potential ensures that at least some cells will entrain under a given input period.

EXPERIMENTAL PROCEDURES

TNF-α Stimulation using Microfluidic Cell Culture. We use the cell culture chip described previously (Gómez-Sjöberg et al., 2007). Cells were seeded in PDMS chambers coated with fibronectin at constant density ~20,000 cells/cm2 and were cultured overnight prior to stimulation. Standard culture conditions of 5% CO2 and 37° C were maintained using an incubation chamber. Mouse TNF-α (Invitrogen) was diluted in DMEM media in vials pressured with 5% CO2 and kept on ice. Microbore tubing (PEEK, Idex) connected the TNF-α supply to the chip. For continuous pumping input, the on-chip peristaltic pump was operated at a flow rate ~200nL/min. For periodic input, TNF-α containing media was introduced and incubated in the chamber, allowing degradation and internalization of the ligand. The chamber volume is replaced with fresh TNF-α containing media at defined intervals, leading to periodic sawtooth pattern in ligand concentration.

Cell retrieval and gene expression analysis. Cells were loaded into the cell culture chip, and a Matlab program delivered 60min or 120min periodic inputs with start times staggered by 30 minutes to generate time points from 0 to 23.5 hours. Cells in one chamber (approximately 200 cells) were retrieved for each timepoint. At the conclusion of stimulation, cells in all chambers were lysed at once on-chip, and retrieved in a 2ul volume of lysis buffer using an automated routine. Cells exited the chip through ~10cm length microbore tubing positioned into wells of a 96-well plate. Wash steps using PBS prior to retrieval prevented cross-contamination of chambers. cDNA was synthesized using Cells Direct One Step RT-PCR kit (Invitrogen). TaqMan primers and probes (Applied Biosystems) were used for real-time qPCR. Gene expression was assayed using the 48.48 Dynamic Array IFC chip (Fluidigm). Cycle thresholds (CT) were converted to relative expression values normalized to GAPDH (2Ct_gapdh - Ct_gene). Total expression abundance was calculated as the integral of the relative expression (using the Matlab trapz function).

Image Acquisition and Data Processing. The microfluidic chip was mounted on an automated Leica DMI6000B microscope, and fluorescence images (red and green channels for p65 and H2B reporters, respectively) were acquired at 20x magnification via a Retiga-SRV CCD camera (QImaging) every 5-6 minutes for 24-48 hours. CellProfiler software (www.cellprofiler.org) and custom Matlab routines (Gómez-Sjöberg et al., 2007) were used for image processing (available on request). NF-κB activation was quantified as mean nuclear fluorescence intensity after background correction. Area-under-curve provides a measure of total NF-κB activity (Tay et al., 2010) and was quantified as the integral of the NF-κB response (using Matlab trapz). For peak analysis and heatmaps data was smoothed

and standardized (Matlab functions smooth and zscore) followed by peak detection (Matlab mspeaks). Peak-to-peak distances were computed as the difference between peak times (Matlab diff). Cell image overlays aided visualization of oscillation peaks (colored green) and troughs (colored red).

NF-κB Reporter Cell Line. Mouse (3T3) fibroblasts expressing near-endogenous p65 levels were described previously (Tay et al., 2010). Briefly, p65-/- mouse 3T3 fibroblasts were engineered to express p65-DsRed under control of 1.5kb p65 promoter sequence (Lee et al., 2008; Tay et al., 2010). A clone was selected with minimum detectable fluorescence intensity to achieve near-endogenous expression level and NF-κB dynamics similar to wild-type (Lee et al., 2008). Addition of ubiquitin-promoter driven H2B-GFP expression provided a nuclear label to facilitate automated tracking and image processing.

ACKNOWLEDGMENTS

We acknowledge Tomasz Lipniacki, Mustafa Khammash, Benjamin Hepp and Ankit Gupta for discussions on NF-κB and transcription modeling, and Kobi Benenson and Alexander Hoffmann for commenting on the manuscript. S. Tay acknowledges European Union ERC Starting Grant (SingleCellDynamics), Swiss Nationalfonds, SNF SystemsX and NCCR Molecular Systems Engineering for funding support.

REFERENCES

Abraham, U., Granada, A.E., Westermark, P.O., Heine, M., Kramer, A., and Herzel, H. (2010). Coupling governs entrainment range of circadian clocks. Mol Syst Biol 6, 438.

Albeck, J.G., Mills, G.B., and Brugge, J.S. (2013). Frequency-modulated pulses of ERK activity transmit quantitative proliferation signals. Mol Cell 49, 249-261.

Ashall, L., Horton, C.A., Nelson, D.E., Paszek, P., Harper, C.V., Sillitoe, K., Ryan, S., Spiller, D.G., Unitt, J.F., Broomhead, D.S., et al. (2009). Pulsatile stimulation determines timing and specificity of NF-kappaB-dependent transcription. Science (New York, NY) 324, 242-246.

Berridge, M.J., Bootman, M.D., and Roderick, H.L. (2003). Calcium signalling: dynamics, homeostasis and remodelling. Nature reviews Molecular cell biology 4, 517-529.

Cai, L., Dalal, C.K., and Elowitz, M.B. (2008). Frequency-modulated nuclear localization bursts coordinate gene regulation. Nature 455, 485-490.

Cheong, R., Rhee, A., Wang, C.J., Nemenman, I., and Levchenko, A. (2011). Information transduction capacity of noisy biochemical signaling networks. Science 334, 354-358.

Collins, J.J., Imhoff, T.T., and Grigg, P. (1996). Noise-enhanced information transmission in rat SA1 cutaneous mechanoreceptors via aperiodic stochastic resonance. Journal of neurophysiology 76, 642-645.

Dolmetsch, R.E., Xu, K., and Lewis, R.S. (1998). Calcium oscillations increase the efficiency and specificity of gene expression. Nature 392, 933-936.

Douglass, J.K., Wilkens, L., Pantazelou, E., and Moss, F. (1993). Noise enhancement of information transfer in crayfish mechanoreceptors by stochastic resonance. Nature 365, 337-340.

Eldar, A., and Elowitz, M.B. (2010). Functional roles for noise in genetic circuits. Nature 467, 167-173.

Elowitz, M.B., Levine, A.J., Siggia, E.D., and Swain, P.S. (2002). Stochastic gene expression in a single cell. Science 297, 1183-1186.

Erzberger, A., Hampp, G., Granada, A.E., Albrecht, U., and Herzel, H. (2013). Genetic redundancy strengthens the circadian clock leading to a narrow entrainment range. Journal of the Royal Society, Interface / the Royal Society 10, 20130221.

Falcke, M. (2003). Deterministic and stochastic models of intracellular Ca2+ waves. New J Phys 5.

Gerard, C., and Goldbeter, A. (2012). Entrainment of the mammalian cell cycle by the circadian clock: modeling two coupled cellular rhythms. PLoS computational biology 8, e1002516.

Goldbeter, A., Li, Y., and Dupont, G. (1990). Oscillatory dynamics in intercellular communication. Biomed Biochim Acta 49, 935-940.

Goldbeter, A., and Pourquie, O. (2008). Modeling the segmentation clock as a network of coupled oscillations in the Notch, Wnt and FGF signaling pathways. Journal of theoretical biology 252, 574-585.

Gómez-Sjöberg, R., Leyrat, A.A., Pirone, D.M., Chen, C.S., and Quake, S.R. (2007). Versatile, fully automated, microfluidic cell culture system. Analytical chemistry 79, 8557-8563.

Han, Q., Bagheri, N., Bradshaw, E.M., Hafler, D.A., Lauffenburger, D.A., and Love, J.C. (2012). Polyfunctional responses by human T cells result from sequential release of cytokines. Proc Natl Acad Sci U S A 109, 1607-1612.

Hao, S., and Baltimore, D. (2013). RNA splicing regulates the temporal order of TNF-induced gene expression. Proc Natl Acad Sci U S A 110, 11934-11939.

Hayden, M.S., and Ghosh, S. (2008). Shared principles in NF-kappaB signaling. Cell 132, 344-362.

Hoffmann, A., Levchenko, A., Scott, M.L., and Baltimore, D. (2002). The IkappaB–NF-kappaB Signaling Module: Temporal Control and Selective Gene Activation. Science (New York, NY), 1-5.

Huh, D., and Paulsson, J. (2011). Random partitioning of molecules at cell division. Proc Natl Acad Sci U S A 108, 15004-15009.

Jensen, M.H., and Krishna, S. (2012). Inducing phase-locking and chaos in cellular oscillators by modulating the driving stimuli. FEBS letters 586, 1664-1668.

Junkin, M., and Tay, S. (2014). Microfluidic single-cell analysis for systems immunology. Lab Chip 14, 1246-1260.

Kageyama, R., Ohtsuka, T., Shimojo, H., and Imayoshi, I. (2008). Dynamic Notch signaling in neural progenitor cells and a revised view of lateral inhibition. Nature neuroscience 11, 1247-1251.

Kellogg, R.A., Gomez-Sjoberg, R., Leyrat, A.A., and Tay, S. (2014). High-throughput microfluidic single-cell analysis pipeline for studies of signaling dynamics. Nature protocols 9, 1713-1726.

Kupzig, S., Walker, S.A., and Cullen, P.J. (2005). The frequencies of calcium oscillations are optimized for efficient calcium-mediated activation of Ras and the ERK/MAPK cascade. Proc Natl Acad Sci U S A 102, 7577-7582.

Lee, T.K., Denny, E.M., Sanghvi, J.C., Gaston, J.E., Maynard, N.D., Hughey, J.J., and Covert, M.W. (2008). A noisy paracrine signal determines the cellular NF-kappaB response to lipopolysaccharide. Science signaling 2, ra65.

Leloup, J.C., and Goldbeter, A. (2003). Toward a detailed computational model for the mammalian circadian clock. Proc Natl Acad Sci U S A 100, 7051-7056.

Lindner, B., Garcia-Ojalvo, J., Neiman, A., and Schimansky-Geier, L. (2004). Effects of noise in excitable systems. Phys Rep 392, 321-424.

Lipniacki, T., Paszek, P., Brasier, A.R., Luxon, B., and Kimmel, M. (2004). Mathematical model of NF-kappaB regulatory module. Journal of theoretical biology 228, 195-215.

Lipniacki, T., Puszynski, K., Paszek, P., Brasier, A.R., and Kimmel, M. (2007). Single TNFalpha trimers mediating NF-kappaB activation: stochastic robustness of NF-kappaB signaling. BMC bioinformatics 8, 376.

Little, J.W., Shepley, D.P., and Wert, D.W. (1999). Robustness of a gene regulatory circuit. The EMBO journal 18, 4299-4307.

Longo, D.M., Selimkhanov, J., Kearns, J.D., Hasty, J., Hoffmann, A., and Tsimring, L.S. (2013). Dual delayed feedback provides sensitivity and robustness to the NF-kappaB signaling module. PLoS computational biology 9, e1003112.

McDonnell, M.D., and Ward, L.M. (2011). The benefits of noise in neural systems: bridging theory and experiment. Nat Rev Neurosci 12, 415-426.

Mondragon-Palomino, O., Danino, T., Selimkhanov, J., Tsimring, L., and Hasty, J. (2011). Entrainment of a population of synthetic genetic oscillators. Science 333, 1315-1319.

Mori, T., and Kai, S. (2002). Noise-induced entrainment and stochastic resonance in human brain waves. Physical Review Letters 88, 218101.

Nelson, D.E., Ihekwaba, A.E.C., Elliott, M., Johnson, J.R., Gibney, C.A., Foreman, B.E., Nelson, G., See, V., Horton, C.A., Spiller, D.G., et al. (2004). Oscillations in NF-kappaB signaling control the dynamics of gene expression. Science (New York, NY) 306, 704-708.

Paszek, P., Ryan, S., Ashall, L., Sillitoe, K., Harper, C.V., Spiller, D.G., Rand, D.A., and White, M.R. (2010). Population robustness arising from cellular heterogeneity. Proc Natl Acad Sci U S A 107, 11644-11649.

Pekalski, J., Zuk, P.J., Kochanczyk, M., Junkin, M., Kellogg, R., Tay, S., and Lipniacki, T. (2013). Spontaneous NF-kappaB activation by autocrine TNFalpha signaling: a computational analysis. PloS one 8, e78887.

Perc, M., and Marhl, M. (2003). Noise enhances robustness of intracellular Ca2+ oscillations. Phys Lett A 316, 304-310.

Phelps, C.B., Sengchanthalangsy, L.L., Malek, S., and Ghosh, G. (2000). Mechanism of kappa B DNA binding by Rel/NF-kappa B dimers. J Biol Chem 275, 24392-24399.

Pikovsky, A., Rosenblum, M., and Kurths, J. (2003). Synchronization: a universal concept in nonlinear sciences, Vol 12 (Cambridge university press).

Purvis, J.E., Karhohs, K.W., Mock, C., Batchelor, E., Loewer, A., and Lahav, G. (2012). p53 dynamics control cell fate. Science 336, 1440-1444.

Purvis, J.E., and Lahav, G. (2013). Encoding and decoding cellular information through signaling dynamics. Cell 152, 945-956.

Reppert, S.M., and Weaver, D.R. (2002). Coordination of circadian timing in mammals. Nature 418, 935-941.

Schutze, J., Mair, T., Hauser, M.J.B., Falcke, M., and Wolf, J. (2011). Metabolic Synchronization by Traveling Waves in Yeast Cell Layers. Biophysical Journal 100, 809-813.

Shankaran, H., Ippolito, D.L., Chrisler, W.B., Resat, H., Bollinger, N., Opresko, L.K., and Wiley, H.S. (2009). Rapid and sustained nuclear-cytoplasmic ERK oscillations induced by epidermal growth factor. Mol Syst Biol 5, 332.

Suel, G.M., Garcia-Ojalvo, J., Liberman, L.M., and Elowitz, M.B. (2006). An excitable gene regulatory circuit induces transient cellular differentiation. Nature 440, 545-550.

Swain, P.S., Elowitz, M.B., and Siggia, E.D. (2002). Intrinsic and extrinsic contributions to stochasticity in gene expression. Proc Natl Acad Sci U S A 99, 12795-12800.

Tay, S., Hughey, J.J., Lee, T.K., Lipniacki, T., Quake, S.R., and Covert, M.W. (2010). Single-cell NF-kappaB dynamics reveal digital activation and analogue information processing. Nature 466, 267-271.

Turner, D.A., Paszek, P., Woodcock, D.J., Nelson, D.E., Horton, C.A., Wang, Y., Spiller, D.G., Rand, D.A., White, M.R., and Harper, C.V. (2010). Physiological levels of TNFalpha stimulation induce stochastic dynamics of NF-kappaB responses in single living cells. J Cell Sci 123, 2834-2843.

Varela, F., Lachaux, J.P., Rodriguez, E., and Martinerie, J. (2001). The brainweb: phase synchronization and large-scale integration. Nat Rev Neurosci 2, 229-239.

Vilar, J.M., Kueh, H.Y., Barkai, N., and Leibler, S. (2002). Mechanisms of noise-resistance in genetic oscillators. Proc Natl Acad Sci U S A 99, 5988-5992.

Wakamoto, Y., Dhar, N., Chait, R., Schneider, K., Signorino-Gelo, F., Leibler, S., and McKinney, J.D. (2013). Dynamic persistence of antibiotic-stressed mycobacteria. Science 339, 91-95.

Wang, Y., Paszek, P., Horton, C.A., Kell, D.B., White, M.R., Broomhead, D.S., and Muldoon, M.R. (2011). Interactions among oscillatory pathways in NF-kappa B signaling. BMC systems biology 5, 23.

Wee, K.B., Yio, W.K., Surana, U., and Chiam, K.H. (2012). Transcription factor oscillations induce differential gene expressions. Biophys J 102, 2413-2423.

Yang, Q., Pando, B.F., Dong, G., Golden, S.S., and van Oudenaarden, A. (2010). Circadian gating of the cell cycle revealed in single cyanobacterial cells. Science 327, 1522-1526.

Yde, P., Mengel, B., Jensen, M.H., Krishna, S., and Trusina, A. (2011). Modeling the NF-kappaB mediated inflammatory response predicts cytokine waves in tissue. BMC systems biology 5, 115.

Yissachar, N., Sharar Fischler, T., Cohen, A.A., Reich-Zeliger, S., Russ, D., Shifrut, E., Porat, Z., and Friedman, N. (2013). Dynamic response diversity of NFAT isoforms in individual living cells. Mol Cell 49, 322-330.

Yoshiura, S., Ohtsuka, T., Takenaka, Y., Nagahara, H., Yoshikawa, K., and Kageyama, R. (2007). Ultradian oscillations of Stat, Smad, and Hes1 expression in response to serum. Proc Natl Acad Sci U S A 104, 11292-11297.

Zhou, C., Kurths, J., Kiss, I.Z., and Hudson, J.L. (2002). Noise-enhanced phase synchronization of chaotic oscillators. Phys Rev Lett 89, 014101.

SUPPLEMENTAL INFORMATION

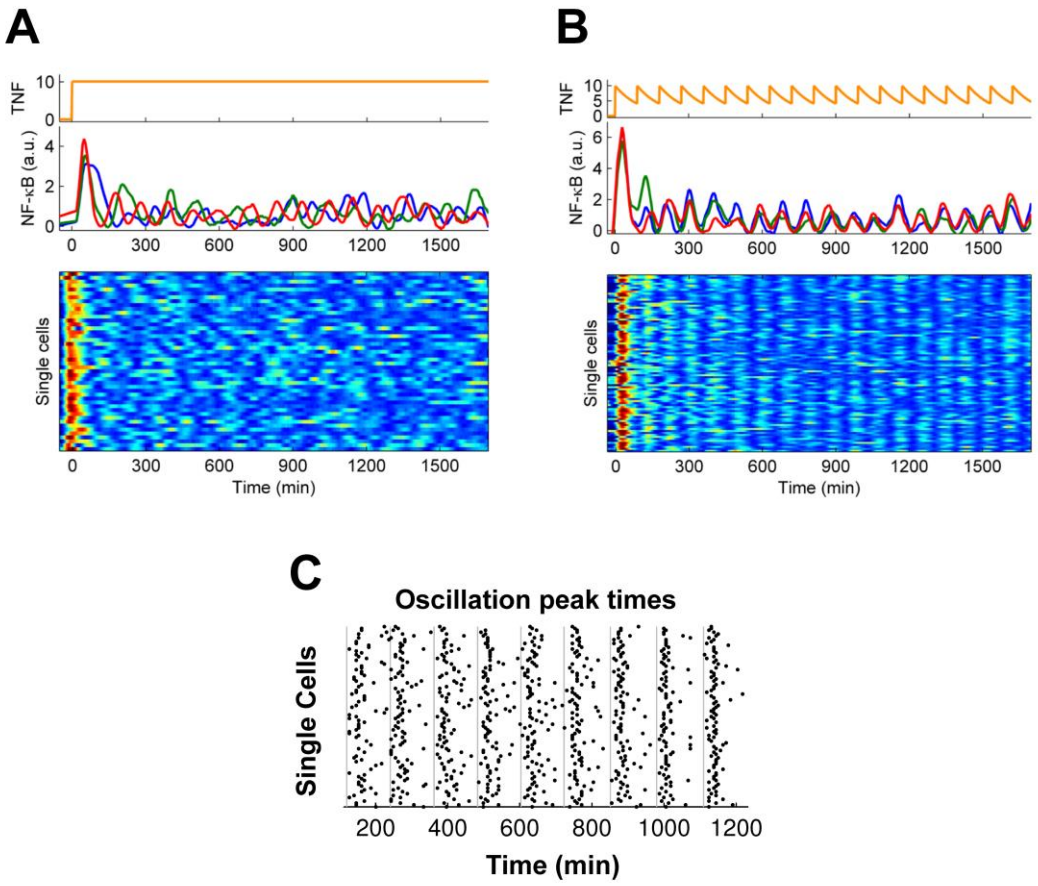

Figure S1. Comparison of NF-κB dynamics for constant and periodic (entraining) TNF stimulation, Related to Figure 2

A) Constant TNF input leads to asynchronous, heterogeneous oscillations in the population. B) Periodic input (90 min interval) generates entrained, synchronous population response. Color code in heatplots indicates NF-κB nuclear intensity from low (blue) to high (red). C) Peak timing for 120 min periodic TNF (10ng/ml) input. Over time, timing of NF-κB oscillations in the population becomes increasingly synchronized.

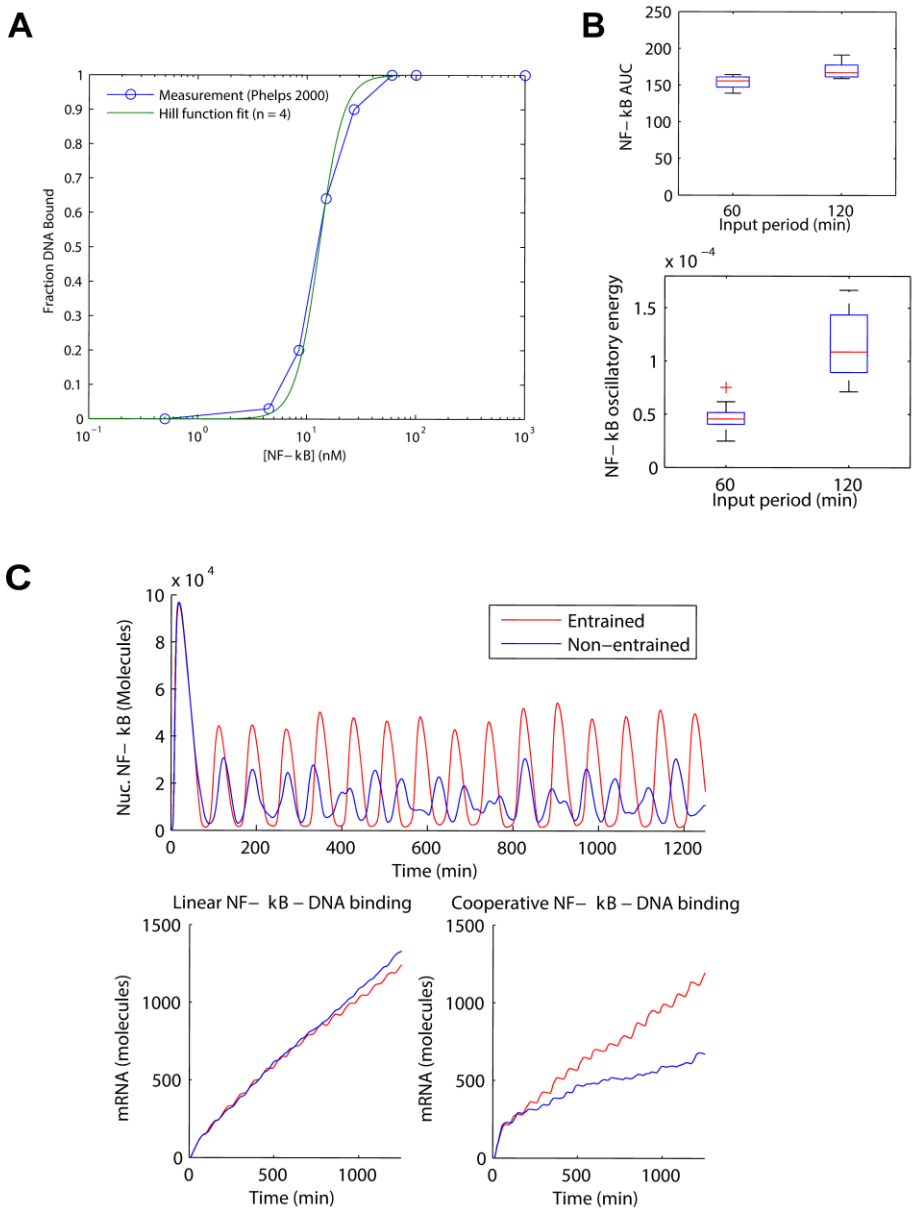

Figure S2. Nonlinear NF-κB – DNA binding increases oscillation-mediated transcriptional output, Related to Figure 3

A) Fitting of experimental NF-κB – DNA binding data from (Phelps et al., 2000). B) Area and oscillatory energy of simulated NF-κB trajectories for non-entraining (60 min) versus entraining (120 min) periodic input. C) Comparison of simulated NF-κB dynamics and mRNA output for entraining vs non-entraining model input, for linear and nonlinear (cooperative) NF-κB – DNA binding. Nonlinear NF-κB binding reproduces the experimentally observed gene expression enhancement under entrainment.

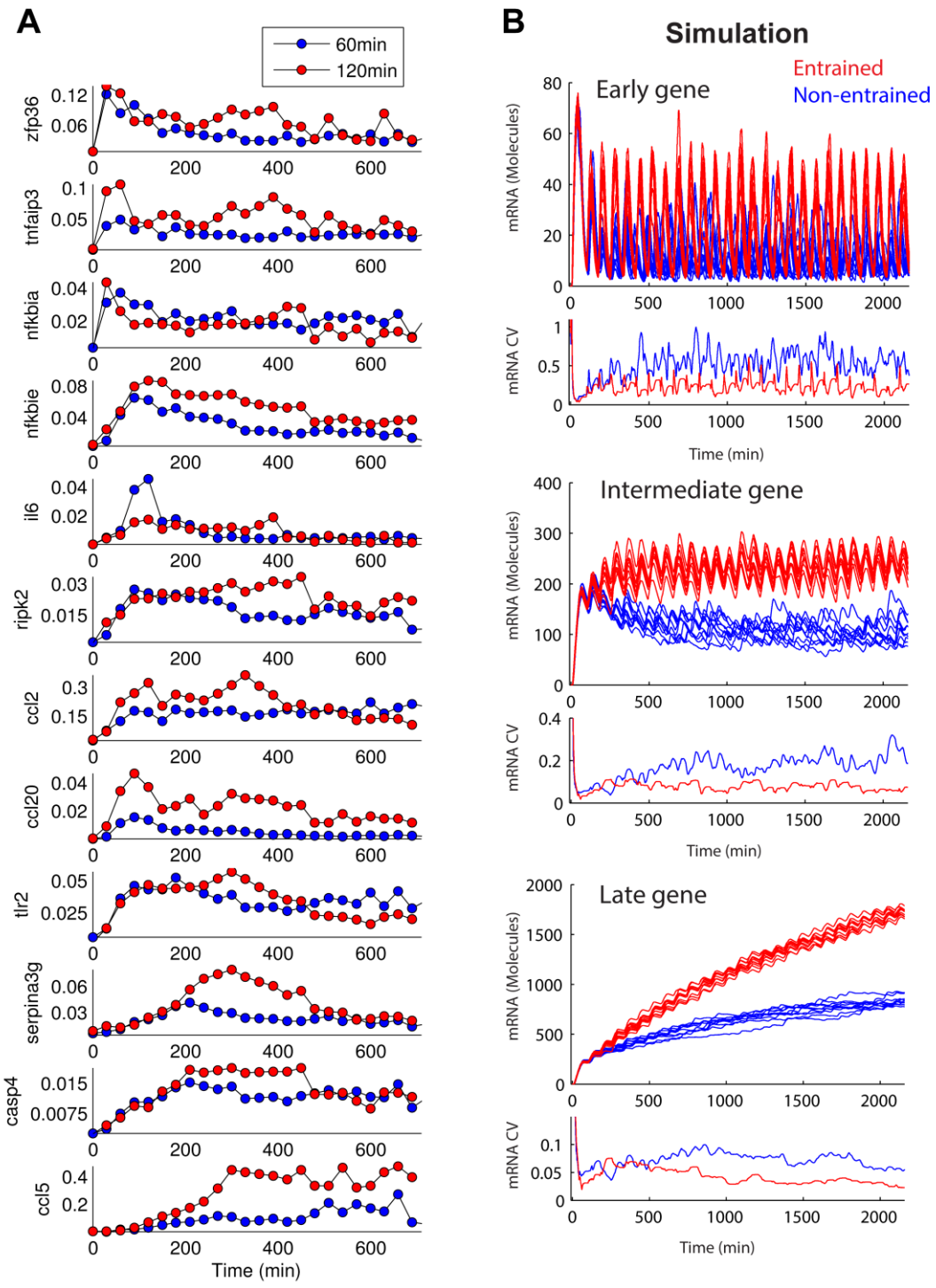

Figure S3. Enhanced NF-κB dependent gene expression under entraining input, Related to Figure 3

A) Gene expression under periodic stimulation ordered from early (top) to late (bottom). Relative expression values are plotted as 2ct_gene-ct_gapdh. TNF (10ng/ml) was provided for 60min (blue) or 120min (red) periodic input, and population gene expression was measured every 30 minutes.

Experiment duration was 12 hours. Stimulation and cell retrieval was conducted using the microfluidic cell culture chip. B) Simulated single-cell mRNA output for entrained vs. non-entrained conditions for early and intermediate genes not shown in main text. Early, intermediate, and late genes are simulated by varying transcript stability (Tdeg). Values for Tdeg are 103 (~17 min), 104 (~2.7 h), and 105 s (~27 h) to simulate early, intermediate, and late genes, respectively. Regardless of mRNA half-life, entrainment leads to both increased expression and reduced variability compared to non-entraining input.

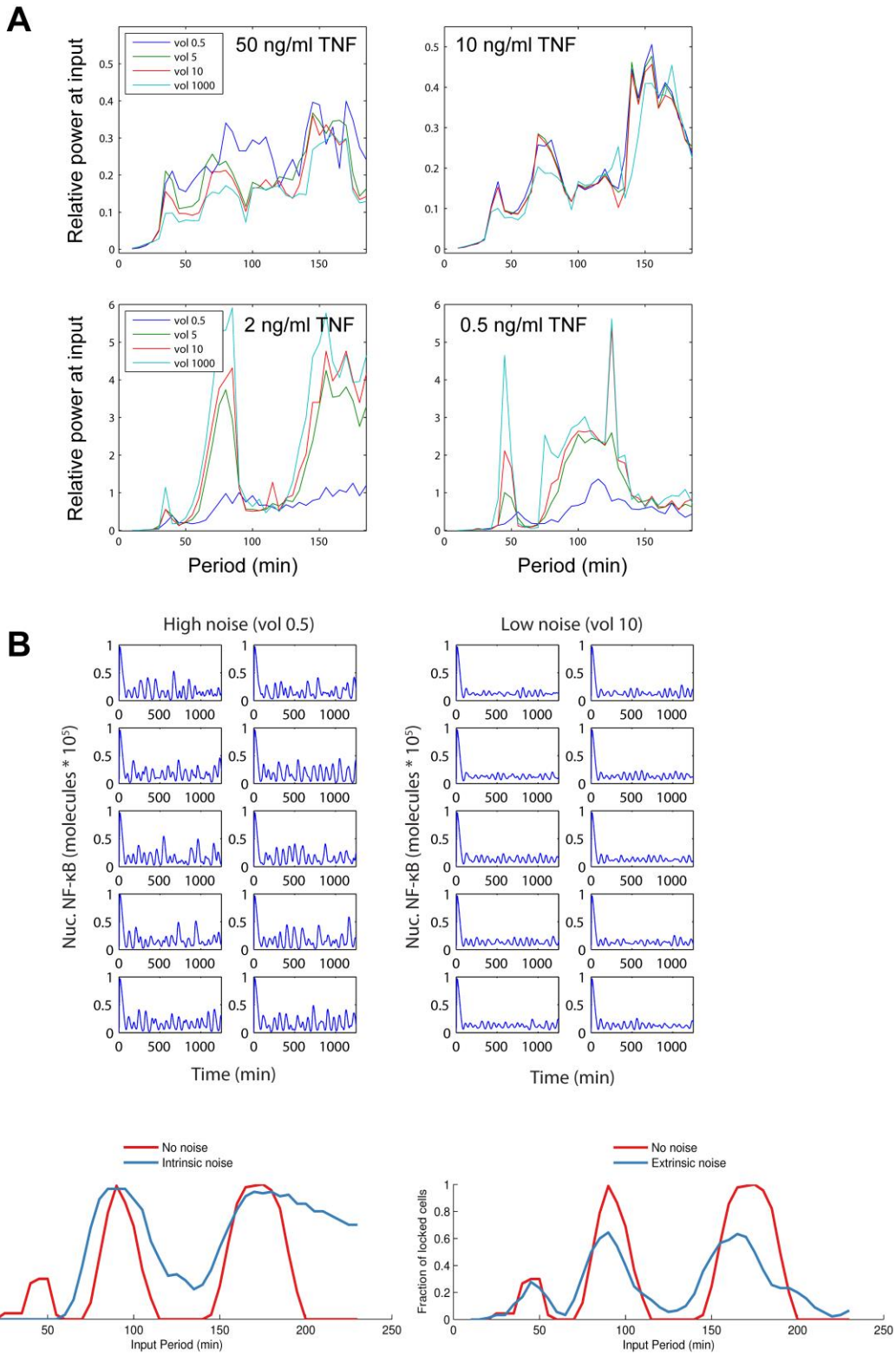
A
50 ng/ml TNF
10 ng/ml TNF
2 ng/ml TNF
0.5 ng/ml TNF
vol 0.5
vol 5
vol 10
vol 1000
Relative power at input
Period (min)
B
High noise (vol 0.5)
Low noise (vol 10)
Nuc. NF-κB (molecules * 10^5)
Time (min)
C
No noise
Intrinsic noise
Extrinsic noise
Fraction of locked cells
Input Period (min)

Figure S4. Additional simulations on role of noise in NF-κB entrainment under different TNF doses, Related to Figure 4

A) Stochastic differential equation (SDE) hybrid simulations of entrainment under various doses of sawtooth like periodic TNF inputs. Entrainment (y-axis) is quantified by the ratio of the spectral power at the input to the total power at other frequencies. Intrinsic noise increases when the reaction volume becomes smaller, reaching a maximum noise level at v=0.5. Reaction volume v=1000 produces near-deterministic conditions. Higher intrinsic noise improves entrainment at TNF doses of 50 and 10 ng/ml. B) Comparison of single-cell NF-κB trajectories for high and low noise conditions under resonant (95 min, 50ng/ml TNF) stimulation using SDE simulation. High noise (left) generates significantly increased oscillation amplitude and higher entrainment score. High NF-κB oscillation amplitude leads to increased gene expression (Fig. S2 and S3). C) Effect of intrinsic and extrinsic noise of the fraction of cells that phase-lock in the population. For the simulation analysis cell responses that phase-lock for > 60% of a 24hr timecourse are declared "locked". Intrinsic noise (left) widens the input range that causes locking for an individual cell. Extrinsic noise (right) increases the variation in natural period between cells, leading also to wider entrainment range.

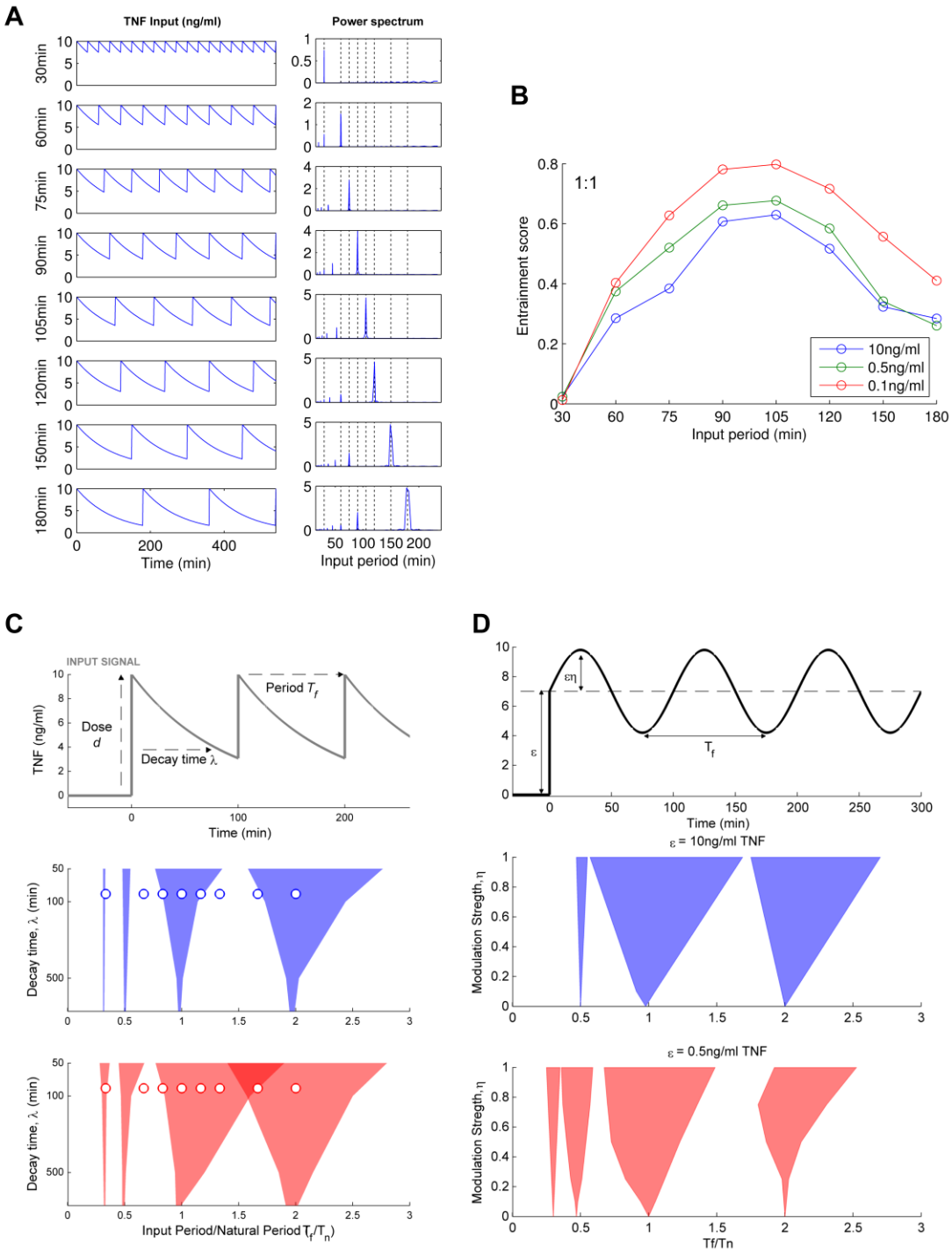

Figure S5. NF-κB Arnold tongue simulations, Related to Figure 5

A) Temporal profile and power spectrum for experimentally established periodic TNF input signals. B) Experimentally measured entrainment efficiency at different TNF doses for 1:1 locking. C) Arnold tongues numerically computed for sawtooth input. Modulation amplitude varies inverse proportionally with decay time λ. Lower input level gives rise to wider entrainment regions. Upper panel shows input function TNF(t) = d*exp(-λ*mod(t,Tf)). Middle panel shows entrainment regions for d = 10 (TNF 10ng/ml). Small circles correspond to experimental inputs. Lower panel shows entrainment regions for d = 0.5 (TNF 0.5ng/ml). D) Arnold tongues for numerically computed for sinusoidal TNF input. Lower input level leads to narrower entrainment regions for Tf/Tn period ratios greater than one but wider regions for ratio less than 1. Top panel shows sinusoidal input function, TNF(t) = ϵ(1+ ηsin(2πt/Tf)) (Wang et al., 2011). Middle panel shows entrainment regions for ϵ = 10 (10ng/ml TNF) and varying η from 0 to 1. Lower panel shows entrainment regions for ϵ = 0.5 (0.5ng/ml TNF) and varying η from 0 to 1.

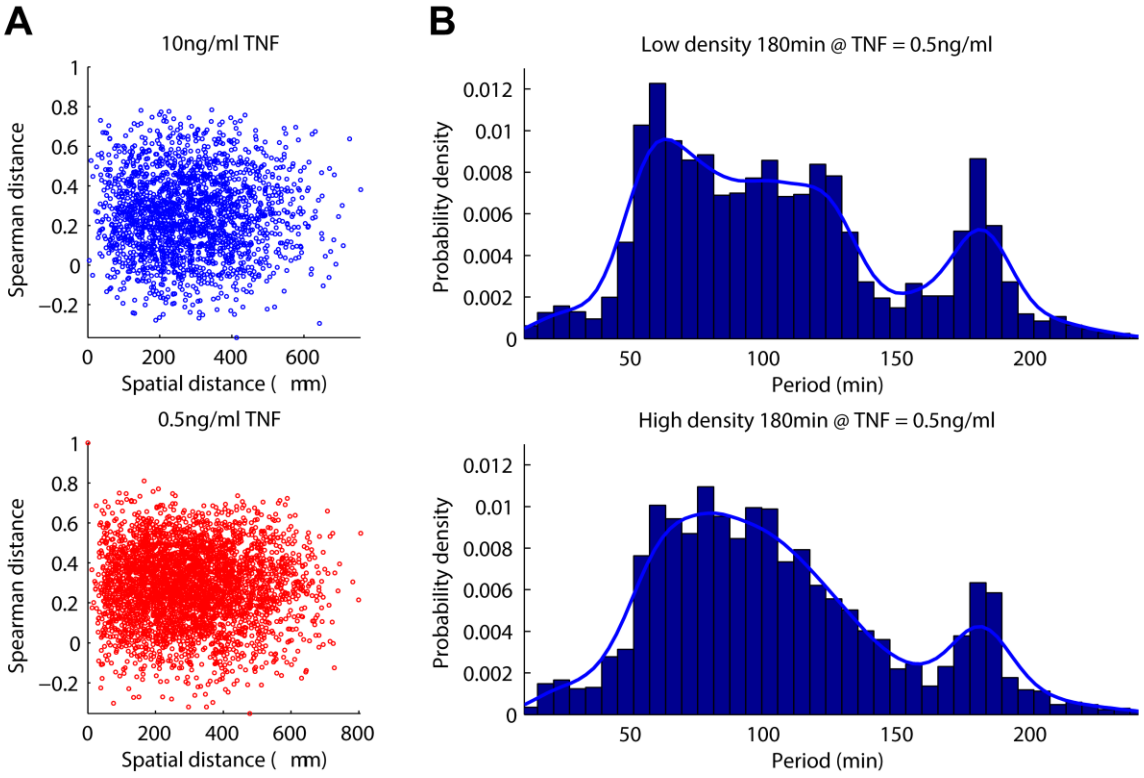

Figure S6. Influence of spatial distance on entrainment, Related to Figure 6

A) Spatial distance between cells and similarity in their oscillatory responses (by Spearman correlation coefficient) do not correlate strongly, in agreement with previous findings (Lee et al., 2008). B) Changing cell density from a low (50 cells/chamber) to high (300 cells/chamber) does not alter the distribution of peak-to-peak (period) time. These findings suggest that spatial paracrine or contact mediated interactions do not play a major role in the observed entrainment.

EXTENDED EXPERIMENTAL PROCEDURES

Numerical computation of phase-locked regions (Arnold Tongues). We follow a similar procedure as described previously (Mondragon-Palomino et al., 2011). Sinusoidal input is simulated as shown (Fig. S5). To construct Arnold Tongue diagrams for sawtooth input (Fig. 4A), period T_f is varied from 15-250 min at 0.5 min increments and decay rate λ is varied from 50 to 1000 sec (0.833 to 16.67 min) and locking regions are displayed in terms of modulation amplitude ($1/\lambda$). To construct Arnold Tongue diagrams for sinusoid input (Fig. S5D), period T_f is varied from 15-250 min at 0.5 min increments and modulation strength η is varied from 0 to 1. Simulations are run for sufficient duration (500 hr) to accumulate 90-100 phase measurements. Phase is the distance from start of an input cycle to the following NF-κB oscillation peak. If a new input begins before a NF-κB peak appears, no phase measurement is recorded for the cycle. The CV of these phase measurements is computed, and if the value is below an arbitrary threshold 0.1, the response is considered phase-locked.

Analysis of peak timing variability. Between-cell variability (BCV) and within-cell variability (WCV) are expressed in terms of coefficient of variation (standard deviation / mean). BCV is the variation in mean period: Define M = vector of mean period for each cell. BCV = sqrt(var(M))/mean(M). WCV is the mean period variation: Define V = vector of period CV for each cell. WCV = mean(V).

Analysis of phase locking. Phase ϕ is computed for each input cycle as distance from the next occurring NF-κB peak (if one occurs in the time before a new input cycle starts). This distance is normalized to the input period to arrive at a phase value in the range (0-1]. To assess locking, the current phase measurement ϕ_t is compared to the previous phase ϕ_{t-1}. Phase-locking is defined as a phase change less than 15% ($|\phi_t - \phi_t\text{-}1| < 0.15$). Locking ratio is expressed as (# of input cycles):(# of response cycles) occurring during the time between ϕ_t and ϕ_{t-1} measurements. Locking fraction indicates the proportion of cycles locked at each ratio compared to the total number of cycles, computed as number of locked input-response cycles over total input-response cycles.

Spectral Analysis. Single cell time traces were transformed into frequency domain power spectral density (PSD) using the Matlab *fft* function. Frequencies were converted to periods to facilitate interpretation. A spectrum-based entrainment measure (Relative power at

input) is defined as the ratio of energy at input to non-input frequencies. The degree of oscillation in a signal (Oscillatory energy) is defined as energy in the power spectrum for periods shorter than 200 min.

Simulation of NF-κB dynamics and entrainment using a hybrid stochastic-deterministic model based on Gillespie algorithm

We used deterministic and hybrid stochastic-deterministic models of the NF-κB pathway published previously (Tay et al., 2010). In the hybrid model, receptor binding and transcription are modeled stochastically while remaining interactions are modeled deterministically.

The model includes the following components:

IKKn	Neutral form of IKK kinase
IKKa	Active form of IKK
IKKi	Inactive form of IKK
K_{NN}	Total number of IKK=IKKn+IKKa+IKKi+IKKii molecules (assumed constant in time)
IKKKa	Active form of IKKK
IKKKn	Neutral form of IKKK
K_N	Total number of IKKK=IKKKn+IKKKa molecules (assumed to be constant in time)
IkB	Cytoplasmic IκBα
IkB_n	Nuclear IκBα
IkB_t	IκBα transcript
IkB_p	Phosphorylated cytoplasmic IκBα
A20	A20 protein
A20t	A20 transcript
Rt	Reporter transcript
NFkB	Cytoplasmic NF-κB
$NFkB_n$	Nuclear NF-κB
NFkB|IkB	Cytoplasmic (NF-κB-IκBα) complexes
NFkB|IkB_p	Phosphorylated cytoplasmic IκBα complexed to NF-κB
NFkB|IkB_n	Nuclear (NF-κB-IκBα) complexes

TNF_{ext}	Extracellular TNFα concentration [ng/ml]
G_{IkB}	Discrete random variable, state of IκBα gene
G_{A20}	Discrete random variable, state of A20 gene
G_R	Discrete random variable, state of reporter gene
B	Number of active receptors
M	Total number of receptors (assumed to be constant in time)

The model includes the following parameters:

Parameter	Value	Description
$k_v = V/U$	5	Ratio of cytoplasmic to nuclear volume
M_{MEFs}	10^3 molecules	Average number of TNFR1 for MEFs cell simulations
K_N	10^5 molecules	Number of IKKK molecules
NF-κB_{tot}	10^5 molecules	Average number of NF-κB molecules
Tdeg	2×10^{-4} s^{-1}	TNF degradation
k_b	1.2×10-5 s^{-1} $molecules^{-1}$	Receptor activation rate
k_f	1.2×10-3 s^{-1}	Receptor inactivation rate
k_a	2×10^{-5} s^{-1}	IKKK activation rate
k_i	10^{-2} s^{-1}	IKKK inactivation rate
k_1	6×10^{-10} s^{-1} $molecules^{-2}$	IKKn activation rate
k_{A20}	10^5 molecules	Michaelis coefficient in TNFR1 activity attenuation
k_2	10^4 molecules	Michaelis coefficient in IKKa inactivation
k_3	2×10^{-3} s^{-1}	IKKn inactivation rate
k_4	10^{-3} s^{-1}	IKKi→IKKii and IKKii→IKKn transformation
q_1	4×10^{-7} s^{-1}	NF-κB binding at A20 and IκBα gene promoters

q_2	10^{-6} s^{-1}	IκBα inducible NF-κB detaching from A20 and IκBα genes
c_1	0.1 s^{-1}	inducible A20 and IκBα mRNA synthesis
c_3	7.5×10^{-4} s^{-1}	A20 and IκBα mRNA degradation
c_4	0.5 s^{-1}	A20 and IκBα translation - fitted
c_5	5×10^{-4} s^{-1}	A20 degradation rate
a_1	5×10^{-7} s^{-1} $molecules^{-1}$	IκBα association NF-κB
a_2	10^{-7} s^{-1} $molecules^{-1}$	IκBα phosphorylation
a_3	5×10^{-7} s^{-1} $molecules^{-1}$	IκBα phosphorylation in IκBα|NF-κB complexes
t_p	10^{-2} s^{-1}	degradation of phosphorylated IκBα
c_{5a}	10^{-4} s^{-1}	spontaneous IκBα degradation
c_{6a}	2×10^{-5} s^{-1}	spontaneous IκBα degradation in IκBα|NF-κB complexes
i_1	10^{-2} s^{-1}	NF-κB nuclear import
e_{2a}	5×10^{-2} s^{-1}	IκBα|NF-κB nuclear export
i_{1a}	2×10^{-3} s^{-1}	IκBα nuclear import
e_{1a}	5×10^{-3} s^{-1}	1 IκBα nuclear export
q_{1r}	10^{-7} s^{-1}	NF-κB binding at reporter gene promoter
q_{2r}	10^{-7} s^{-1}	IκBα inducible NF-κB detaching from reporter gene
q_{2rr}	$10^{-3}s^{-1}$	Spontaneous NF-κB detaching from reporter gene
c_{1r}	$5x10^{-2}s^{-1}$	Inducible reporter mRNA synthesis
c_{1rr}	10^{-3} s^{-1}	Reporter mRNA constitutive synthesis
c_{3r}	Various: 10^{-3} s (~17 min) – early gene 10^{-4} s (~2.7 h) – mid gene 10^{-5} s (~27 h) – late gene	Reporter mRNA degradation rate
k_r	5	Half-max value for cooperative NF-κB – DNA binding
n	4	Hill coefficient for cooperative NF-κB – DNA binding
ANa	2	IκB α alleles
AN	2	A20 alleles
ANr	2	Reporter gene alleles

The following ODEs comprise the fast reactions (all but transcription and receptor activity):

$$\frac{d[IKKKa]}{dt} = k_a * B(t) * (K_N - [IKKKa]) * \frac{k_{a20}}{k_{a20} + [A20]} - ki * [IKKKa]$$

$$\frac{d[IKKn]}{dt} = -[IKKKa]^2 * k_1 * [IKKn] + k_4 * (K_{NN} - [IKKn] - [IKKa] - [IKKi])$$

$$\frac{d[IKKa]}{dt} = [IKKKa]^2 * k_1 * [IKKn] - k_3 * [IKKa] * (k_2 + [A20])/k_2$$

$$\frac{d[IKKi]}{dt} = k_3 * [IKKa] * \frac{k_2 + [A20]}{k_2} - k_4 * [IKKi]$$

$$\frac{d[IkB_p]}{dt} = a_2 * [IKKa] * [IkB] - t_p * [IkB_p]$$

$$\frac{d[NFkB|IkB_p]}{dt} = a_3 * [IKKa] * [NFkB|IkB] - t_p * [NFkB|IkB_p]$$

$$\frac{d[NFkB]}{dt} = c_{6a} * [NFkB|IkB] - a_1 * [NFkB] * [IkB] + t_p * \left[NFkB\middle|IkB_p\right] - i_1 * [NFkB]$$

$$\frac{d[NFkB_n]}{dt} = i_1 * [NFkB] - a_1 * k_v * [IkB_n] * [NFkB_n]$$

$$\frac{d[A20]}{dt} = c_4 * [A20_t] - c_5 * [A20]$$

$$\frac{d[A20_t]}{dt} = c_1 * [G_{A20}] - c_3 * [A20_t]$$

$$\frac{d[IkB]}{dt} = -a_2 * IKKa * IkB - a_1 * IkB * NFkB + c4 * IkB_t - c_{5a} * IkB - i_{1a} * IkB + e_{1a} * IkB_n$$

$$\frac{d[IkB_n]}{dt} = -a_1 * k_v * [IkB_n] * [NFkB_n] + i_{1a} * [IkB] - e_{1a} * [IkB_n]$$

$$\frac{d[IkB_t]}{dt} = c_{1a} * [G_{IkB}] - c_3 * [IkB_t]$$

$$\frac{d[NFkB|IkB]}{dt} = a_1 * [IkB] * [NFkB] - c_{6a} * [NFkB|IkB] - a3 * [IKKa] * [NFkB|IkB] + e2a * [NFkB|IkB_n]$$

$$\frac{d[NFkB|IkB_n]}{dt} = a_1 * k_v * [IkBa_n] * [NFkB_n] - e_{2a} * [NFkB|IkB_n]$$

Reporter gene transcript with cooperative induction:

$$\frac{d[R_t]}{dt} = c_1 * \frac{[G_R]^n}{(k_r^n + [G_R]^n)} - c_3 * [R_t]$$

The following are ODEs for the slow reactions (IκBα, A20, and Reporter gene and receptor activation) used in the deterministic approximation:

$$\frac{d[B]}{dt} = k_b * [TNF] * (M - [B]) - k_f * [B]$$

$$\frac{d[G_{A20}]}{dt} = q_1 * [NFkB_n] * (A_N - [G_{A20}]) - q_2 * IkB_n * [G_{A20}]$$

$$\frac{d[G_{IkB}]}{dt} = q1 * [NFkB_n] * (A_{Na} - [G_{IkB}]) - q_2 * [IkB_n] * [G_{IkB}]$$

$$\frac{d[G_R]}{dt} = q1 * [NFkB_n] * (A_{Nr} - [G_R]) - q_2 * [IkB_n] * [G_R]$$

In the hybrid model, fast reactions are modeled stochastically. Receptors activate with and inactivate with propensities R^b and R^d, respectively, as follows:

$$[R_r^b] = kb * [TNF_{ext}]$$

$$[R_r^d] = kd$$

A20, IκBα, and reporter genes are activated by NF-κB binding and inactivated by IκBα removal of NF-κB:

$$[R^b] = q_1 * [NFkB_n]$$

$$[R^d] = q_2 * [IkB_n]$$

Numerical implementation scheme for the hybrid model is as described (Lipniacki et al., 2007; Tay et al., 2010).

Noise simulation

To simulate extrinsic noise, numbers of NF-κB and TNFR1 across cells follow a lognormal distribution with parameters A, μ, and σ:

$$f = \frac{A}{x\sigma\sqrt{2\pi}} * e^{-\frac{(\ln(x)-\mu)^2}{2*\sigma^2}}$$

	A	**M**	**σ**
NF-κB	10^5	1/√2	-1/4
TNFR1	10^3	√2	-1

Intrinsic noise results from discrete regulation of receptor and gene activity. To affect transcription noise, we increased gene copy number from 2 to 50 (parameters AN and ANa) and proportionally decreased rate of IκB and A20 synthesis (parameter c0).

Simulating continuous and periodic TNF stimulation

To simulate continuous flow, TNF-α input decay rate (model parameter T_{deg}) is set to 0. To simulate periodic replacement, T_{deg} is set to an assumed rate (equal to 2×10^{-4} s^{-1} based on estimated TNF-α degradation and cell internalization) (Lipniacki et al., 2004; Tay et al., 2010) and TNF-α concentration is reset at the defined periodic interval (30-180min) to create a

sawtooth input profile. Parallel simulations were performed using the ETH Zurich Brutus high-performance cluster (www.cluster.ethz.ch).

Hybrid stochastic-deterministic NF-κB simulation using stochastic differential equations

We start with equations governing receptor binding and gene activation as follows:

$$x_1 = k_b * [TNF] * (M - x_1) - k_f * x_1$$

$$x_2 = q_1 * [NFkB_n] * (A_N - x_2) - q_2 * IkB_n * x_2$$

$$x_3 = q1 * [NFkB_n] * (A_{Na} - x_3) - q_2 * [IkB_n] * x_3$$

$$x_4 = q1 * [NFkB_n] * (A_{Nr} - x_4) - q_2 * [IkB_n] * x_4$$

where states x_i and parameter values are described in the following table:

State	Species	Description
x_1	B	Active receptor
x_2	G_{A20}	Gene A20
x_3	G_{IkB}	Gene IκBα
x_4	G_R	Gene Reporter

All parameters are as described in the Gillespie-based model section above. All other equations are simulated deterministically as above.

Stochastic Reaction Network derivation

From the ODE model we derive a stochastic reaction network model for a system with volume Ω. The states x_i are then given by

$$x_i = \frac{y_i}{N_a \cdot \Omega} = \frac{y_i}{\tilde{\Omega}}$$

where $N_a = 6.022 \cdot 10^{23}$ is the Avogadro constant, $\widetilde{\Omega} := N_a \cdot \Omega$ and y_i is the copy number of species s_i. The reactions and corresponding propensities $\omega_k(x)$ are listed in the following table:

1	$\emptyset \to s_1$	$\omega_1(x) = k_b * [TNF] * \left(M - \frac{y_1}{\widetilde{\Omega}}\right)$
2	$s_1 \to \emptyset$	$\omega_2(x) = k_f * \frac{y_1}{\widetilde{\Omega}}$
3	$\emptyset \to s_2$	$\omega_3(x) = q_1 * [NFkB_n] * \left(A_N - \frac{y_2}{\widetilde{\Omega}}\right)$
4	$s_2 \to \emptyset$	$\omega_4(x) = q_2 * IkB_n * \frac{y_2}{\widetilde{\Omega}}$
5	$\emptyset \to s_3$	$\omega_5(x) = q1 * [NFkB_n] * \left(A_{Na} - \frac{y_3}{\widetilde{\Omega}}\right)$
6	$s_3 \to \emptyset$	$\omega_6(x) = q_2 * [IkB_n] * \frac{y_3}{\widetilde{\Omega}}$
7	$\emptyset \to s_4$	$\omega_7(x) = q1 * [NFkB_n] * \left(A_{Nr} - \frac{y_4}{\widetilde{\Omega}}\right)$
8	$s_4 \to \emptyset$	$\omega_8(x) = q_2 * [IkB_n] * \frac{y_4}{\widetilde{\Omega}}$

The dynamics of the species copy numbers are then given by $\{X(t): t \geq 0\}$

$$X(t) = X(0) + \sum_{k=1}^{M} Y_k \left(\int_0^t \omega_k(X(s))ds \right) s_k$$

where $\{Y_k: k = 1, \dots, M\}$ is a family of independent unit rate Poisson processes.

Langevin Approximation derivation

The Langevin Approximation (Van Kampen, 1992) $\{Z(t): t \geq 0\}$ of a Stochastic Reaction Network results in a Stochastic Differential Equation approximating the dynamics of the species concentrations

$$Z(t) = Z(0) + \int_0^t F\big(Z(s)\big)ds + \sum_{k=1}^{M} \frac{1}{\sqrt{\Omega}} \left(\int_0^t \sqrt{\widetilde{\omega}_k\big(Z(s)\big)} dW_k(s) \right) s_k$$

where $F(x) = \sum_{k=1}^{M} \widetilde{\omega}_k(x) s_k$ and $\{W_k: k = 1, \dots, M\}$ is a family of independent standard Brownian motions and the $\widetilde{\omega}_k$-s are the reaction-rate functions from the ODE model:

1	$\emptyset \rightarrow s_1$	$\widetilde{\omega}_1(x) = k_b * [TNF] * (M - x_1)$
2	$s_1 \rightarrow \emptyset$	$\widetilde{\omega}_2(x) = k_f * x_1$
3	$\emptyset \rightarrow s_2$	$\widetilde{\omega}_3(x) = q_1 * [NFkB_n] * (A_N - x_2)$
4	$s_2 \rightarrow \emptyset$	$\widetilde{\omega}_4(x) = q_2 * IkB_n * x_2$
5	$\emptyset \rightarrow s_3$	$\widetilde{\omega}_5(x) = q1 * [NFkB_n] * (A_{Na} - x_3)$
6	$s_3 \rightarrow \emptyset$	$\widetilde{\omega}_6(x) = q_2 * [IkB_n] * x_3$
7	$\emptyset \rightarrow s_4$	$\widetilde{\omega}_7(x) = q1 * [NFkB_n] * (A_{Nr} - x_4)$
8	$s_4 \rightarrow \emptyset$	$\widetilde{\omega}_8(x) = q_2 * [IkB_n] * x_4$

Simulations of the Langevin Approximation are run with volumes varying from ω = 0.5 (low noise) to ω = 1000 (high noise). The equations are solved by the Euler-Maruyama method implemented in Java with a timestep of $dt = 1\ s$ (function *SDE.simByEuler* in Matlab 2014a).

5. CONCLUSIONS

5.1 Summary

This work has developed a microfluidic pipeline for single cell analysis and applied this pipeline towards understanding how cells process temporal fluctuation in signaling inputs. We focused on two dynamic features of the NF-κB pathway – digital activation and noisy oscillation.

The NF-κB digital response is defined at the population level by two characteristics: 1) the percentage of cells exhibiting a response, and 2) the extent of cell-to-cell dynamic heterogeneity in the responses. Previous studies found that for input levels leading to a low fraction of the population responding also led to large cell-to-cell heterogeneity, suggesting that these two response characteristics were linked (Tay et al., 2010). In this work we find that the NF-κB switch in fact decouples activation probability and heterogeneity through processing area and shape of the input profile. By computationally and experimentally screening a range of intensity and duration combinations, we found that input *area* controls the fraction of cells activating, while input *shape* controls the extent of heterogeneity in the response. These two response properties are therefore tunable for specific functions depending on biological context. For example, NF-κB is involved in cytokine secretion in macrophages but regulates cellular differentiation in lymphocytes. Controlling NF-κB heterogeneity would have different effects in these contexts – impacting variability in secretion profile in one case, and variability in lymphocyte phenotypes in the second case.

The reason for NF-κB oscillation has been a mystery since its discovery. We asked how oscillation functions to control transcription. Using periodic input that either enhanced or disrupted NF-κB oscillation without affecting total nuclear NF-κB, we found that oscillation was critical for efficient transcriptional output. Noise widened the range of input frequencies leading to entrainment and enhancement of oscillation. Therefore oscillation serves to sense frequency content of input signals. Oscillation enables cells to communicate by periodic signaling with increased efficiency by requiring fewer TNF molecules to achieve the same level of transcriptional output. Beyond increased efficiency, frequency encoding could increase information capacity and fidelity of cell-cell communication through regulating specific sets of NF-κB genes.

5.2 Emerging concepts

5.2.1 Digital signal integration through the NF-κB switch

Cells face multiple input signals at a time, and it remains uncertain how multiple signal types are integrated by the cell. For multiple inputs to a digital system, the inputs might integrate additively or the cell could make a decision about which input to respond to. In this work we showed that signaling response through TLR4 (via LPS input) is digital, and the area of the input determines the fraction of cells in the population responding. Signaling through TLR2 (via Pam3csk4 – PAM – input) produces dynamics that are distinct from those produced by LPS at low dose. When both input types are applied simultaneously, the population exhibits an approximately equal split in responses – some single cells in

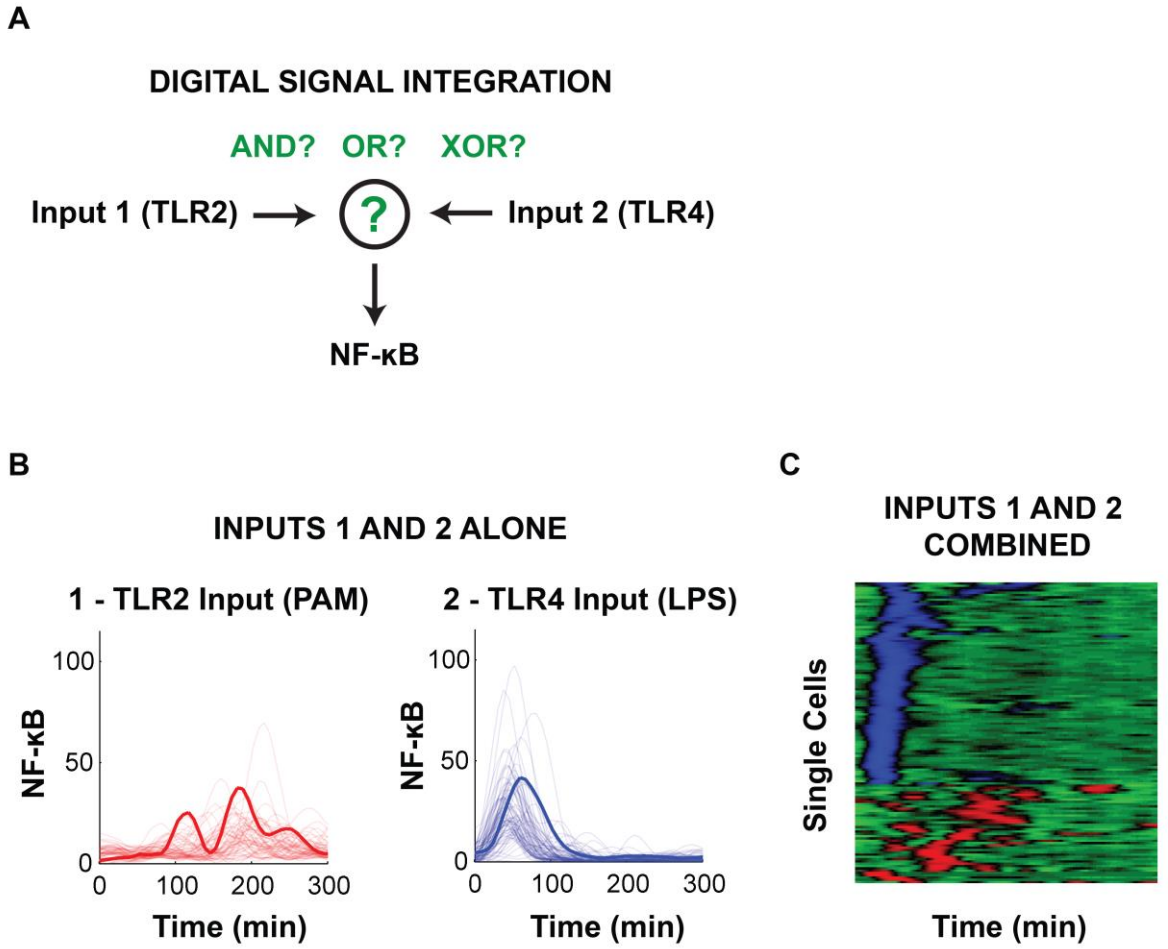

Figure 1. Digital integration of simultaneous inputs. When these two inputs are delivered simultaneously to cells, NF-κB appears to "choose" only one of them. A) It is unclear how the NF-κB switch regulates responses to multiple simultaneous inputs. B) Two TLR ligands, LPS and PAM, show distinct dynamics at low dose. C) Heatplot showing single-cell responses in a population that received simultaneous PAM + LPS input. Color coding indicates that whether the single cell dynamic response matched LPS or PAM, and a fraction of the population exhibits dynamics resembling the response to LPS and the remainder show dynamics corresponding to PAM input.

the population show dynamics that mimic that of PAM input through TLR2, and the other portion shows dynamics resembling LPS input through TLR4.

Similar to how the NF-κB switch responds under dose and duration inputs, this effect could arise from the cooperative process of adaptor assembly upstream of IKK activation. Receptor and adaptor assembly of one ligand type might rapidly accumulate and sequester all available molecules of a shared adaptor component (such as TRAF6), preventing activation due to a competing ligand type. This emerging result points to the NF-κB switch as not only a way for cells to manipulate response probability and heterogeneity, but also addresses the problem of how cells simultaneously process multiple ligands – by allowing cells to stochastically choose one ligand and effectively ignore other ligands competing for the same pathway.

5.2.2 NF-κB oscillation as a frequency filter

We showed that NF-κB dependent gene expression is enhanced when periodic input causes entrained NF-κB oscillations and diminished when periodic input disrupts NF-κB oscillations. However it isn't yet clear how NF-κB coordinates gene expression across the broader space of input frequencies.

Simulations of periodic TNF pulse inputs show that NF-κB can act as a bandpass filter or a notch filter, depending on the width of the TNF pulse. For 10 min pulse width, gene expression output is maximized when the input frequency is near the NF-κB natural frequency (90 min), with decreased output for input frequencies either above or below – thus NF-κB acts as a bandpass filter. Curiously, simulations show opposite behavior with a shorter pulse width. For 1 min pulses NF-κB functions as a notch filter, with minimized gene expression output when the system is stimulated near the NF-κB natural frequency.

Secretion occurs in pulsatile fashion, and immune cells such as T cells can secrete periodically (Han et al., 2012). This simulation result implies that cells could communicate information based on both the frequency of pulsed secretion and length of individual pulses – and will be fascinating to follow up experimentally.

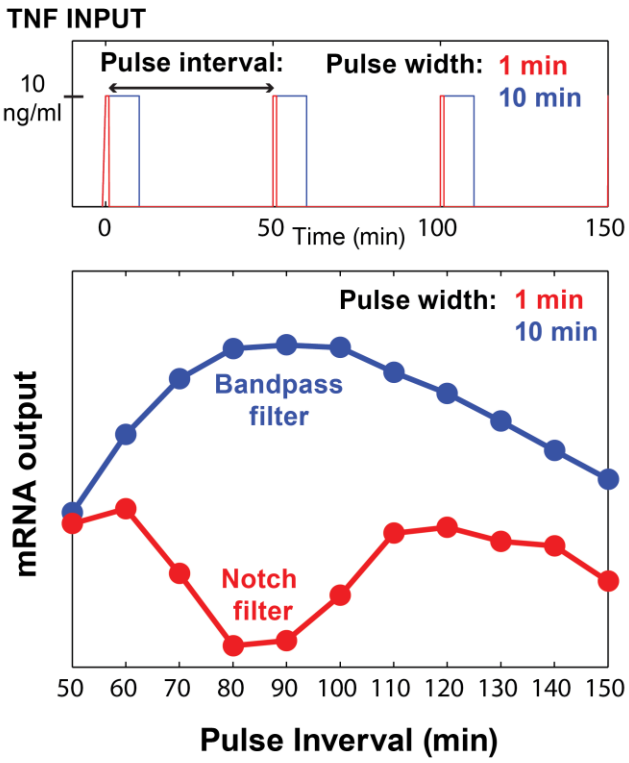

Figure 2. NF-κB as a bandpass or notch filter on gene expression (simulation). For pulses of TNF delivered at different intervals, NF-κB gene output acts like a filter – either bandpass or notch, depending on the pulse width of the input signal. When the input interval is near the NF-κB natural period (90 min), output is maximized (for a 10 min pulse) or minimized (for a 1 min pulse).

5.3 Outlook

This work showed that NF-κB digital activation and noisy oscillation serve specific function in the processing temporally modulated input signals: the digital NF-κB switch controls probability and heterogeneity of response based on the area and shape of the input, and NF-κB oscillation regulates transcriptional efficiency based on the input signal frequency. The logical extension of this work to look beyond cells in isolation and ask how cells communities organize and dynamically coordinate signaling to implement tissue functions. Microfluidics will again play an essential role by enabling 3D culture in designed geometrical and cell type conformations to mimic aspects of tissue organization (Huh et al., 2013). Gene editing technologies such as CRISPR will greatly facilitate the ability to monitor an increasing number of dynamic signaling events inside cells (Yang et al., 2013). Finally, microscopy technologies are rapidly advancing to allow fast, high-resolution imaging deep into living tissues (Pantazis and Supatto, 2014).

Continuing in dynamics of innate immune signaling an emerging area is how the microbiome influences immunity and disease. Microbes reside in all mucosal and air surfaces on the body including skin, mouth and particularly the gut – and outnumbering human cells 10 to 1 (Arumugam et al., 2011). Further, microbiome composition and function has been implicated in dozens of diseases spanning inflammatory bowel disease to brain diseases such as autism (Furusawa et al., 2013). However, the mechanisms of bidirectional interaction between microbiota and host physiology are unknown, making the field ripe for investigation into dynamic signaling at the microbe – immune interface using live imaging and microfluidics.

5.4 References

Adachi, S., and Iwata, M. (2002). Duration of calcineurin and Erk signals regulates CD4/CD8 lineage commitment of thymocytes. Cell. Immunol. *215*, 45–53.

Ahmed, S., Grant, K.G., Edwards, L.E., Rahman, A., Cirit, M., Goshe, M.B., and Haugh, J.M. (2014). Data-driven modeling reconciles kinetics of ERK phosphorylation, localization, and activity states. Mol. Syst. Biol. *10*, 718.

Albeck, J.G., Mills, G.B., and Brugge, J.S. (2013). Frequency-Modulated Pulses of ERK Activity Transmit Quantitative Proliferation Signals. Mol. Cell *49*, 249–261.

Altan-Bonnet, G., and Germain, R.N. (2005). Modeling T cell antigen discrimination based on feedback control of digital ERK responses. PLoS Biol. *3*, 1925–1938.

Aoki, K., Yamada, M., Kunida, K., Yasuda, S., and Matsuda, M. (2011). Processive phosphorylation of ERK MAP kinase in mammalian cells. Proc. Natl. Acad. Sci. U. S. A. *108*, 12675–12680.

Arumugam, M., Raes, J., Pelletier, E., Le Paslier, D., Yamada, T., Mende, D.R., Fernandes, G.R., Tap, J., Bruls, T., Batto, J.-M., et al. (2011). Enterotypes of the human gut microbiome. Nature *473*, 174–180.

Ashall, L., Horton, C. a, Nelson, D.E., Paszek, P., Harper, C. V, Sillitoe, K., Ryan, S., Spiller, D.G., Unitt, J.F., Broomhead, D.S., et al. (2009). Pulsatile stimulation determines timing and specificity of NF-kappaB-dependent transcription. Science *324*, 242–246.

Baeuerle, P. a, and Baltimore, D. (1988). Activation of DNA-binding activity in an apparently cytoplasmic precursor of the NF-kappa B transcription factor. Cell *53*, 211–217.

Bagowski, C.P., and Ferrell, J.E. (2001). Bistability in the JNK cascade. Curr. Biol. *11*, 1176–1182.

Baker, R.G., Hayden, M.S., and Ghosh, S. (2011). NF-κB, inflammation, and metabolic disease. Cell Metab. *13*, 11–22.
Baltimore, D. (2009). Discovering NF- k B. 1–4.
Beer, N.R., Wheeler, E.K., Lee-Houghton, L., Watkins, N., Nasarabadi, S., Hebert, N., Leung, P., Arnold, D.W., Bailey, C.G., and Colston, B.W. (2008). On-chip single-copy real-time reverse-transcription PCR in isolated picoliter droplets. Anal. Chem. *80*, 1854–1858.
Behar, M., and Hoffmann, A. (2013). Tunable signal processing through a kinase control cycle: The IKK signaling node. Biophys. J. *105*, 231–241.
Behar, M., Barken, D., Werner, S.L., and Hoffmann, A. (2013). Theory The Dynamics of Signaling as a Pharmacological Target. Cell *155*, 448–461.
Bhatia, S.N., and Ingber, D.E. (2014). Microfluidic organs-on-chips. Nat. Biotechnol. *32*, 760–772.
Ca, A. (1998). Calcium oscillations increase the efficiency and specificity of gene expression. *392*, 933–936.
Cai, L., Dalal, C.K., and Elowitz, M.B. (2008). Frequency-modulated nuclear localization bursts coordinate gene regulation. Nature *455*, 485–490.
Dolmetsch, R.E., Lewis, R.S., Goodnow, C.C., and Healy, J.I. (1997). Differential activation of transcription factors induced by Ca2+ response amplitude and duration. Nature *386*, 855–858.
Eldar, A., and Elowitz, M.B. (2010). Functional roles for noise in genetic circuits. Nature *467*, 167–173.
Elowitz, M.B., Levine, A.J., Siggia, E.D., and Swain, P.S. (2002). Stochastic gene expression in a single cell. Sci. Signal. *297*, 1183.
Fu, Y., Lim, S., Urano, D., Tunc-ozdemir, M., Phan, N.G., and Elston, T.C. (2014). Theory Reciprocal Encoding of Signal Intensity and Duration in a Glucose-Sensing Circuit. Cell *156*, 1084–1095.
Furusawa, Y., Obata, Y., Fukuda, S., Endo, T. a, Nakato, G., Takahashi, D., Nakanishi, Y., Uetake, C., Kato, K., Kato, T., et al. (2013). Commensal microbe-derived butyrate induces the differentiation of colonic regulatory T cells. Nature *504*, 446–450.
Gerondakis, S., Fulford, T.S., Messina, N.L., and Grumont, R.J. (2014). NF-κB control of T cell development. Nat. Immunol. *15*, 15–25.
Gómez-Sjöberg, R., Leyrat, A. a., Pirone, D.M., Chen, C.S., and Quake, S.R. (2007). Versatile, fully automated, microfluidic cell culture system. Anal. Chem. *79*, 8557–8563.
Gottschalk, R. a., Hathorn, M.M., Beuneu, H., Corse, E., Dustin, M.L., Altan-Bonnet, G., and Allison, J.P. (2012). Distinct influences of peptide-MHC quality and quantity on in vivo T-cell responses. Proc. Natl. Acad. Sci. *109*, 881–886.
Han, Q., Bagheri, N., Bradshaw, E.M., Hafler, D. a., Lauffenburger, D. a., and Love, J.C. (2012). From the Cover: Polyfunctional responses by human T cells result from sequential release of cytokines. Proc. Natl. Acad. Sci. *109*, 1607–1612.
Hao, S., and Baltimore, D. (2013). RNA splicing regulates the temporal order of TNF-induced gene expression. Proc. Natl. Acad. Sci. U. S. A. *110*, 11934–11939.
Hayden, M.S., and Ghosh, S. (2008). Shared Principles in NF-kB Signaling. Cell *132*, 344–362.
Hoffmann, A., and Baltimore, D. (2006). Circuitry of nuclear factor kappaB signaling. Immunol. Rev. *210*, 171–186.
Hoffmann, A., Levchenko, A., Scott, M.L., and Baltimore, D. (2002). The IkappaB-NF-kappaB signaling module: temporal control and selective gene activation. Science *298*, 1241–1245.
Hong, J.W., Studer, V., Hang, G., Anderson, W.F., and Quake, S.R. (2004). A nanoliter-scale nucleic acid processor with parallel architecture. Nat. Biotechnol. *22*, 435–439.
Hornung, G., and Barkai, N. (2008). Noise propagation and signaling sensitivity in biological networks: a role for positive feedback. PLoS Comput. Biol. *4*, e8.
Hughey, J.J., Gutschow, M. V, Bajar, B.T., and Covert, M.W. (2014). Single-cell variation leads to population invariance in NF- κB signaling dynamics.
Huh, D., Kim, H.J., Fraser, J.P., Shea, D.E., Khan, M., Bahinski, A., Hamilton, G. a, and Ingber, D.E. (2013). Microfabrication of human organs-on-chips. Nat. Protoc. *8*, 2135–2157.

Iezzi, G., Karjalainen, K., and Lanzavecchia, A. (1998). The Duration of Antigenic Stimulation Determines the Fate of Naive and Effector T Cells. Immunity *8*, 89–95.
Iliescu, C., Taylor, H., Avram, M., Miao, J., and Franssila, S. (2012). A practical guide for the fabrication of microfluidic devices using glass and silicon. Biomicrofluidics *6*, 16505–1650516.
Imayoshi, I., Isomura, A., Harima, Y., Kawaguchi, K., Kori, H., Miyachi, H., Fujiwara, T., Ishidate, F., and Kageyama, R. (2013). Oscillatory control of factors determining multipotency and fate in mouse neural progenitors. Science *342*, 1203–1208.
Junkin, M., and Tay, S. (2014). Microfluidic single-cell analysis for systems immunology. Lab Chip *14*, 1246–1260.
Kazmierczak, B., and Lipniacki, T. (2010). Spatial gradients in kinase cascade regulation. IET Syst. Biol. *4*, 348–355.
Kellogg, R.A., and Tay, S. (2015). Noise Facilitates Transcriptional Control under Dynamic Inputs. Cell *160*, 381–392.
Kellogg, R.A., Gómez-Sjöberg, R., Leyrat, A.A., and Tay, S. (2014). High-throughput microfluidic single-cell analysis pipeline for studies of signaling dynamics. Nat. Protoc. *9*, 1713–1726.
Kingeter, L.M., Paul, S., Maynard, S.K., Cartwright, N.G., and Schaefer, B.C. (2010). Cutting edge: TCR ligation triggers digital activation of NF-kappaB. J. Immunol. *185*, 4520–4524.
Knutson, C.G., Mangerich, A., Zeng, Y., Raczynski, A.R., Liberman, R.G., Kang, P., Ye, W., Prestwich, E.G., Lu, K., Wishnok, J.S., et al. (2013). Chemical and cytokine features of innate immunity characterize serum and tissue profiles in inflammatory bowel disease. Proc. Natl. Acad. Sci. U. S. A. *110*, E2332–E2341.
Kobayashi, T., Mizuno, H., Imayoshi, I., Furusawa, C., Shirahige, K., and Kageyama, R. (2009). The cyclic gene Hes1 contributes to diverse differentiation responses of embryonic stem cells. 1870–1875.
Von Kriegsheim, A., Baiocchi, D., Birtwistle, M., Sumpton, D., Bienvenut, W., Morrice, N., Yamada, K., Lamond, A., Kalna, G., Orton, R., et al. (2009a). Cell fate decisions are specified by the dynamic ERK interactome. Nat. Cell Biol. *11*, 1458–1464.
Von Kriegsheim, A., Baiocchi, D., Birtwistle, M., Sumpton, D., Bienvenut, W., Morrice, N., Yamada, K., Lamond, A., Kalna, G., Orton, R., et al. (2009b). Cell fate decisions are specified by the dynamic ERK interactome. Nat. Cell Biol. *11*, 1458–1464.
Lee, T.K., Denny, E.M., Sanghvi, J.C., Gaston, J.E., Maynard, N.D., Hughey, J.J., and Covert, M.W. (2009). A noisy paracrine signal determines the cellular NF-kappaB response to lipopolysaccharide. Sci. Signal. *2*, ra65.
Leman, M., Abouakil, F., Griffiths, A.D., and Tabeling, P. (2014). Droplet-based microfluidics at the femtolitre scale. Lab Chip.
Levine, J.H., Lin, Y., and Elowitz, M.B. (2013a). Functional roles of pulsing in genetic circuits. Science *342*, 1193–1200.
Levine, J.H., Lin, Y., and Elowitz, M.B. (2013b). Functional roles of pulsing in genetic circuits. Science *342*, 1193–1200.
Lin, S.-C., Lo, Y.-C., and Wu, H. (2010). Helical assembly in the MyD88-IRAK4-IRAK2 complex in TLR/IL-1R signalling. Nature *465*, 885–890.
Lipniacki, T., Puszynski, K., Paszek, P., Brasier, A.R., and Kimmel, M. (2007). Single TNFalpha trimers mediating NF-kappaB activation: stochastic robustness of NF-kappaB signaling. BMC Bioinformatics *8*, 376.
Liu, B., Bhatt, D., Oltvai, Z.N., Greenberger, J.S., and Bahar, I. (2014). Significance of p53 dynamics in regulating apoptosis in response to ionizing radiation, and polypharmacological strategies. Sci. Rep. *4*, 6245.
Liu, T., Yamaguchi, Y., Shirasaki, Y., Shikada, K., Yamagishi, M., Hoshino, K., Kaisho, T., Takemoto, K., Suzuki, T., Kuranaga, E., et al. (2013). Single-Cell Imaging of Caspase-1 Dynamics Reveals an All-or-None Inflammasome Signaling Response. Cell Rep. *8*, 974–982.
Mali, P., Yang, L., Esvelt, K.M., Aach, J., Guell, M., DiCarlo, J.E., Norville, J.E., and Church, G.M. (2013). RNA-guided human genome engineering via Cas9. Science *339*, 823–826.

Malleshaiah, M.K., Shahrezaei, V., Swain, P.S., and Michnick, S.W. (2010). The scaffold protein Ste5 directly controls a switch-like mating decision in yeast. Nature *465*, 101–105.
Marcus, J.S., Anderson, W.F., and Quake, S.R. (2006). Microfluidic single-cell mRNA isolation and analysis. Anal. Chem. *78*, 3084–3089.
McDonnell, M.D., and Ward, L.M. (2011). The benefits of noise in neural systems: bridging theory and experiment. Nat. Rev. Neurosci. *12*, 415–426.
Meffert, M.K., and Baltimore, D. (2005). Physiological functions for brain NF-kappaB. Trends Neurosci. *28*, 37–43.
Miskov-Zivanov, N., Turner, M.S., Kane, L.P., Morel, P. a, and Faeder, J.R. (2013). The duration of T cell stimulation is a critical determinant of cell fate and plasticity. Sci. Signal. *6*, ra97.
Negro, A., Dodge-Kafka, K., and Kapiloff, M.S. (2008). Signalosomes as therapeutic targets. Prog. Pediatr. Cardiol. *25*, 51–56.
Nelson, D.E., Ihekwaba, A.E.C., Elliott, M., Johnson, J.R., Gibney, C.A., Foreman, B.E., Nelson, G., See, V., Horton, C.A., Spiller, D.G., et al. (2004). Oscillations in NF-kappaB signaling control the dynamics of gene expression. Science *306*, 704–708.
Oh, H., and Ghosh, S. (2013). NF- j B: roles and regulation in different CD4 + T-cell subsets. 41–51.
Pantazis, P., and Supatto, W. (2014). Advances in whole-embryo imaging: a quantitative transition is underway. Nat. Rev. Mol. Cell Biol. *15*, 327–339.
Paszek, P., Ryan, S., Ashall, L., Sillitoe, K., Harper, C. V, Spiller, D.G., Rand, D. a, and White, M.R.H. (2010). Population robustness arising from cellular heterogeneity. Proc. Natl. Acad. Sci. U. S. A. *107*, 11644–11649.
Pękalski, J., Zuk, P.J., Kochańczyk, M., Junkin, M., Kellogg, R., Tay, S., and Lipniacki, T. (2013). Spontaneous NF-κB activation by autocrine TNFα signaling: A computational analysis. PLoS One *8*.
Petty, M.C., Introduc-, L.F.A., Aca-, F.L.S., Clays, K., Armstrong, N.J., Jr, J.E.F., and Machleder, E.M. (1998). The Biochemical Basis of an All-or-None Cell Fate Switch in Xenopus Oocytes. *280*, 895–899.
Purvis, J.E., and Lahav, G. (2013). Encoding and decoding cellular information through signaling dynamics. Cell *152*, 945–956.
Purvis, J.E., Karhohs, K.W., Mock, C., Batchelor, E., Loewer, A., and Lahav, G. (2012). P53 Dynamics Control Cell Fate. Science *336*, 1440–1444.
Sanchez-Freire, V., Ebert, A.D., Kalisky, T., Quake, S.R., and Wu, J.C. (2012). Microfluidic single-cell real-time PCR for comparative analysis of gene expression patterns. Nat. Protoc. *7*, 829–838.
Santos, S.D.M., Verveer, P.J., and Bastiaens, P.I.H. (2007). Growth factor-induced MAPK network topology shapes Erk response determining PC-12 cell fate. Nat. Cell Biol. *9*, 324–330.
Scha, R., Okuno, T., Hassdorf, R., Shigeto, K., Ono, T., Bode, M., Pietzsch, O., Wiesendanger, R., Getzlaff, M., Wiesendanger, R., et al. (2002). Microfluidic Large-Scale Integration. *4437*.
Selimkhanov, J., Taylor, B., Yao, J., Pilko, A., Albeck, J., Hoffmann, A., Tsimring, L., and Wollman, R. (2014). Systems biology. Accurate information transmission through dynamic biochemical signaling networks. Science *346*, 1370–1373.
Sen, R., and Baltimore, D. (1986). Multiple nuclear factors interact with the immunoglobulin enhancer sequences. Cell *46*, 705–716.
Shah, N. a, and Sarkar, C. a (2011). Robust network topologies for generating switch-like cellular responses. PLoS Comput. Biol. *7*, e1002085.
Shinohara, H., Behar, M., Inoue, K., Hiroshima, M., Yasuda, T., Nagashima, T., Kimura, S., Sanjo, H., Maeda, S., Yumoto, N., et al. (2014). Positive feedback within a kinase signaling complex functions as a switch mechanism for NF-κB activation. Science *344*, 760–764.
Sinha, M.K., Sturis, J., Ohannesian, J., Magosin, S., Caro, F., Stephens, T., Heiman, M.L., and Polonsky, K.S. (1996). Ultradian Oscillations of Leptin Secretion in Humans between midnight and early morning hours and lowest around noon to mid-afternoon . In the. Biochem. Biophys. Res. Commun. *738*, 733–738.
Spiller, D.G., Wood, C.D., Rand, D. a, and White, M.R.H. (2010). Measurement of single-cell dynamics. Nature *465*, 736–745.

Tay, S., Hughey, J.J., Lee, T.K., Lipniacki, T., Quake, S.R., and Covert, M.W. (2010). Single-cell NF-kappaB dynamics reveal digital activation and analogue information processing. Nature *466*, 267–271.
Walker, J.J., Terry, J.R., and Lightman, S.L. (2010). Origin of ultradian pulsatility in the hypothalamic-pituitary-adrenal axis. Proc. Biol. Sci. *277*, 1627–1633.
Warmflash, A., Zhang, Q., Sorre, B., Vonica, A., Siggia, E.D., and Brivanlou, A.H. (2012). Dynamics of TGF-β signaling reveal adaptive and pulsatile behaviors reflected in the nuclear localization of transcription factor Smad4. Proc. Natl. Acad. Sci. U. S. A. *109*, E1947–E1956.
Warren, L., Bryder, D., Weissman, I.L., and Quake, S.R. (2006). Transcription factor profiling in individual hematopoietic progenitors by digital RT-PCR. Proc. Natl. Acad. Sci. U. S. A. *103*, 17807–17812.
Wee, K.B., Yio, W.K., Surana, U., and Chiam, K.H. (2012a). Transcription factor oscillations induce differential gene expressions. Biophys. J. *102*, 2413–2423.
Wee, K.B., Yio, W.K., Surana, U., and Chiam, K.H. (2012b). Transcription factor oscillations induce differential gene expressions. Biophys. J. *102*, 2413–2423.
Werner, S.L., Barken, D., and Hoffmann, A. (2005). Stimulus specificity of gene expression programs determined by temporal control of IKK activity. Science *309*, 1857–1861.
Whitesides, G.M. (2006). The origins and the future of microfluidics. Nature *442*, 368–373.
Wu, H. (2013). Essay Higher-Order Assemblies in a New Paradigm of Signal Transduction. 287–292.
Yang, H., Wang, H., Shivalila, C.S., Cheng, A.W., Shi, L., and Jaenisch, R. (2013). Resource One-Step Generation of Mice Carrying Reporter and Conditional Alleles by CRISPR / Cas-Mediated Genome Engineering. Cell *154*, 1370–1379.
Yin, Q., Lin, S.-C., Lamothe, B., Lu, M., Lo, Y.-C., Hura, G., Zheng, L., Rich, R.L., Campos, A.D., Myszka, D.G., et al. (2009). E2 interaction and dimerization in the crystal structure of TRAF6. Nat. Struct. Mol. Biol. *16*, 658–666.
Yissachar, N., Fischler, T.S., Cohen, A.A., Reich-zeliger, S., Russ, D., Shifrut, E., and Porat, Z. (2013). Short Article Dynamic Response Diversity of NFAT Isoforms in Individual Living Cells. Mol. Cell *49*, 322–330.
Zambrano, S., Bianchi, M.E., and Agresti, A. (2014). High-throughput analysis of NF-κB dynamics in single cells reveals basal nuclear localization of NF-κB and spontaneous activation of oscillations. PLoS One *9*, e90104.
Zanoni, I., Ostuni, R., Marek, L.R., Barresi, S., Barbalat, R., Barton, G.M., Granucci, F., and Kagan, J.C. (2011). CD14 Controls the LPS-Induced Endocytosis of Toll-like Receptor 4. Cell *147*, 868–880.